2012

Structural and Functional Studies of SLO K+ Channels: Mechanisms of Gating by Intracellular Signaling

Manuel D. Leonetti

STRUCTURAL AND FUNCTIONAL STUDIES OF SLO K^+ CHANNELS:

MECHANISMS OF GATING BY INTRACELLULAR SIGNALING

A Thesis Presented to the Faculty of

The Rockefeller University

in Partial Fulfillment of the Requirements for

the degree of Doctor of Philosophy

by

Manuel D. Leonetti

June 2012

STRUCTURAL AND FUNCTIONAL STUDIES OF SLO K^+ CHANNELS:

MECHANISMS OF GATING BY INTRACELLULAR SIGNALING

Manuel D. Leonetti, Ph.D.
The Rockefeller University 2012

Eukaryotic K^+ channels from the SLO family (SLO1, SLO2 and SLO3) provide a link between intracellular signaling and the electrical activity of a cell. The opening and closing (gating) of the three different SLO homologs is controlled by the synergistic action of membrane voltage and specific intracellular cues: Ca^{2+} binding in SLO1, Na^+ binding in SLO2 and pH increase in SLO3. It is known that intracellular signals activate SLO channels by acting on the large cytoplasmic domains (CTDs) of these proteins, which follows the transmembrane ion-conduction pore. However, a molecular description of the mechanisms of intracellular gating in SLO channels is still lacking.

In this thesis, I present biochemical, structural and functional studies aiming at understanding how the activity of SLO1 and SLO3 channels is controlled by intracellular Ca^{2+} binding and pH increase, respectively. First, I describe recombinant methods for the large-scale expression and purification of functional SLO channels, paving the way for a more complete biochemical and structural analysis of these proteins. Then, I report the crystal structures of the large cytoplasmic domains (CTDs) from two different SLO1 channels. Structures of the Ca^{2+}-bound CTDs from human and zebrafish SLO1 channels define the precise molecular architecture of SLO1's Ca^{2+}-sensing module: CTDs from the four subunits of a tetrameric SLO1 channel assemble in a so-called gating ring

structure at the intracellular face of the membrane. In conjunction with other studies, these results describe how Ca^{2+} binding affects the conformation of one layer of the SLO1 gating ring, which can explain the Ca^{2+}-driven opening of SLO1's ion conduction pore. Next, I present the crystal structure of the human SLO3 gating ring. A comparison with the SLO1 structures suggests that the hSLO3 structure represents the open conformation of the hSLO3 gating ring. Finally, I describe functional mutagenesis studies on the mouse SLO3 ortholog, which reveal a possible mechanism for pH sensing in the mouse SLO3 channel. Surprisingly, the mechanism I propose appears not to be conserved in SLO3 channels from other species. This could be a dramatic example of how new functional mechanisms can easily evolve within the very versatile scaffold of a gating ring structure.

Altogether, the results presented in this thesis provide a molecular framework to understand the mechanisms of intracellular gating in SLO channels.

À mes parents, Josette et Charles, pour m'avoir accompagné dans toutes mes aventures, des deux côtés de l'Atlantique.

ACKNOWLEDGEMENTS

Being a graduate student in the MacKinnon laboratory has been, at so many levels, a fantastic adventure. My first thanks go to my advisor Rod. Rod, your communicative passion for science, and the rigor and clarity of your thinking have inspired me tremendously. Working with you made me a better scientist. Thank you.

One aspect of Rod's genius is his ability to bring together an amazing group of scientists. I am truly grateful to all members of the MacKinnon lab for their help and friendship. I learned so much by working close to all of you. First and foremost, I am particularly indebted to my colleague and mentor Peng Yuan for his extraordinary support over the years. We made a great team. I also want to sincerely thank Liang Feng for his help and generosity. Thanks also to Yichun Hsiung for her continuous help, and to Jose Avalos for guiding my first steps in the lab. I also want to thank our collaborators Maria Garcia and Bill Schmalhofer for their assistance and advice.

Thanks to Seth Darst, Brian Chait, Chris Miller and Jacques Neyton for their time and advice as members of my thesis committee. And thanks to the Dean's Office for their commitment to the students.

The love and support of my family and friends have had a huge influence on my ability to do the best possible science during my Ph.D. In particular, I am truly thankful to my parents for their everlasting support.

TABLE OF CONTENTS

LIST OF FIGURES

LIST OF TABLES

CHAPTER ONE:

INTRODUCTION

Living cells are sophisticated information-processing machines. In order to perform the essential functions of survival of the organism or transmission of genetic material, a cell must perceive and process information about both its environment and its own physiological state. Within the cell, a wide range of signals acting in concert allow this information to be integrated and transmitted, to ultimately coordinate the action of the various cellular components that will elicit an appropriate response. One of the most ubiquitous forms of cellular signaling is electrical in nature: by controlling the distribution and movement of ions (that is, electric charges), a cell can encode signals in the form of a voltage across the lipid membrane surrounding it. This voltage can in turn be sensed by specialized proteins in the cell to regulate their activity.

At a very general level, the work presented here aims at understanding some specific aspects of how electrical signaling is used and controlled in cells. I studied a family of eukaryotic proteins called the SLO potassium channels, which regulate the electrical activity of a cell in response to an intracellular stimulus. In a sense, SLO channels translate information about intracellular activity into electrical signaling. The main question I am interested to address is how this translation occurs at the molecular level, in other words by which mechanisms intracellular activity modulates these proteins in order to control their function.

To appreciate the biological role of SLO channels, I will start by introducing the basic principles of electrical signaling in cells. I will then present in detail the SLO family of K^+ channels, insisting on their physiological roles and functional properties. I will finish this introduction by describing my research project and the motivation for my work.

1.1 - ELECTRICAL SIGNALING IN CELLS AND ION CHANNELS

1.1.1) "Animal electricity"

Electricity is an essential part of life's toolbox. For example, the electrical signals that we can visualize in an electrocardiogram control our heartbeats. Which form, then, does electricity take in a living cell?

Any electrical phenomenon is intrinsically linked to the movement of electric charges. In biology, these charges are the inorganic ions (mostly: Na^+, K^+, Ca^{2+} and Cl^-) present in the aqueous environment that makes up the interior and the surroundings of living cells (1, 2). As first envisioned by Julius Bernstein in the very beginning of the 20th century (3), it is the controlled movement of these ions in and out of cells that generates electrical signals (1, 2). In addition to inorganic ions, life's electrical system is based on three essential components: the hydrophobic cell membrane, and two classes of proteins called ion pumps (also called ion transporters) and ion channels (Figure 1). The cell membrane is a thin oil-like lipid bilayer that separates the cell's interior from its environment. The hydrophobic character of the membrane forbids the free crossing of most components of cells and their external milieu, in particular ions. The movement of ions across the membrane is carried out by proteins embedded in and spanning through the lipid bilayer: ion pumps and ion channels (1, 4). Ion pumps use energy to force the transport of ions in one specific direction, and thus generate concentration gradients across the membrane. Ion channels, which are the focus of my work, do not use energy and are therefore passive pores in the membrane that can only let ions diffuse along their (electro)chemical gradient (5).

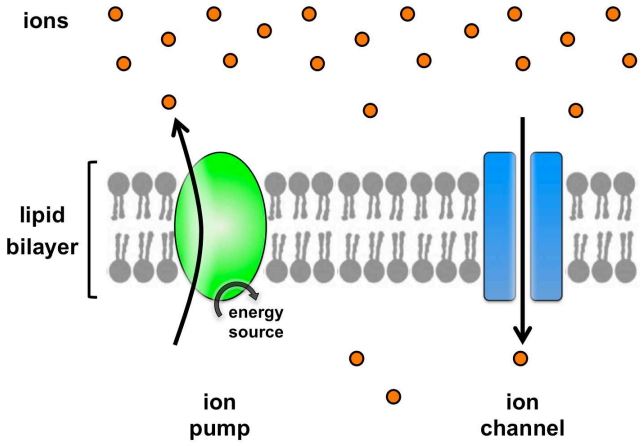

Figure 1: The molecular components of life's electrical system. Two kinds of proteins embedded in the cell membrane control the movement of ions. Pumps use energy to create ionic concentration gradients, while channels are passive pores letting ions flow down their electrochemical gradients.

1.1.2) Ion channels are at the core of the cell's electrical network

Electrical signals in cells are encoded in the form of a voltage (difference of electric potential) across the membrane. To act as a signal, the transmembrane voltage must satisfy two essential criteria: it should be 1) precisely controllable and 2) able to influence downstream effectors. The dynamic control of the cell's voltage arises from two central properties of ion channels: selectivity and gating.

Most channels are selective: they only allow a specific type of ion to cross through their pore, excluding others. When an ion channel opens, the membrane voltage at equilibrium is set at the reversal potential, i.e. the point at which diffusion and electric driving forces commanding ion flow exactly balance each other. For a selective ion channel, Nernst's law of electrodiffusion shows that this reversal potential is determined solely by the ratio of ion concentration outside vs. inside the cell (Figure 2a). The action of dedicated pumps ensures that these concentration ratios are different for Na^+, K^+, Ca^{2+} or Cl^- ions. Selective channels for each of these ions exist, such that the opening of a Na-, K-, Ca- or Cl-selective channel sets the membrane voltage at different values (Figure 2b) (1, 2). Non-selective cation channels, which do not discriminate between cations but prevent the conduction of anions and reverse at 0 mV, form another important class of channels. At rest, the cell is polarized: the voltage is more negative inside (typically -70 mV in animal cells) due to the opening of K^+ and Cl^- channels (2, 6-8). During activation or signal transmission, the membrane voltage becomes less negative (depolarization) owing to the action of Na^+, Ca^{2+} or non-selective cation channels (1, 2, 9). When multiple channels are opened at once, each specific channel type drives the membrane voltage towards its own reversal potential, and the overall potential depends on the number and strength of each individual conductance. Hence, by controlling the opening of particular kinds of selective ion channels, cells can modulate the value of the transmembrane voltage and

2a $$\textit{Nernst equation for ion X:} \quad E_{rev} = \frac{RT}{zF} \ln \frac{[X]_{out}}{[X]_{in}}$$

2b

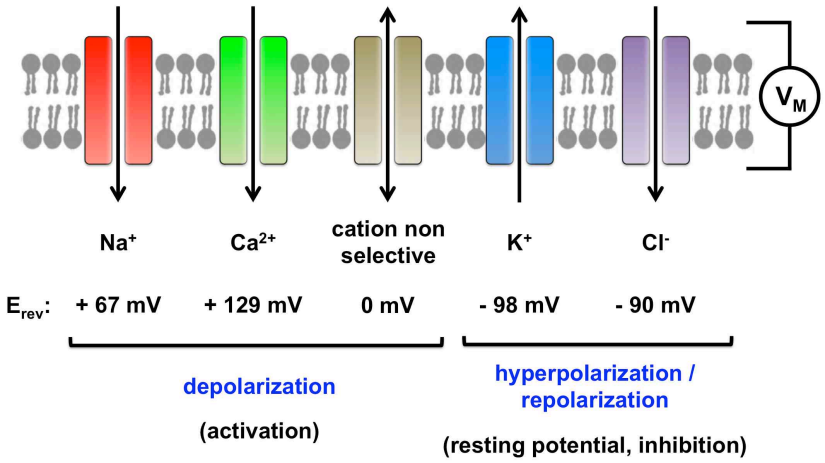

2c

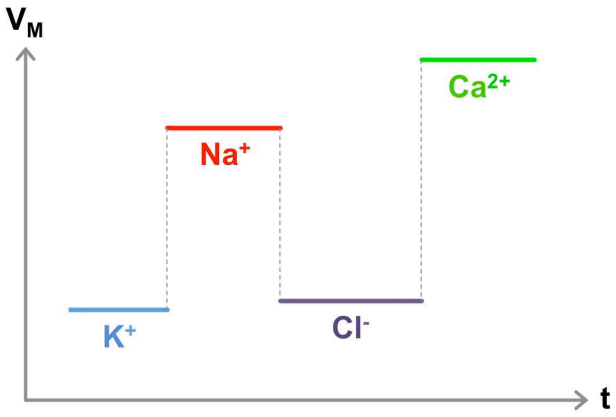

Figure 2: The different reversal potentials of selective ion channels allow information to be encoded in the membrane voltage. 2a) The ratio of ionic concentration across the membrane sets the reversal potential (E_{rev}) of a selective ion channel according to the Nernst equation (R: gas constant; T: temperature; *z*: ionic charge; F: Faraday constant). **2b)** This ratio varies for the different ionic species in a cell (Na^+, Ca^{2+}, K^+, Cl^-), so that the reversal potential of the corresponding selective ion channels are different (values are given for a typical mammalian skeletal muscle cell). **2c)** Opening of specific selective channels controls the membrane voltage, allowing information to be encoded (showing the example of sequential openings of K^+-, Na^+-, Cl^-- and Ca^{2+}- selective channels).

encode information (Figure 2c). This is another essential functional feature of ion channels, known as gating: channels respond to specific signals that govern their opening and closing. Multiple modes of gating exist, ranging from binding of a ligand to the action of light (1).

In essence, ion channel gating mediates the tuning of the membrane voltage to encode information. Downstream, the transmission of these signals is ensured by specialized membrane proteins that can sense the voltage and modulate their activity in response to it. These proteins are said to be voltage-dependent, and in fact the most ubiquitous voltage-dependent proteins are ion channels themselves (1, 10). The interplay between membrane voltage and opening of voltage-gated channels is the basis for the conduction of action potentials, first described in the seminal work of Hodgkin and Huxley (11). However, voltage sensing is not restricted to channels, as demonstrated by the recent discovery of Ci-VSP, a phosphatase enzyme whose activity is governed by membrane voltage (12).

1.1.3) Electrical signaling is ubiquitous

Historically, the study of electrical signaling focused on tissues like nerves and muscles where electrical phenomena manifest themselves perhaps the most obviously. Neurons or muscle fibers belong to the family of excitable cells, in which activity is controlled by the propagation of action potentials (1). The outcome of action potential propagation is the opening of voltage-gated Ca^{2+} channels, and the subsequent entry of Ca^{2+} is the trigger for the main functional response of excitable cells: release of synaptic vesicles in neurons, or actin/myosin sliding in muscular fibers, for example.

Nonetheless, the basic components of the cellular electrical system are present in virtually every cell type and every organism. In particular, voltage-

gated proteins are ubiquitous (1, 6, 13). Since the core function of these proteins is to sense variations in the membrane voltage, their ubiquity mirrors the universality of electrical signaling in nature. For example, as I will discuss later, one of the proteins I studied extensively is specific to sperm cells. Moreover, electrical signaling is not restricted to animal cells and is used by plants as well as unicellular organisms, often to allow a rapid response to environmental changes (1). Examples include the folding of *Mimosa* leaves upon touch (14, 15) or the obstacle avoidance response in *Paramecium* (16). Recently, the discovery of rhythmic variations in the membrane voltage of the bacterium *Escherichia coli* suggests that electrical signaling might be a very ancient form of functional regulation in cells (17).

Altogether, electrical signaling – that is, encoding of information in the form of a voltage across the cell membrane – is central to many aspects of cellular physiology. Since the opening and closing of specific ion channels controls the membrane voltage, understanding how ion channels gate is a key step towards understanding the cellular responses governed by electrical signaling, from information processing in the brain to the ability of a sperm cell to fertilize an egg. Understanding how ion channels gate is precisely my interest. My main focus is the study of a family of eukaryotic K^+ channels called SLO, which regulate many cellular functions, which I will describe in the next section.

1.2 – THE SLO FAMILY OF K^+ CHANNELS: PHYSIOLOGY

1.2.1) Overview of the SLO family of K^+ channels

SLO channels are K^+-selective pores expressed in animal cells, and are gated by both membrane voltage and intracellular signaling. Since K^+ ions are more concentrated inside the cell than outside, opening of a SLO channel hyperpolarizes the membrane and moderates the overall electrical activity of a cell. Three types of SLO channels exist (SLO1, SLO2 and SLO3), which vary by the kind of intracellular cue responsible for their activation (Figure 3a). SLO1, SLO2 and SLO3 are activated by the binding of intracellular Ca^{2+}, intracellular Na^+ or an increase in intracellular pH, respectively (18). Figure 3b shows the basis of SLO1 activation by membrane voltage and intracellular Ca^{2+}: voltage and Ca^{2+} act in synergy to open the SLO1 pore. The same basic principle applies to the activation of SLO2 and SLO3 by voltage and Na^+ or alkalization, respectively.

The activation of SLO1, SLO2 and SLO3 by different intracellular signals underlies the fundamentally different functional roles these proteins play in cells. These differences are reflected in the modest conservation of amino acid sequence between the three homologs (Figure 3a). Especially, SLO2 is quite divergent from SLO1 and SLO3, which are much closely related in sequence and number of transmembrane helices (see below). Nonetheless, the three members of the SLO family share common core properties.

First of all, all SLO channels share the same basic architecture (Figure 4). As most K^+ channels, SLO channels are homo-tetramers in the membrane (19, 20). The transmembrane pore of one protomer contains six transmembrane helices (S1-S6), similar to canonical voltage-gated K^+ channels: S1 to S4 make up

3a

	SLO1	SLO2	SLO3
gated by:	Ca^{2+}	Na^{+}	pH_i ↑

% identity, human sequences

	SLO2.1	SLO2.2	SLO3
SLO1	14%	16%	42%
SLO2.1		75%	14%
SLO2.2			14%

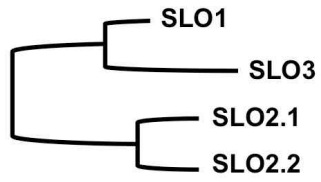

3b

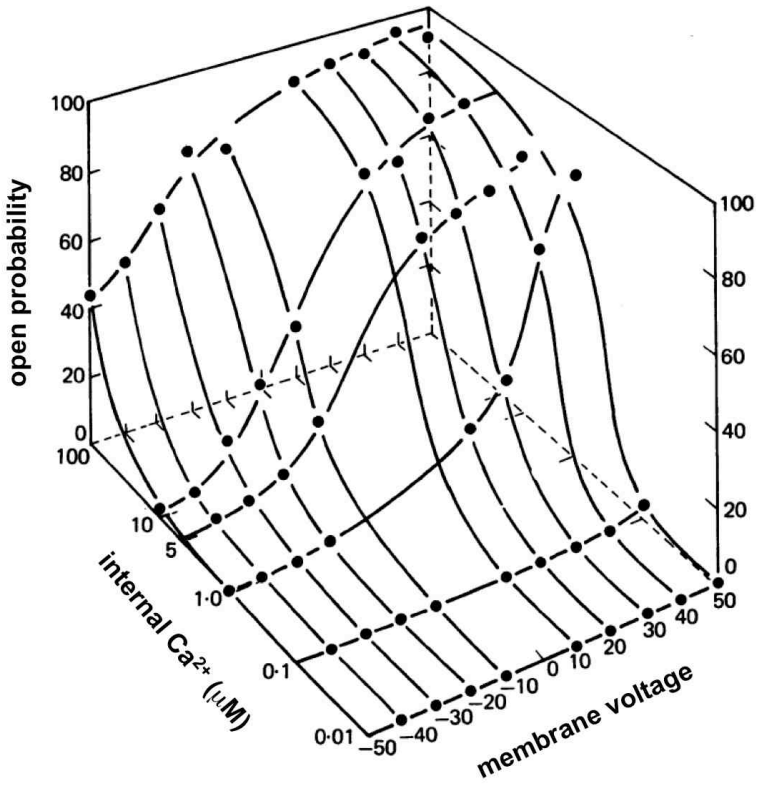

Figure 3: SLO channels: activation and phylogeny. 3a) SLO1, SLO2 and SLO3 are activated by different intracellular signals. The phylogenic relationship shown at the bottom right can be inferred by comparing the sequences of the three homologs. **3b)** Activation of SLO1 by voltage and Ca^{2+}: the channel's open probability is shown as function of intracellular Ca^{2+} concentration and membrane voltage (adapted from *224*).

the unit responsible for voltage sensing (at least in SLO1 and SLO3), whereas S5 and S6 form the pore responsible for ion flow (21). SLO1 and SLO3 (but not SLO2) possess an additional transmembrane N-terminal helix, S0 (22). Following S6, all three channel types have a large cytosolic domain that controls intracellular activation (18, 23). This CyTosolic Domain, or CTD, is made of a tandem of so-called RCK domains: RCK1 and RCK2 (24).

Another similarity arises from the main functional role of SLO channels in cells: SLO channels act as negative feedback switches to regulate the intracellular concentration of the same ions that activates them. This is best described for the Ca^{2+}-activated SLO1 (25, 26). Functional and biochemical studies have established that SLO1 co-localizes with voltage-dependent Ca^{2+} channels in most cell types (25-29). When the cytosolic Ca^{2+} concentration rises, SLO1 opens and the resulting hyperpolarization drives the closing of voltage-gated Ca^{2+} channels in the plasma membrane, thereby shutting off one of the main source of Ca^{2+} entry into the cytoplasm (Figure 5). Overall, the Ca^{2+}-driven opening of SLO1 results in a decrease of intracellular Ca^{2+} itself. The precise mode of action of SLO2 and SLO3 is less well characterized, but it is very likely that the same negative feedback interplay exists between SLO2 and voltage-gated Na^{+} channels or SLO3 and voltage-gated proton channels, both pairs being known to be expressed in the same cell types (30-32).

1.2.2) SLO1 (BK, Maxi-K) channels

SLO1 channels (also known as BK or Maxi-K) were the first of the SLO family to be discovered and characterized. Following the finding that internal Ca^{2+} could activate potassium flux in tissues (33), the development of patch-clamp and reconstitution techniques lead to the identification of a specific kind of Ca^{2+}-activated K^{+} channel with an unusually large unitary conductance (~100-300

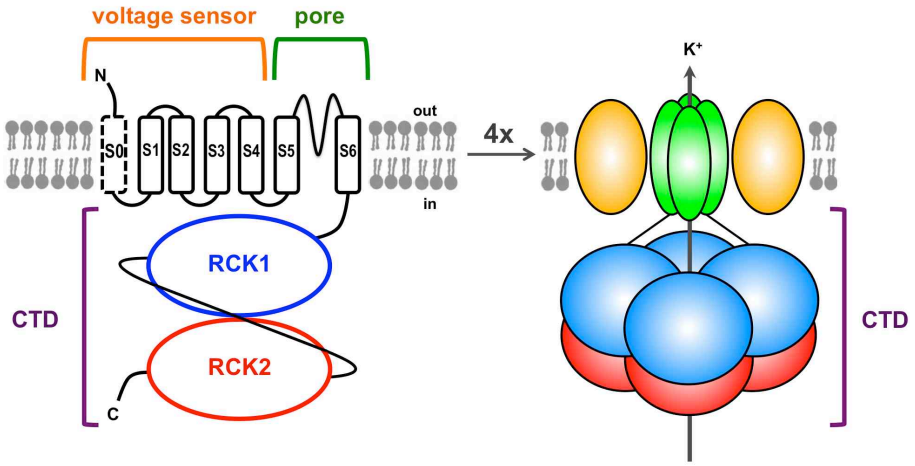

Figure 4: Conserved architecture of SLO channels. The topology of a SLO subunit is shown on the left (the S0 transmembrane helix is not present in SLO2). The voltage sensor, pore, RCK1 and RCK2 domains are shown in orange, green, blue and red respectively. In the membrane, four identical subunits assemble in a tetrameric channel (right, same color-code as previously). The voltage sensors from the front and back subunits are not drawn for clarity.

Figure 5: SLO / voltage-gated channel negative feedback interplay. 3a) SLO1 opening inhibits voltage-gated Ca^{2+} channels by hyperpolarizing the membrane, thereby shutting off one of the main sources of Ca^{2+} entry in the cytoplasm. **3b)** The same interplay is likely to exist between SLO2 and voltage-gated Na^{+} channels, or SLO3 and voltage-gated H^{+} channels.

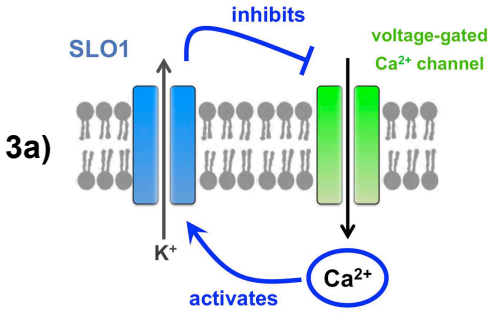

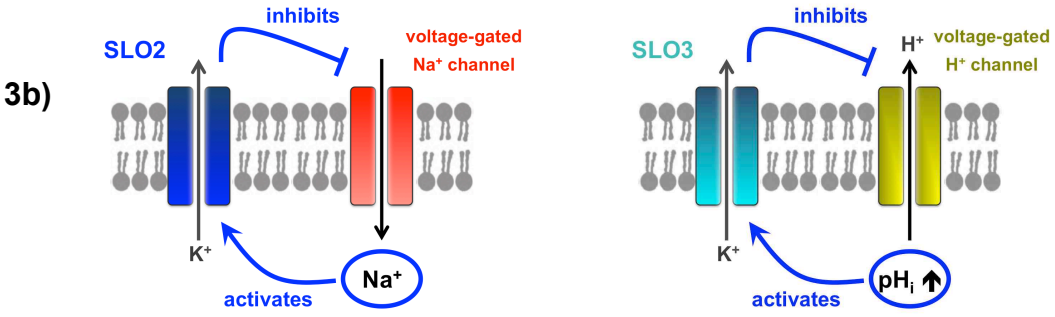

pS in symmetrical 150 mM K^+, to be compared to ~25 pS for the archetypical Shaker delay-rectifier K^+ channel) (34, 35). This property gave the protein its name: BK (for Big-K) or Maxi-K (36, 37). A mutation at the *slowpoke* locus was discovered in *Drosophila* that abolishes BK currents in the fly muscles (38), paving the way for the molecular cloning of the corresponding gene, *slo* (39-41). After the discovery of the related SLO2 and SLO3 channels, BK was renamed SLO1, which is the nomenclature I will be using here (18).

SLO1 channels are expressed throughout the animal kingdom (Metazoa). SLO1 has a remarkably wide range of expression in human tissues, including neurons, smooth and skeletal muscles, endocrine cells, kidney, pancreas or even cartilage. Looking specifically in the brain, immunocytochemistry studies in mice detected SLO1 expression in almost all brain regions (42). The ubiquity of SLO1 in different cell types likely reflects the universal physiological importance of Ca^{2+} signaling (43-45). In excitable cells, where its function is best characterized, SLO1 is involved in controlling neuronal activity, neurotransmitter release, smooth and skeletal muscle tone or hair cell tuning, all of which involve Ca^{2+} entry through voltage-gated Ca^{2+} channels (18, 27, 46-52). The role of SLO1 in non-excitable cells is less well established, but recent studies have proposed that SLO1 currents, by hyperpolarizing the cell, regulate the driving force for Ca^{2+} influx through the plasma membrane or from intracellular stores (53, 54). The wide physiological importance of SLO1 is reflected in the range of phenotypes of SLO1 knock-out (KO) mice: KO animals are viable but exhibit ataxia, impaired vasodilatation and vascular hypertension, incontinence, high-frequency hearing loss and erectile dysfunction (55-59).

The diversity of cellular functions involving SLO1 is also mirrored by a large array of physiological processes that regulate the channel's properties. The functional characteristics of SLO1 currents are modulated extensively by

alternative splicing, complex phosphorylation, lipidation and binding of cofactors (18, 60-64). Another level of complexity arises from the interaction of SLO1 with other proteins in the cell. In particular in tetrapods (including mammals), SLO1 is associated with a class of proteins known as β-subunits which significantly alter its function (26). The first β-subunit, β1, was originally identified in smooth muscles where it co-purifies with SLO1 (65, 66). The elucidation of β1's primary sequence revealed that it contains two transmembrane helices linked by a large, glycosylated extracellular loop (67), and allowed the cloning of three other kinds of β-subunits based on sequence similarity (β2, β3, β4) (68-73). β-subunits affect SLO1 function in different ways: β1, β2 and β4 modulate both voltage-gating, apparent Ca^{2+} sensitivity and activation/deactivation kinetics (73-76), and β2 and β3 confer fast inactivation through a ball-and-chain mechanism (68, 69, 77). The phenotypes of KO mice for β1 and β4 emphasize the functional importance of β-subunits, showing impaired vasoregulation, bladder contraction and airway dilation for β1 (78-81), and increased hippocampal activity for β4 (82). β-subunits are not the only proteins known to interact with SLO1 (18, 60). In particular LRRC26, a leucine-rich repeat-containing (LRRC) protein, has been recently described to dramatically activate SLO1 currents in prostate cancer cells (83). The discovery that a related LRRC protein also activates SLO3 raises the interesting possibility that members of this protein family are general interacting partners of SLO channels (83).

Taken together, the vast diversity of modifications and interactions that regulate SLO1 explains how the functional characteristics of SLO1 currents are fine-tuned in different cell types (18). A fascinating example of how subtle variations of SLO1 properties are important for cellular function is found in the cochlea, where the expression of different SLO1 splice variants and the gradual

expression of β1-subunits define the precise electrical resonant frequency at which individual hair cells are set to respond (50).

1.2.3) SLO2 (Slick, Slack) channels

Expression of Na^+-activated K^+ channels (K_{Na}) is well established in the animal nervous system, from arthropods to mammals (30, 84). Their presence has also been suggested in mammalian muscles, but might be species-specific (see for example (85)). In neurons, K_{Na} function is intimately linked to the excitatory entry of Na^+ during synaptic transmission or action potential propagation, and K_{Na} currents have been shown to regulate the shape of the action potential, the firing rate of neurons or the kinetics of excitatory synaptic response (30, 31, 84, 86-88).

The vast majority of K_{Na} channels are believed to be encoded by *Slo2* (30). SLO2.2 (also known as Slack) was first cloned based on sequence similarity with SLO1 (89), and was later shown to be activated by intracellular Na^+ (90). The SLO2.1 (Slick) paralog was subsequently discovered based on sequence homology (91). Both SLO2.1 and SLO2.2 are Na^+-activated, but vary in their functional details: SLO2.1 opens rapidly, is also activated by intracellular Cl^- and inhibited by ATP binding, whereas SLO2.2 displays slow "on" kinetics, is weakly Cl^--dependent and insensitive to ATP (30, 91). Immunocytochemistry and *in situ* hybridization experiments in rat showed that SLO2.1 and 2.2 are widely expressed in the brain, in particular in the olfactory bulb, visual and somatosensory cortex, midbrain, hippocampus and brainstem (89, 92, 93). The distribution of SLO2 matches the known abundance of K_{Na} currents in the nervous system, reinforcing the idea that most native K_{Na} are encoded by SLO2 (30). However, the lack of specific pharmacological agents for SLO2 has hindered the precise functional characterization of SLO2 channels in tissues.

1.2.4) SLO3 (KSper) channels

The third member of the SLO family is present only in mammals, and is specific to sperm cells (94). SLO3 is activated by membrane voltage and intracellular alkalinization (94, 95). The pH-dependence of SLO3 reflects the fact that intracellular pH (pH_i) is a master regulator of activity in mammalian sperm. pH_i increase activates two essential properties of sperm cells: their motility (i.e., the ability to reach the egg) and their capacity of fertilization (i.e., the ability to break through the egg's membrane and deliver DNA) (32). From the testis to the ovaries, sperm cells experience a gradual increase in extracellular pH, which translates into an increase in pH_i owing to the action of proton pumps and proton channels in the mammalian sperm membrane (32, 96).

Voltage-sensitive ion channels in sperm cells are involved in both regulating and sensing variations of pH_i. In human sperm cells (but not in mice), the voltage-gated proton channel Hv1 is a key regulator of pH_i (32, 97, 98). Furthermore, one of the direct effect of pH_i increase is the opening of pH-dependent voltage-activated Ca^{2+} channels (CatSper, described in mouse and human sperm), which controls many aspects sperm activation (98-100). Hence, pH_i and electrical signals are intimately linked in the physiology of sperm cells.

To date, SLO3 function has been almost exclusively studied in mice, although its expression in human sperm has been shown at the RNA level (94). Electrical recordings of mouse sperm cells using the patch-clamp technique revealed the existence of an alkaline-activated K^+ current (KSper) (101), which was later shown to be carried by SLO3 channels (102-104). Genetic knock-out studies in mice highlighted the physiological importance of SLO3 in male fertility. SLO3 KO mice are completely infertile under natural conditions, and KO sperm cells show morphological defects, impaired motility and compromised ability to undergo the acrosome reaction (103, 104). Importantly,

fertilization with KO sperm cells could be achieved *in vitro*, but with much lower rate of success than with wild-type cells (103, 104). Another interesting aspect of the KO phenotype relates to the response of sperm cells to osmolarity changes. Upon ejaculation, mammalian sperm cells must adapt to a decrease in extracellular osmolarity, and one study showed that the motility and morphological defects of SLO3 KO cells are exacerbated at low osmotic conditions, raising the possibility that SLO3, on top of its role in controlling the electrical balance of sperm cells, might also act as an osmoregulator (104).

Finally, as in the case of SLO1, SLO3 function is likely to be regulated by transmembrane interaction partners in cells. The SLO1 β-subunit β4 is expressed in mouse sperm, and might act as a chaperone for SLO3, increasing SLO3 surface expression without significantly modulating its functional properties (105). Recently, LRRC52, a newly discovered protein from the leucine-rich repeat containing family, has been reported to co-assemble with SLO3 in mouse sperm and to potentiate the pH sensitivity of SLO3 currents when expressed in heterologous systems (106).

1.2.5) SLO channels as therapeutic targets

Owing to their diverse physiological roles, SLO channels have long been recognized as important drug targets (107-110). In particular, the ubiquitous importance of SLO1 in smooth muscle physiology makes it an attractive candidate for the treatment of a wide range of disorders such as asthma, hypertension, urinary incontinence or erectile dysfunction (110). This is further emphasized by the discovery that human genetic variations in the SLO1 β1-subunit cause asthma (111) or can directly affect blood pressure regulation (112). Interestingly, some drugs currently on the market have been shown to act through molecular pathways dependent on SLO1: examples include β-adrenergic

agonists used for the treatment of asthma (113, 114), or phosphodiesterase inhibitors (e.g. Viagra) used against erectile dysfunction (115). In addition, SLO1 has also recently emerged as a regulator of different kinds of human cancers, and *in vitro* experiments have shown that SLO1 blockers can inhibit the proliferation of specific types of cancer cells (116, 117).

Overall, the physiological roles of SLO channels in cells highlight the central importance of intracellular activation for their function: these channels are expressed in cells where changes in intracellular Ca^{2+}, Na^{+} or pH are essential for activity. Moreover, the conserved architecture of SLO channels suggests similarities in their mechanism of action. My thesis work aims at understanding how SLO channels' function is regulated at the molecular level, and in particular probing how the effects of the Ca^{2+}, Na^{+} or pH_i translate into channel opening. In the next section, I will describe in more details our molecular and mechanistic understanding of SLO channels' function.

1.3 – SLO CHANNELS: FUNCTIONAL MECHANISMS

1.3.1) Domain architecture

What is already known about the mechanisms of SLO channel activation at the molecular level? In the absence of detailed atomic structures of SLO channels, it is difficult to understand precisely the molecular events leading to channel opening. However, insights about SLO channels' structure and mechanism can be drawn from the known structure of evolutionarily related K^+ channels, which I will detail in this section (for excellent reviews, see (118) and (21)).

As we have seen, each subunit of a tetrameric SLO channel can be divided into three functional domains: the voltage sensor and the pore embedded in the lipid bilayer, and the CyToplasmic Domain (CTD) (Figure 6). The pore is the basic unit of ion conduction and selectivity, and contains the channel's activation gate. Channel opening and closing is ultimately controlled by conformational changes happening in the pore. The function of the gating modules, voltage sensors and CTD, is to sense gating signals and transfer the corresponding energy to the pore domain to trigger opening in an allosteric manner. The pore, voltage sensor and CTD domains are related to different classes of channels for which structural data are available, and which shed light on the structure and function of SLO channels.

1.3.2) Pore domain and activation gate

The structure of the truncated bacterial K^+ channel KcsA, which is essentially an isolated pore domain, defines the basic principles of ion conduction and selectivity in all K^+ channels (119, 120). KcsA shows how protein

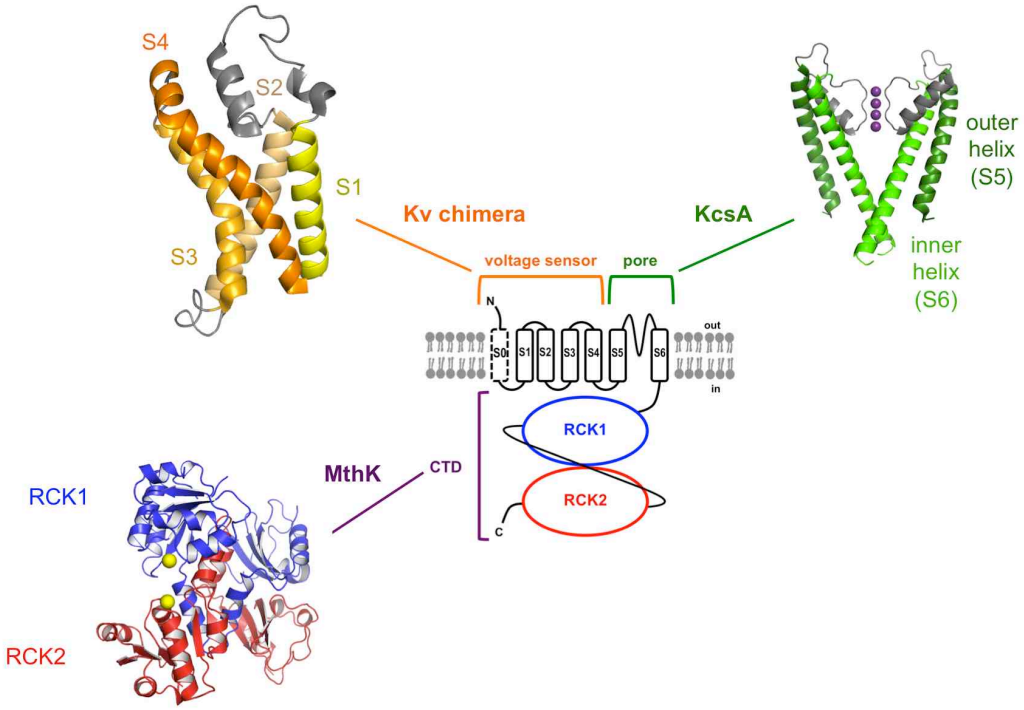

Figure 6: Structural homologs of SLO channels. For each SLO channel domain (voltage sensor, pore and CTD), a structural homolog is shown (respectively: voltage sensor from the paddle chimera Kv, PDB ID 2R9R, KcsA pore, PDB ID 1K4C, and MthK RCK domains, PDB ID 1LNQ). For KcsA, K^+ ions are shown in purple spheres, and the front and back subunits are removed for clarity. For MthK, Ca^{2+} is shown as yellow spheres.

residues provide a pathway allowing ions to cross the membrane: a central aqueous cavity stabilizes hydrated ions in the low dielectric environment of the lipid bilayer, and the selectivity filter close to the extracellular side acts as a gatekeeper responsible for K^+ selectivity. The precise geometry of the filter provides a polar environment mimicking the specific coordination of K^+ ions by water molecules, explaining how K^+ can move through at a rate close to their diffusion limit in water and why other ions such as Na^+, which prefer a different coordination, are excluded (120, 121).

Since the selectivity filter and the inner helices (S6 in SLO) of the pore are the only regions lining the ion pathway, they must contain the channel's activation gate that switches ion flow on or off. The crystal structure of the ligand-bound MthK, a bacterial Ca^{2+}-gated K^+ channel, provides a striking illustration of how the movement of the inner helices contributes to channel gating (122, 123). In the Ca^{2+}-bound, open conformation of the MthK structure, the inner helices are bent outwards providing a physical access to the inner cavity from the intracellular side (Figure 7) (123). In contrast, in KcsA the same helices form a narrow (~4 Å) hydrophobic bundle at the intracellular entry, forbidding the movement of K^+. Subsequent structural characterization of other K^+- or related channels reinforced the concept that the movement of inner helices is central to channel activation (124-131). In MthK, the open inner helices bend at a Gly residue ("Gly hinge") that is conserved throughout the K^+ channel family and is a major determinant of channel activation (123, 132).

How do these principles apply to SLO channels? All the relevant studies have so far focused on SLO1. Functional experiments revealed that, in SLO1, rearrangement of the inner helices occurs during the closed-to-open transition (133, 134). Importantly, two consecutive Gly are present in SLO1 at the position corresponding to the "Gly hinge" in MthK. Mutation of either Gly to Ala impairs

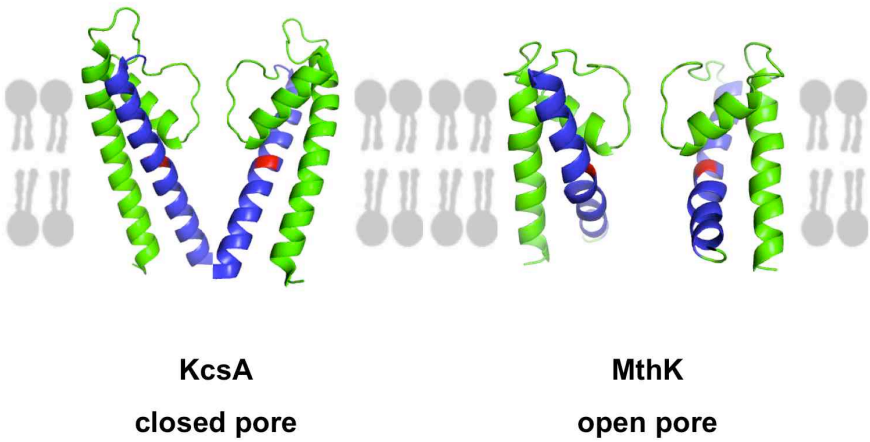

Figure 7: Closed and open pores in K^+ channel structures. The pore regions of the closed KcsA (PDB ID 1K4C) and the open MthK (PDB ID 1LNQ) are shown. In MthK, the inner helices (blue) splay open at a conserved Gly residue (red).

SLO1 opening, and in the double Ala mutant the voltage required to open the channel in 100 μM Ca^{2+} is shifted by ~ 130 mV to higher values (132). Thus, inner helix flexibility is an important aspect of SLO1 gating. Whether the same applies to SLO2 or SLO3 remains to be tested. Additionally, the precise conformational changes occurring in SLO1's inner helix during activation are still to be characterized (21, 133-136).

1.3.3) Voltage sensors

In canonical voltage-gated channels, functional and structural studies have revealed that voltage-sensing stems from the movement, in response to voltage changes, of positively charged amino acids ("gating charges") located in the S4 transmembrane helix (1, 137-142). Gating charge movement manifests itself in a measurable "gating current" prior to channel opening (143). Functional experiments coupling mutagenesis and gating current measurement in the archetypical *Shaker* voltage-gated K^+ channel identified the implicated residues in S4 (four Arg and one Lys), and established that each *Shaker* tetramer contains 12-14 gating charges, or ~3.5 per individual voltage sensor. The crystal structures of the bacterial KvAP and the eukaryotic Kv1.2 and Kv1.2/Kv2.1 "paddle chimera" channels define the molecular architecture of the voltage sensor in classical voltage-dependent K^+ (Kv) channels, and show that voltage sensors (S1 to S4) are essentially independent domains embedded in the lipid bilayer (124, 125, 141). The linker between S4 and the pore's outer helix, S5, provides the allosteric connection that translates voltage sensor movement into pore opening (138).

The voltage dependence of SLO1 and SLO3 likely originates from the same principles. Sequence analysis reveals that most of *Shaker*'s gating charge residues are conserved in SLO1 or SLO3 (94, 144). However, there is a discrepancy between this apparent conservation of number of charged residues

in S4 and the actual number of gating charges: gating currents have been measured in SLO1 (145), but quantitative measurements showed that SLO1 possess only 2-4 gating charges per tetramer (144, 145), compared to *Shaker*'s 12-14 (146, 147). Mutagenesis studies in SLO1 further showed that, in S4, only the last Arg (R213) carries a gating charge (144). Hence, the actual structure of the voltage sensors of SLO1 (and probably SLO3) is surely pretty divergent from that of canonical Kv channels. Another important difference is the presence in SLO1 and SLO3 of the additional transmembrane helix S0, which has been proposed to directly interact with the core of the voltage sensor domains based on mutagenesis and cross-linking experiments (148, 149).

Lastly, the voltage dependence of SLO2 remains largely unexplained since its S4 segment does not show any obvious conservation of positively charged residues, even though SLO2 currents are voltage-sensitive (90, 150).

1.3.4) CTD: tandem RCK domains and functional implications

The basic architecture of the large intracellular CTD is expected to be conserved among the different SLO channels, based on sequence conservation (151). An elegant proof that the CTD is the basic unit responsible for intracellular activation, and that CTDs from different SLO channels are indeed similar in structure, came from experiments using chimeras between SLO1 and SLO3. By swapping CTDs between SLO1 and SLO3, Lingle and colleagues showed that the CTD alone is responsible for the specific response to Ca^{2+} vs. pH_i: a chimeric channel with a SLO1 transmembrane domain (S0 to S6) and a SLO3 CTD becomes alkalization-activated but Ca^{2+}-insensitive, and vice versa (23).

It was first recognized by sequence analysis that the CTD is evolutionary related to a class of protein domains ubiquitous in prokaryotic K^+ channels and K^+ pumps: the RCK domains (for Regulating the Conductance of K^+) (24, 151-

154). The first snapshot of the RCK domain fold came from the crystal structure of the RCK domain from the *E. coli* K^+ channel (24), which also suggested that the functional RCK unit is formed by a dimer of RCK domains interacting through a large protein interface. A salt bridge can be seen in the structure, and is conserved in the sequence corresponding to RCK1 in SLO channels as demonstrated by mutant-cycle mutagenesis studies in SLO1 (24). This proved the existence of at least one RCK domain in the CTD of SLO channels. In-depth sequence analysis showed that another RCK domain (RCK2) could be found in the SLO CTD, so that the CTD actually contains a tandem of RCK domains (151, 151).

Subsequently, the structure of the prokaryotic Ca^{2+}-activated K^+ channel MthK offered the first picture of a full channel whose gating apparatus is formed by RCK domains (122). The sequence of MthK encodes only one RCK domain, but an alternative start site at the RCK N-terminus initiates the translation of a second identical RCK domain that assembles with the first, pore-attached RCK in the full channel, showing that dimerization is a trademark of RCK function (122) (Figure 8a). Moreover, in the MthK tetramer, four RCK dimers are seen to assemble in a "gating ring" at the intracellular surface of the membrane (122) (Figure 8a). The structure suggested a simple hypothesis for RCK-mediated gating in MthK: in response to Ca^{2+} binding, conformational changes at the RCK level cause a dilation of the gating ring, which in turn pulls the pore's inner helices to open the channel (122). This mechanism was later confirmed by crystallographic studies on an isolated MthK gating ring (without the pore domain) in which the Ca^{2+} binding site was disabled by mutation, most likely representing the "closed" conformation of the gating ring (155). Comparison of this structure with the original Ca^{2+}-bound, open gating ring shows that upon

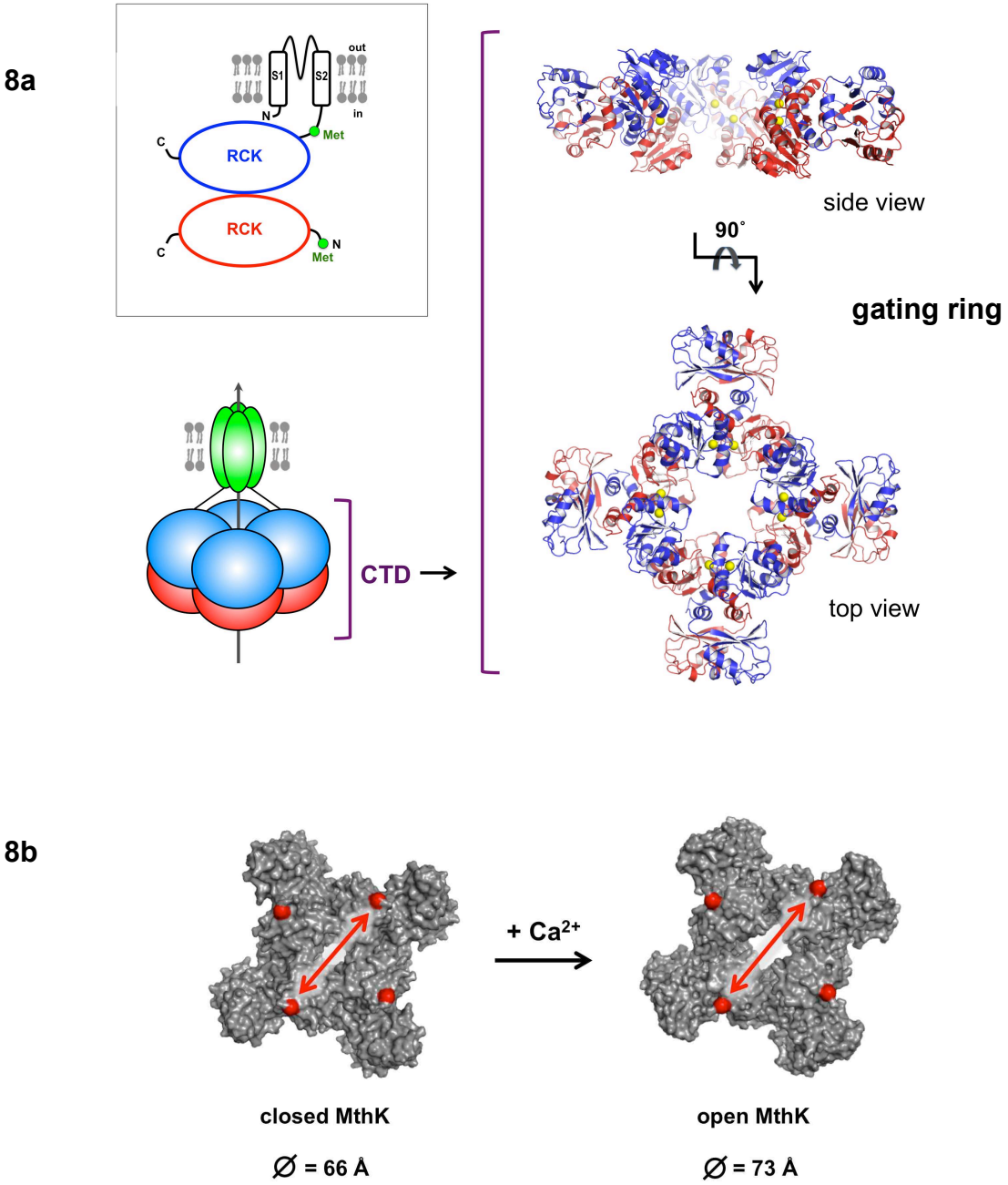

Figure 8: MthK gating ring. 8a) Structure of the MthK tetrameric gating ring (PDB ID 1LNQ). The topology of one subunit in shown in inset: the MthK CTD is made by the repeat of the same RCK domain. In all panels, RCK1 and RCK2 are color-coded blue and red, respectively. **8b)** Ca^{2+} causes the MthK gating ring to expand, leading to channel opening. The gating rings are seen from the top, and the red spheres mark the very N-terminal CTD residues, linked to the channel pore. PDB ID: 2FY8 (closed), 1LNQ (open).

Ca^{2+} binding the ring's diameter expands from 66 to 74Å, driving channel opening (122, 123, 155, 156) (Figure 8b).

The presence of a RCK tandem in SLO channels strongly suggests similarities in function with MthK. In addition, the "gating ring expansion" model predicts that the amino-acid linkers between the pore's inner helices and the RCK N-termini serve essentially as passive tethers transducing the mechanical force of gating ring dilation into channel opening. Functional experiments in SLO1 where the linker length was systematically modified support this model, showing that increase or decrease in the length, respectively, impairs or potentiates Ca^{2+}-driven activation, and that this effect varies linearly with length, the linker acting essentially as a spring (151, 157). Altogether, the structure and mechanism of MthK provides a basic framework for understanding the activation of SLO channels by intracellular signals.

1.3.5) Ca^{2+} activation in SLO1

What more is known about the functional mechanisms of SLO channel activation by Ca^{2+}, Na^{+} or pH_i? In particular, where in the CTD is the ligand binding site or sensor located? Here again, only SLO1 has been studied in detail. The first insight into the location of the Ca^{2+} binding site(s) in the SLO1 CTD took advantage of the different Ca^{2+} sensitivities of mouse and drosophila channels. Swapping RCK2 between the two channels established that this domain is responsible for the difference (158). More detailed mutagenesis analysis narrowed down the RCK2 sequence critical for Ca^{2+} activation: a stretch rich in Asp residues, absolutely conserved across species, named the "Ca^{2+} bowl" by the authors (^{889}QFLDQDDDDDPD^{900}, numbering corresponding to the human protein) (159). A systematic alanine scan of the whole Ca^{2+} bowl and flanking regions revealed that mutating two of the Asp (D895 and D897) had the most severe effect (160). Furthermore, radioactive assays in which $^{45}Ca^{2+}$ binding can

be detected on a RCK2 fragment containing the Ca^{2+} bowl (161, 162) showed that, in the double mutant D895A-D897A, $^{45}Ca^{2+}$ signal is reduced by 80%, further suggesting that the corresponding side chains might directly coordinate Ca^{2+} (160, 160). Another study involved chimeric SLO1/SLO3 channels (163). Replacing the RCK2 domain of SLO1 by the corresponding SLO3 sequence creates channels that are completely Ca^{2+}-insensitive. Now, in this background, introducing back a SLO1 region of 34 amino-acids encompassing the Ca^{2+} bowl restores most of the Ca^{2+} sensitivity (163). Thus, the calcium bowl appears to be the main Ca^{2+} binding site responsible for SLO1 activation.

However, the Ca^{2+} bowl is likely not the only Ca^{2+} binding site in SLO1. Indeed, deleterious mutations in the Ca^{2+} bowl sequence abolish most, but not all, of SLO1's Ca^{2+} sensitivity (159). In particular, SLO1 channels in which the Ca^{2+} bowl region (^{893}QDDDDDPD^{900}) is completely removed are still functional and Ca^{2+}-activated: raising [Ca^{2+}] from 3 nM to 10 μM Ca^{2+} causes a -80 mV shift in the midpoint of voltage activation (compared to -170 mV in *wt* channels) (164). The precise location of the other Ca^{2+} binding site(s) is still unknown. Three residues located in RCK1 have been implicated (D367, M513 and E535) (164-166). Mutating either of these residues to Ala almost abolishes the high-affinity (<10 μM) response to Ca^{2+} in the background of a Ca^{2+}-bowl-disabled SLO1 channel (164-166). However, whether these amino acids directly coordinate Ca^{2+} or act through an indirect effect is unresolved. In particular, direct biochemical evidence for Ca^{2+} binding in RCK1 is missing.

Importantly, none of the proposed high-affinity Ca^{2+} binding sites appear to match the binding sites seen in the MthK structure (122, 151). Hence, even though MthK and SLO1 likely share similarities in how conformational changes at the CTD level drive channel opening, the details of how the energy of Ca^{2+} binding is transduced into channel activation surely differ between the two channels.

1.4 – RESEARCH PROJECT

SLO channels: studying the structure to understand function

Overall, SLO channels are an important class of K^+ channels involved in a myriad of physiological processes ranging from muscle contraction to sperm motility. Understanding the gating of these channels is key to understanding the specific cellular functions controlled by their activity. The evolutionary link between the SLO family and other channels of known molecular structure provides a basic framework for understanding the gating mechanisms of SLO1, SLO2 and SLO3. However, as we have seen, the unique features of SLO channels (be it in terms of voltage- or intracellular activation) cannot be explained by simply drawing parallels between SLO channels and their distant relatives (21, 118, 151, 167). To really understand how SLO channels operate at the molecular level, a direct knowledge of the atomic structure of these proteins is needed. Such knowledge would pave the way for functional studies specifically designed to probe particular aspects of SLO channels' operation.

The goal of my Ph.D. work is to study the atomic structure of SLO channels, and to use this information to discover new aspects of how these molecular machines perform their function in cells. To this end, I used two experimental techniques: X-ray crystallography, which is a way to directly investigate the atomic arrangements of any molecule (in particular proteins); and electrophysiology, which allows the direct study of the function of ion channels by measuring the electrical currents they mediate.

In addition to the fascinating challenge of understanding the chemical and physical foundations of cellular functions (especially in the context of human physiology), this work is also motivated by its potential contribution to the

treatment of diseases. As we have seen, SLO channels (and in particular SLO1) are attractive drug targets. Structural information can be instrumental in the design and development of therapeutic molecules (168), as shown by the example of HIV protease inhibitors used for the treatment of AIDS (169, 170). Furthermore, the biochemical characterization and large-scale production effort that preludes any crystallographic analysis can also lead to the development of new tools for pharmacological studies.

The specific questions I decided to study relate to the distinctive, key property of SLO channels: their activation by intracellular signals. Can we understand how binding of an ion, or a change in pH, modulate these proteins to promote channel opening? Since SLO1, SLO2 and SLO3 are closely related, do they share the same principles of activation? For example, do Ca^{2+}, Na^{+} and pH_i act on the same site(s) in the three homologs, or did evolution make use of different opportunities within the same basic protein scaffold?

As we will see, structural studies of eukaryotic proteins as complex as SLO channels constitute an important technical challenge, and I was very fortunate to work on this project alongside two very talented scientists: first and foremost Peng Yuan, a post-doc, whose excellent expertise and mentorship was central to the work I will present; and Yichun Hsiung, a research assistant, whose skillfulness was essential for dealing with the large amount of cell culture that this project required. All the data I will describe in this dissertation are fundamentally the result of our team effort.

In my thesis, I will describe our effort to characterize structurally SLO channels, as well as to use this structural knowledge to probe fundamental aspects of how SLO channels function, in particular how channel activation is mediated by ligand binding or pH change at the intracellular level. In the next chapter, I will present our endeavors to crystallize entire SLO channels, and my work on developing methods to express large quantities of full-length SLO1 channels in eukaryotic heterologous systems, and to purify these proteins while making sure they retain full functionality. Using a specific toxin-binding assay as a probe, I will show how expression and purification of functional SLO1 is highly dependent on the choice of expression system, but can be achieved in insect or mammalian cell lines.

In the subsequent chapters, I will describe our results on determining the atomic structures of isolated CTDs from SLO1 and SLO3. In Chapter 3, we will look at two structures of the human and zebrafish SLO1 CTDs, solved by Peng in the presence of Ca^{2+}. We will see how, together with studies from other laboratories, these structures illustrate how the binding of Ca^{2+} in the SLO1 CTD changes the conformation of the protein to open the channel pore. In Chapter 4, I will describe the structure I solved of the human SLO3 CTD and present electrophysiological results that explain the molecular mechanisms of pH sensing in mammalian SLO3 channels. In the final discussion, I will compare these different structures together and examine how they define new unique properties of SLO channels regulation by intracellular signals, and discuss the evolutionary relationship of RCK-mediated ion channel gating.

CHAPTER TWO:

EXPRESSION OF FULL-LENGTH SLO CHANNELS IN EUKARYOTIC HETEROLOGOUS SYSTEMS

As we have seen, direct knowledge of the atomic structure of SLO channels is required to understand the precise molecular events controlling gating in these proteins. X-ray crystallography is the primary experimental method to obtain structural information of proteins at the atomic scale. An X-ray crystallography experiment involves two major steps: first, one must find suitable conditions to obtain three-dimensional crystals of the protein of interest; then, the atomic details of these crystals are probed under an X-ray beam, and the resulting data are processed into an atomic structure of the proteins forming the crystal. The major bottleneck in X-ray crystallography is to obtain protein crystals. Crystallization of proteins follows the same principles of crystallization as for any molecule or mineral. To crystallize, a molecule in solution needs to be brought above its solubility limit: the solution then becomes supersaturated and metastable, leading to precipitation or, if the right conditions are met, crystallization. The most common way to reach the solubility limit is to increase the concentration of the molecule.

Thus, crystallizing proteins typically requires high concentrations of starting material. In practice, this means that large quantities of proteins need to be obtained. To this end, two options are available. The first one is to make use of a natural tissue where the protein is enriched. The other option is to force the expression of the protein in a heterologous system. Heterologous expression is often the method of choice in present-day crystallography because it allows one to work with proteins for which no practical natural source is available (as is the case for SLO channels) and it allows tailoring the protein of interest to facilitate its subsequent purification and crystallization.

Crystallography of membrane proteins presents unique challenges. First, heterologous over-expression of membrane proteins is particularly difficult, due to the complexity of membrane protein folding and the limited area of the cell

membrane (171, 172). Second, current biochemical techniques require that membrane proteins be extracted from the native lipid bilayer in a water-soluble form, typically by solubilizing the hydrophobic transmembrane core in a detergent micelle (173). Eukaryotic membrane proteins such as SLO channels are even more difficult to work with, and the first eukaryotic membrane protein structure obtained using heterologous expression was solved only recently, in 2005 (1).

The first goal of my Ph.D. work was to develop methods for the large-scale production and purification of SLO channels, the necessary first step of any crystallographic undertaking. In this chapter, I describe my efforts to express functional SLO1 channels in three different systems commonly used for eukaryotic protein expression (172): *Pichia pastoris* yeast, *Sf9* insect cells and human HEK cell line. As a first approach to probe the functionality of the purified proteins, I developed techniques to screen whether purified SLO1 channels obtained from these different expression systems are able to bind a specific toxin molecule that recognizes only properly folded SLO1 tetramers. I will show that SLO1 channels expressed from HEK or *Sf9* cells, but not from *Pichia* yeast, are competent to bind the toxin and are indeed fully functional.

2.1 – HETEROLOGOUS EXPRESSION OF SLO CHANNELS

2.1.1) Eukaryotic expression systems

I tested three eukaryotic systems for the heterologous over-expression of SLO channels: the yeast *Pichia pastoris*, *Sf9* insect cells and HEK human cell line (172). Each system has its own specificities. Yeast can be grown in large quantities using fairly inexpensive media, and *Pichia* cells in particular can reach very high density compatible with fermentor culture (up to >100 g dry weight of cells per liter of culture) (174). Yeast cells can carry out most, but not all, post-translational modifications common to animal cells. *Pichia* is capable of producing membrane proteins at high level. However, the lipid composition of the *Pichia* membrane is quite different from that of a typical animal cell (for example, yeast lack cholesterol). The first eukaryotic membrane protein structure obtained using heterologous expression (the mammalian Kv1.2 potassium channel) made use of the *Pichia* system (125). On the other hand, *Sf9* or HEK cells are *bona fide* animal cells that can be used for protein over-expression, but require expensive cell culture media (172). HEK cells offer the most native environment for the expression of mammalian membrane proteins, but these epithelial cells are best grown attached on a surface, which limits large-scale production efforts in practice. *Sf9* insect cells can be conveniently grown in shaker flasks, and are often the system of choice for eukaryotic protein expression (172).

2.1.2) Screening of SLO candidates using FSEC

I proceeded to screen the SLO family for candidates amenable for large-scale production and purification. Typically, a good membrane protein candidate for crystallization must fulfill three criteria: 1) have a sufficiently high yield of

expression in the system of choice, 2) be stable, i.e. not prone to rapid degradation upon purification and 3) be homogeneous, i.e. give rise to a monodisperse species upon extraction from the lipid membrane by detergent solubilization (175). FSEC (Fluorescent Size Exclusion Chromatography) is a powerful method to screen for such candidates (175). In an FSEC experiment, the protein of interest is fused to a GFP (Green Fluorescent Protein) molecule and the biochemical behavior of the protein-GFP construct is followed by fluorometry within the whole cell lysate, so that only small amounts of material are needed and no purification is required. After cell lysis and detergent extraction, the protein-GFP fusion is loaded on a gel filtration column that separates molecules according to their size (size exclusion chromatography). A protein that is stable and homogeneous will typically elute as a single, sharp peak on FSEC (175).

In an initial screen, I tested 9 different SLO1, SLO2 or SLO3 channels from different species for expression in *Pichia*, *Sf9* or HEK, the rationale being that differences in protein sequence between species can have a big impact on the ability of a protein to crystallize. These candidates represented all SLO channels that had been cloned at the time (y. 2006), except for mammalian SLO1 channels, which share extremely high amino-acid sequence identity (for example, sequences from mouse and human SLO1 are 96% identical): for this clade, the human SLO1 was chosen as a representative candidate. This initial screen identified three promising candidates: SLO1 channels from human and the sea slug *Aplysia californica*, and the rat SLO2.2. Representative FSEC profiles for these three channels, expressed in HEK cells, are shown in Figure 9a. Expression in *Sf9* or *Pichia* gave identical results (data not shown). A representative candidate that did not pass the FSEC test (*Caenorhabditis elegans* SLO1) is shown in Figure 9b. A close inspection of the data in Figure 9a reveals interesting differences in the biochemical behavior of the three promising candidates: *Aplysia* SLO1 (AcSLO1)

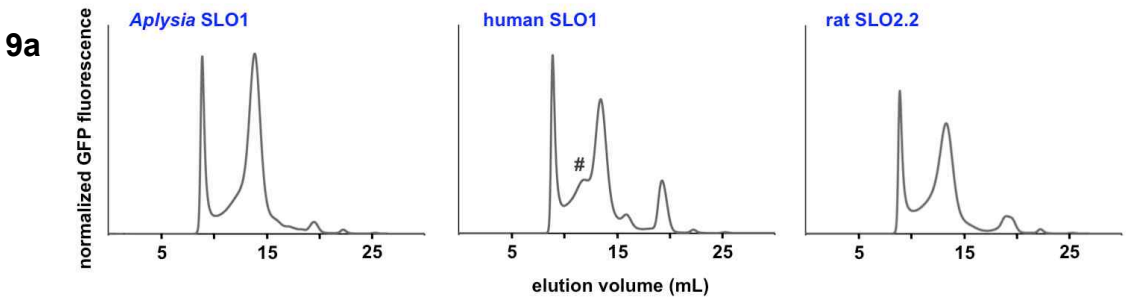

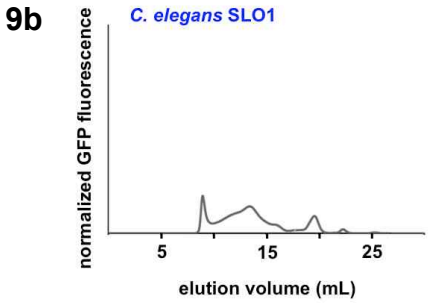

Figure 9: FSEC screening in HEK cells. SLO channels were expressed in HEK cells as C-terminal GFP fusions, and the crude DDM-solubilized cell lysate was loaded on a Superose 6 gel filtration column, monitoring GFP fluorescence. All traces are at the same scale. **9a)** Best candidates. The hSLO1 profile shows signs of non-specific aggregation: a "shoulder" left of the main peak (#). **9b)** Example of a bad candidate.

and rat SLO2.2 elute as single, monodisperse peaks, whereas the human SLO1 (hSLO1) gel filtration profile shows a high-molecular weight "shoulder" on the left of the main peak, sign that the solubilized hSLO1 channel has a tendency to aggregate. In terms of expression level, the yield for rat SLO2.2 is half compared to that of AcSLO1.

Based on these initial results, I decided to focus on the two SLO1 candidates (AcSLO1 and hSLO1). AcSLO1 appeared to be the most promising target, and the hSLO1 FSEC profile was encouraging enough to pursue, considering that the structure of a human protein would have the biggest impact on our understanding of human physiology and on new therapeutic possibilities.

2.1.3) Large-scale production and purification of AcSLO1 and hSLO1 channels

Large-scale production and purification of *Aplysia* AcSLO1 and human hSLO1 were carried out using the *Pichia* and *Sf9* systems. The purification was done in three steps: 1) *Pichia* and *Sf9* cells expressing AcSLO1 or hSLO1 were lysed either mechanically (*Pichia*) or by sonication (*Sf9*) and membrane proteins were extracted using n-dodecyl-β-D-maltoside (DDM) or n-decyl-β-D-maltoside (DM) detergents; 2) the solubilized SLO1 channels were isolated from the crude cell lysate by affinity chromatography; and 3) the channels were further purified in a final gel filtration step. To facilitate affinity purification, I engineered an affinity tag within the protein constructs. Initial attempts using a C-terminal poly-His tag gave samples of low purity because of the relatively low expression yield of hSLO1 or AcSLO1 in *Pichia* and *Sf9*: in this case the non-specific binding of background contaminants to the affinity resin was too high. High purity was achieved using a C-terminal 1D4 tag (TETSQVAPA), for which very specific monoclonal antibodies are available. Some of the constructs I used also contained a C-terminal GFP between the SLO1 sequence and the affinity tag, so that the

channel construct can be easily followed by fluorometry at different steps during purification. In order to remove the C-terminal 1D4 tag or GFP-1D4 tag prior to crystallization, a protease cleavage site was added to the construct following the SLO1 sequence. Two different cleavage sites were compared: a thrombin site and a site recognized by the PreScission protease. Only PreScission showed specific cleavage restricted to the engineered site, whereas thrombin treatment led to additional non-specific proteolysis (data not shown). Schematics of the final optimized expression constructs, obtained by fusing a PreScission site-1D4 tag or a PreScission site-GFP-1D4 tag to the SLO1 C-terminus, are shown in Figure 10a.

By growing large cultures of *Pichia* or *Sf9* cells, AcSLO1 and hSLO1 channels could be purified in milligram quantities (final protein yield per liter of culture for either AcSLO1 or hSLO1: ~0.3 mg in *Pichia*; ~0.2 mg in *Sf9*). Gel filtration profiles from the final purification step are shown in Figure 10b and 10c (DDM was used as detergent). Three important characteristics can be seen in these profiles. First, the gel filtration behavior of channels obtained from *Pichia* or *Sf9* cultures is essentially identical (compare Figures 10b and 10c). Second, the elution volume of the main peak is consistent with purified channels being in a tetrameric form. This was confirmed by chemical crosslinking experiments (see Figure 10d showing the example of hSLO1 purified from *Pichia*, but the same was observed with proteins purified from *Sf9*). Third, both AcSLO1 and hSLO1 exhibit signs of non-specific aggregation, which manifests itself as a "shoulder" on the left of the main tetramer peak. When the tetramer peak is isolated, concentrated and re-loaded on the gel filtration column, the channel further aggregates, with hSLO1 behaving worse than AcSLO1 in this respect (Figure 10b). Over time, the isolated AcSLO1 tetramer peak will aggregate as well and display a visible "shoulder" on gel filtration (data not shown).

Overall, this large-scale purification effort seemed promising: AcSLO1 and hSLO1 could be purified in quantities compatible with crystallization efforts, and the channels were purified in their native oligomeric state. Before starting intensive crystallization efforts, I decided to probe whether the purified channels were also still fully functional.

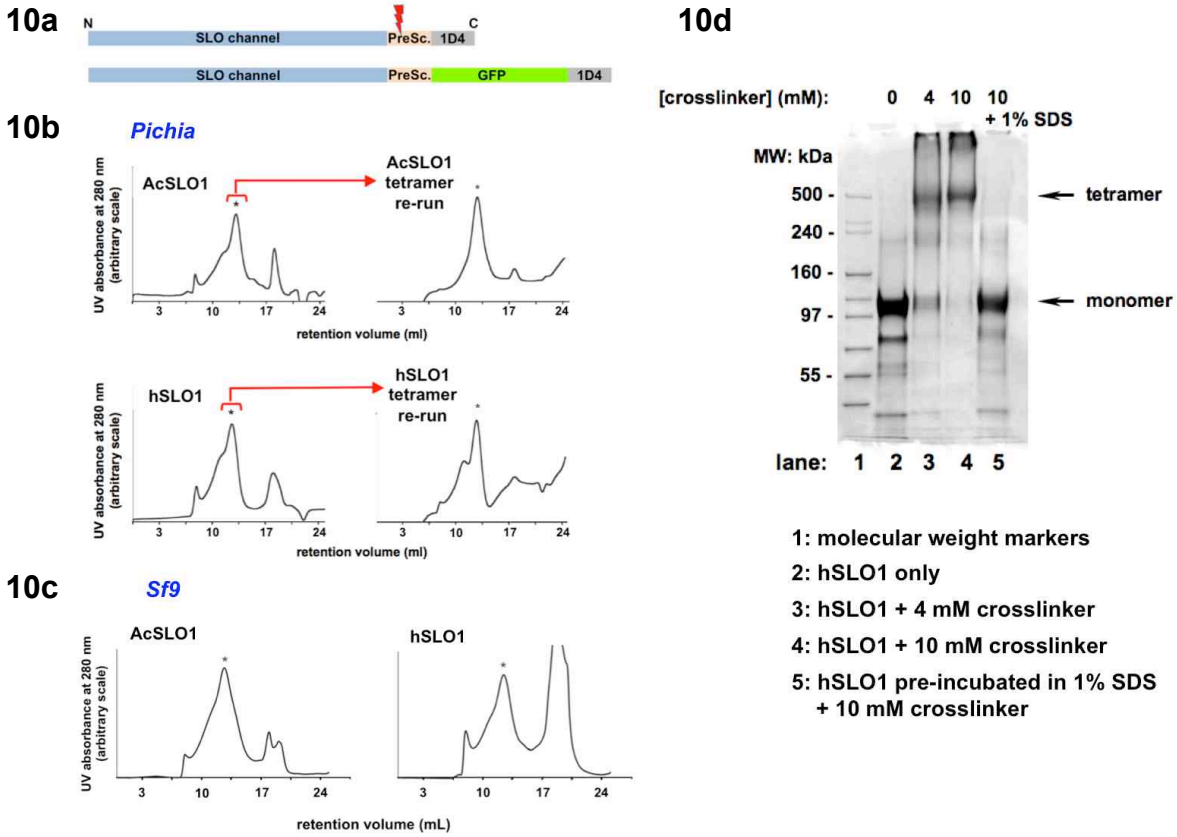

Figure 10: Expression and purification of SLO1 channels. 10a) Constructs used for large-scale protein expression: C-terminal fusions containing PreScission site-1D4 tag or PreScission site-GFP-1D4 tag (see text). PreScission protease is used to remove the added C-terminal sequence during purification (red). **10b)** Gel filtration profiles of AcSLO1 and hSLO1 purified from *Pichia*, solubilized in DDM (Superose 6 column). Peaks corresponding to SLO1 tetramers (asterisks) were isolated, concentrated and re-loaded on the column ("re-run"). **10c)** Same as in 10b) showing AcSLO1 and hSLO1 purified from *Sf9* expression. Peaks eluting at 17-20 mL mostly contain GFP. **10d)** SDS-PAGE showing chemical crosslinking of the isolated hSLO1 tetramer peak from *Pichia* expression. Increasing concentrations of disuccinimidyl glutarate were used for crosslinking. The SDS-PAGE was stained with Coomasie.

2.2 – FUNCTIONAL STUDIES OF PURIFIED SLO1 CHANNELS

2.2.1) Toxin binding as a probe of SLO1 functional state

The absolute test to probe whether a purified ion channel retains its full functional state is to reconstitute the solubilized channel into a lipid bilayer from which ion channel function can be directly assessed by electrophysiology (176, 177). However, this method is time- and protein-consuming. Instead, I decided to first study the ability of purified AcSLO1 and hSLO1 to bind toxins recognizing specifically the native state of the channels. Natural peptides found in the venom of scorpions have been shown to act as high-affinity blockers of K^+ channels (178). These "pore-blocker" toxins occlude ion conduction in cells by binding to the channel's extracellular mouth, at the interface between the four subunits of the pore (Figure 11) (178, 179). Toxins can be extremely specific for a particular kind of K^+ channel, and toxin binding is a powerful tool to assess whether a given channel retains its native state upon purification (180). Several toxins from the charybdotoxin (ChTx) family, including ChTx itself, target SLO channels (178). In particular iberiotoxin (IbTx), isolated from the venom of the Indian red scorpion *Buthus tamulus* by the team of Maria Garcia at Merck Research Laboratories, is a specific blocker of SLO1 (181). I therefore performed IbTx-binding assays to study the biochemical properties of AcSLO1 and hSLO1 expressed in heterologous systems.

2.2.2) ^{125}I-IbTx binding assays on DDM-solubilized hSLO1

Maria Garcia and her colleagues have extensively studied binding of ChTx and IbTx (the two toxins have nearly identical properties) to membrane-embedded as well as solubilized hSLO1 (182, 183). Their standard protocol

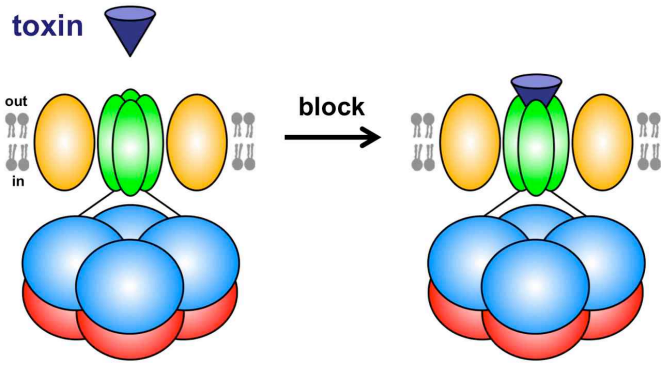

Figure 11: Pore-blocker toxins. Toxins from scorpion venom occlude ion conduction by binding at the extracellular interface between the channel's four subunits.

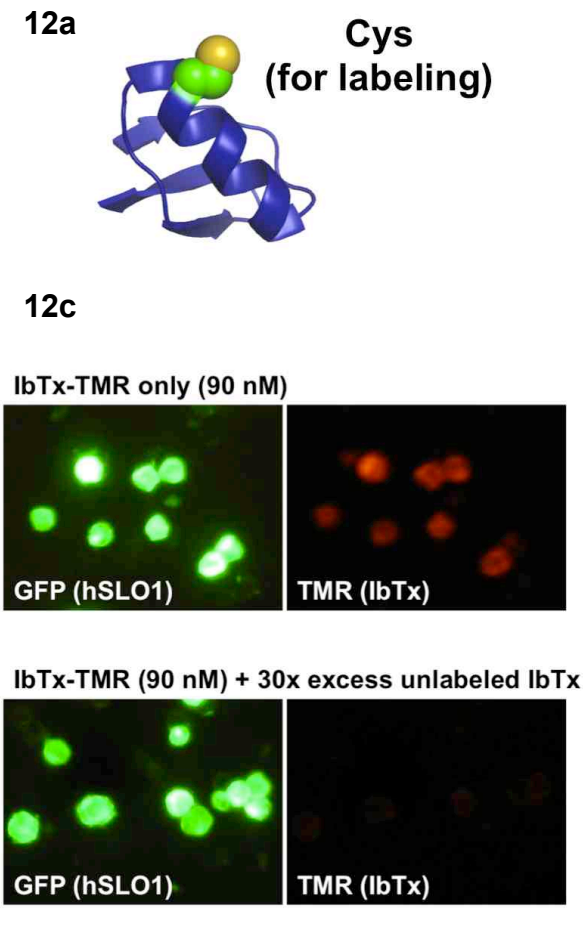

Figure 12: Labeling of IbTx-D19C. 12a) Position of the introduced Cys (shown as spheres) in the toxin molecule. **12b)** HPLC profile of the last purification step from *E. coli* expression (see Material and Methods). The main peak corresponds to pure IbTx-D19C (asterisk). **12c)** HEK cells expressing GFP-tagged hSLO1 (green) were incubated with 90 nM IbTx-D19C fluorescently labeled with tetramethylrhodamine (TMR, red). A competition assay in the presence of large excess of unlabeled IbTx shows that the binding is specific.

makes use of toxin derivatives radiolabeled with ^{125}I by iodination on Tyr residues. In a binding assay, solubilized hSLO1 or membrane preparations containing hSLO1 are incubated with ^{125}I-ChTx or ^{125}I-IbTx, and the toxin-receptor complex is recovered by filtration on treated glass filters, which are then counted for ^{125}I γ radiation (1).

Electrophysiology experiments done in extracellular salt conditions close to physiological levels (90 mM Na^+ and 2.5 mM K^+) show that ^{125}I-IbTx blocks hSLO1 with a K_D of ~1.5 nM, almost identical to native IbTx (K_D ~1 nM) (183). However, binding affinity can be increased by removing all external K^+ and using an extracellular buffer of very low ionic strength. Using a buffer containing only 10 mM NaCl and 20 mM TRIS-HCl pH 7.4 (+ 0.1% BSA to limit non-specific binding), ^{125}I-IbTx binds *in vitro* to membranes containing hSLO1 with a K_D of ~5 pM (183). These specific conditions (0 K^+ and low ionic strength) have been used in all toxin binding studies published so far, because the very high affinity allows using minimal amounts of radiolabeled toxin.

Toxin binding on solubilized hSLO1 has been studied using the same conditions. The Garcia lab showed that picomolar ^{125}I-ChTx binding on solubilized hSLO1 could be achieved using digitonin as a detergent, but not DDM (182). Digitonin is an unusual detergent that interacts with membrane cholesterol and solubilizes membrane proteins along with an annulus of phospholipids (184). Digitonin is very expensive, toxic and difficult to obtain in a pure and homogeneous form, all of which undermine its practical use for membrane protein crystallization (185, 186). On the other hand, mild glycosydic detergents such as DDM or DM are well-suited and very commonly used for crystallization efforts (186).

With the help of Maria Garcia and her colleagues, I attempted to reproduce their findings using DDM-solubilized hSLO1 obtained from *Pichia* or

Sf9 expression. Indeed, under the standard 0 K^+ and low ionic strength conditions, we could not detect any picomolar ^{125}I-IbTx binding to these samples (data not shown). Does this mean that, in DDM micelles, solubilized hSLO1 is denatured in a non-native, toxin-insensitive form? This would be a significant drawback for our crystallographic undertaking. However, I reasoned that another phenomenon could explain these results. It is known that, at least in detergent micelles, the selectivity filter of K^+ channels changes its conformation depending on K^+ concentration (120). At low [K^+] (~2 mM), the crystal structure of KcsA shows that the selectivity filter adopts a "collapsed" conformation drastically affecting the geometry of the K^+ binding sites (120). Interestingly, it is known that pore-blocker toxins such as ChTx or IbTx bind in the immediate vicinity of the filter's K^+ sites (178, 187). Hence, it is possible that, in the standard ^{125}I-toxin binding protocol using non-physiological K^+-free conditions, the conformation of hSLO1 is affected in a way that prevents toxin binding (most probably due to a conformational change in the channel's selectivity filter). To test this hypothesis, I needed to perform toxin-binding studies in the presence of K^+.

2.2.3) Development of a K^+-compatible IbTx binding assay

In practice, ^{125}I-IbTx cannot be used to study toxin-channel interactions in the presence of K^+. This is because the synthesis of large quantities of radioactive ^{125}I-IbTx is quite inconvenient, so that its usage is limited to conditions where toxin binding has picomolar affinity (i.e. 0 K^+, low salt conditions), thus allowing the use of very low quantities of material. I thus decided to develop a new IbTx binding assay, which would be compatible with K^+-containing buffers.

Toxins from the ChTx family can be recombinantly expressed in bacteria, and introducing a Cys residue at position 19 (on the toxin's upper surface) allows

for specific labeling of the toxins without compromising their binding capabilities (188, 189) (Figure 12a). Using protocols originally described for ChTx (188), I could produce and purify the Cys mutant IbTx-D19C expressed in *E. coli* (see Materials and Methods section). An HPLC profile of the final purification step is shown in Figure 12b. IbTx-D19C can be labeled on the introduced cysteine and the labeled toxin binds hSLO1 with high affinity. An example is shown on Figure 12c: IbTx-D19C labeled with the red fluorophore tetramethylrhodamine (TMR, using a Cys-reactive maleimide conjugate) specifically binds HEK cells expressing hSLO1 (toxin concentration: 90 nM).

To study IbTx binding on solubilized hSLO1, I first covalently linked IbTx-D19C onto a Cys-reactive iodoacetyl agarose resin. The IbTx-coated resin could then be used to pull-down solubilized hSLO1, and test the influence of $[K^+]$ on the channel-toxin interaction. The results of such pull-down experiments are shown in Figure 13a. In these experiments, hSLO1-GFP was solubilized from HEK cells using either digitonin or DDM. The crude cell extract was then incubated with IbTx resin, and hSLO1 binding to the resin was revealed by SDS-PAGE, looking at GFP fluorescence. Figures 13a and 13b shows the requirement of K^+ for toxin binding on DDM-solubilized hSLO1; on the contrary, when digitonin is used, binding occurs independently of K^+ concentration. Interestingly, for IbTx binding in DDM, K^+ must be present during solubilization itself: adding K^+ to hSLO1 solubilized in a K^+-free buffer does not rescue binding (Figure 13b). In the case of AcSLO1, the wild-type protein does not bind IbTx due to a sequence variation at the toxin receptor site (190). However, I could confer IbTx binding to AcSLO1 by introducing, by mutagenesis, the hSLO1 sequence corresponding to the expected receptor site (190) (a total of 7 mutations, see Figure 13c). This mutant AcSLO1 (which I will from now on refer to as AcSLO1^T,

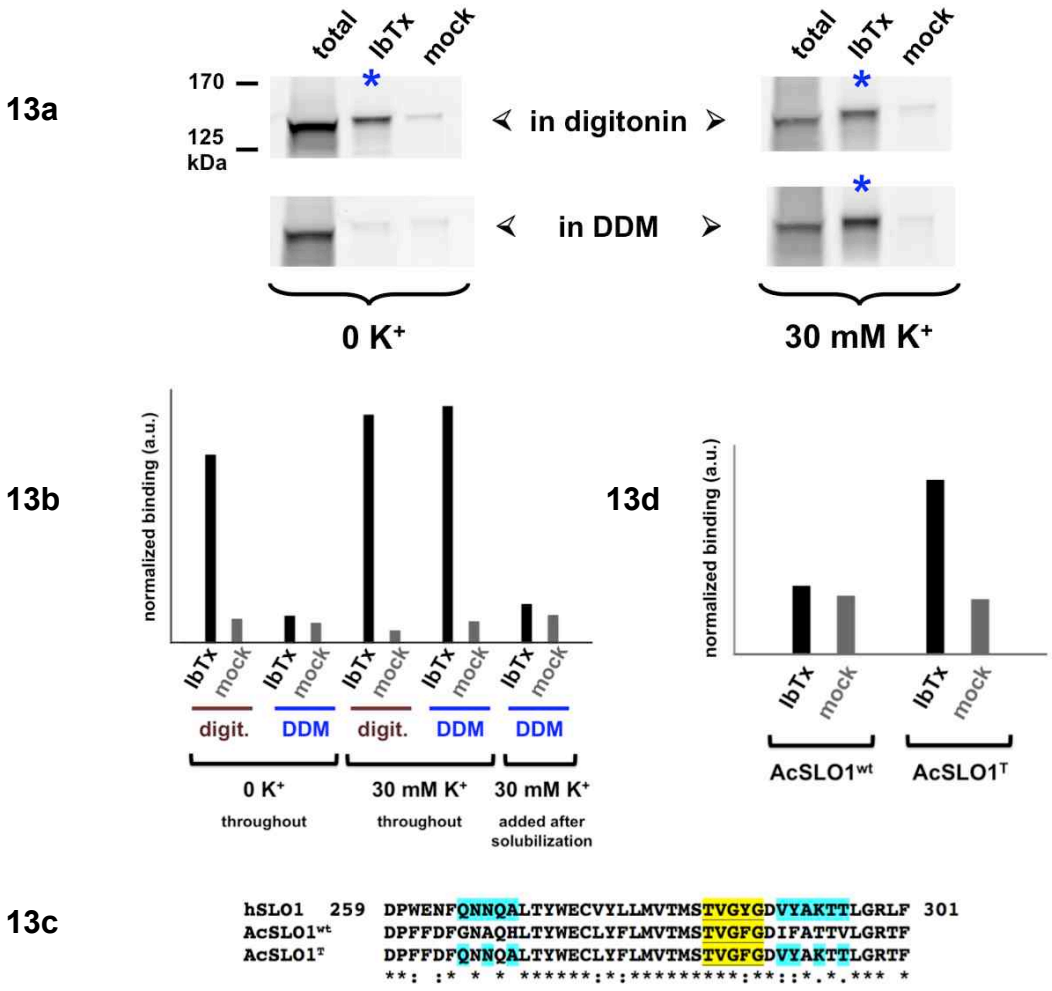

Figure 13: SLO1 pull-down on IbTx resin. 13a) IbTx-coated agarose resin binding to hSLO1-GFP solubilized in either digitonin or DDM. SDS-PAGE revealed by GFP fluorometry are shown. Each panel shows three lanes: total solubilized hSLO1 ("total"); hSLO1 bound to IbTx-coated agarose resin ("IbTx"); non-specific binding to agarose resin not conjugated to IbTx ("mock" beads). Both hSLO1 solubilization and resin binding are carried out in buffer containing either 0 K^+ or 30 mM K^+. **13b)** Densitometry quantification of experiments as in 13a). hSLO1 was solubilized in either digitonin or DDM. Specified K^+ concentrations are used during both solubilization and resin binding (0 or 30 mM, "throughout"), or during resin binding only (30 mM, solubilization carried out in 0 K^+). Binding is normalized to total solubilized material. **13c)** Sequence alignment showing the mutations introduced in $AcSLO1^T$ to confer toxin sensitivity (cyan). The selectivity filter sequence is shown in yellow. Numbers correspond to hSLO1 sequence numbering. **13d)** Same as 13b) showing normalized binding of $AcSLO1^{wt}$ and IbTx-sensitive $AcSLO1^T$. Channels were solubilized in DDM in the presence of 30 mM K^+.

for toxin) binds to IbTx resin when solubilized in DDM in the presence of K^+ (Figure 13d).

Overall, the IbTx-resin pull-down experiments proved that SLO1 channels can indeed be solubilized in DDM and still bind IbTx, provided that high enough [K^+] is present. These results gave a qualitative analysis of IbTx binding on solubilized SLO1.

2.2.4) Quantitative IbTx binding on purified SLO1 from *Pichia* and *Sf9* expression

To truly assess the functional state of purified SLO1 channels obtained from *Pichia* or *Sf9* large-scale expression, a quantitative assay was needed. In essence, I wanted to answer the following question: what proportion of channels can be purified in a toxin-binding competent, presumably native state? To this end, I turned to radioligand binding assays.

I labeled IbTx-D19C with ^{14}C-N-ethylmaleimide, a commercially available Cys-reactive radioactive probe, following protocols already described for similar experiments with ChTx (188). ^{14}C labeling was essentially complete: the specific activity I measured for the labeled ^{14}C-IbTx using spectroscopic absorbance at 280 nm (A_{280}) to calculate toxin concentration was in excellent agreement with the expected value (measured: 31.5 ±0.3 Ci/mol, expected: 33.2 Ci/mol). Importantly, I could easily produce large quantities of ^{14}C-IbTx, compatible with binding assays for which binding interaction is in the nM range.

With this tool in hand, I performed quantitative ^{14}C-IbTx binding assays on purified SLO1 channels from *Pichia* and *Sf9* expression. I used a protocol that was essentially identical to the ^{125}I-IbTx experiments I described previously: ^{14}C-IbTx was incubated with solubilized channels and the toxin-channel complex was recovered on treated glass filters, extensively washed in ice-cold buffer and ^{14}C β radiation was measured by scintillation counting (see Materials and

Methods section). hSLO1 and AcSLO1 channels purified from *Sf9* showed robust IbTx binding using this assay: a representative example is shown in Figure 14, using toxin-sensitive AcSLO1^{T} solubilized in DM. By using A_{280} to calculate the concentration of purified SLO1 used to set up these assays, I could quantify that at least ~60% of the expected receptors bound to ^{14}C-IbTx in DM micelles. It is hard to know if this number means that a fraction of purified channels is in a toxin-insensitive state, or if it results from practical limitations of incomplete protein recovery on the glass filters and/or errors in estimating protein concentration (I used a theoretical calculation for the extinction coefficient ε_{280}).

For SLO1 channels expressed in *Pichia*, the results were drastically different: when the same experiments were performed, no binding could be detected (data not shown). This was further confirmed using the qualitative pull-down assays on IbTx-coated resin. Whereas SLO1 expressed in *Sf9* showed robust binding to the resin, no binding could be detected with *Pichia*-expressed channels (data not shown).

2.2.5) Functional reconstitution of SLO1 channels expressed in *Sf9*

The IbTx-binding studies suggested that DM- or DDM-solubilized SLO1 channels produced in *Sf9*, but not *Pichia*, could be purified in a native state. To further confirm the functional state of the purified proteins, I reconstituted these channels in lipid vesicles (POPE:POPG 3:1) and studied their function by electrophysiology in an artificial lipid bilayer system. SLO1 channels from *Sf9* were indeed fully functional since channel activity could be recorded (Figure 15). In the case of *Pichia* expression, I could never see any electrophysiological activity despite repeated reconstitution attempts (data not shown). Hence, it seems that only *Sf9*, and not *Pichia*, is suitable for the large-scale heterologous

Figure 14: ^{14}C-IbTx binding to purified AcSLO1^{T} in DM micelles (from *Sf9* expression). Toxin-channel complexes were recovered by filtration. The experiment was set up with 100 nM channels. Each point is the mean of two measurements (shown ± range). Data were fitted to a binding isotherm.

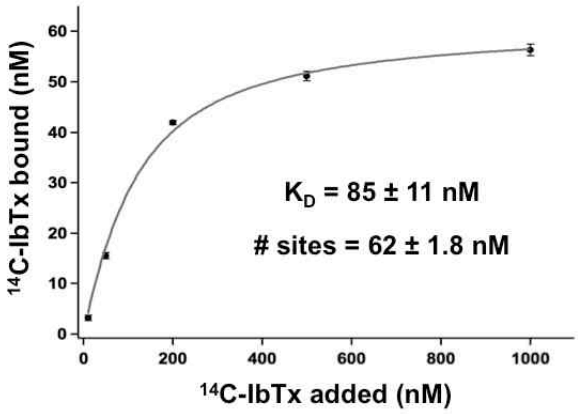

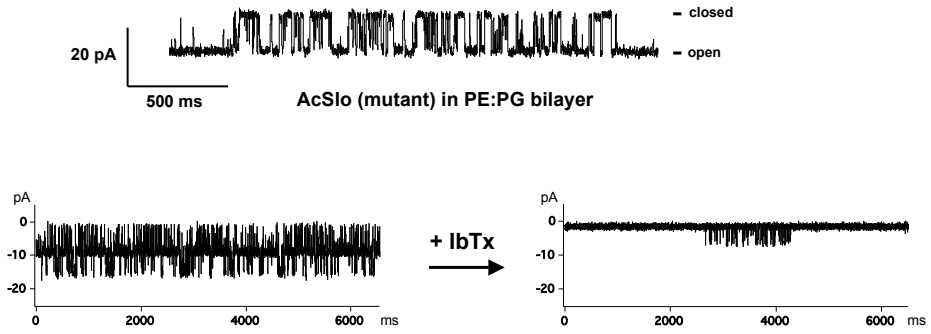

Figure 15: Electrophysiological recordings of reconstituted AcSLO1^{T} from Sf9 expression. Recordings were made in symmetrical 150 mM KCl, holding at + 150 mV. Channel activity was blocked by adding 200 nM IbTx to the external side.

expression of functional SLO1 channels (HEK cells are also an option, since SLO1 from HEK expression binds IbTx in pull-down assays, as I presented in Figure 13). This result was surprising and interesting, since *Pichia* is routinely used in our laboratory for the expression of eukaryotic K^+ channels. I will discuss this finding in more details in the discussion section at the end of this chapter.

2.3 – PROGRESS TOWARDS A SLO CHANNEL STRUCTURE

Altogether, the functional studies on purified SLO1 showed that *Sf9* insect cells are a suitable heterologous expression system for crystallographic studies of SLO channels. This works paves the way for the study of SLO channel atomic structure by X-ray crystallography. However, despite our endeavor, we have been so far unable to obtain crystals of AcSLO1 or hSLO1. As I will present in the next chapters, our immediate effort later switched to crystallographic studies on the SLO intracellular CTD, which led to important new insights on SLO channel functional and gating mechanisms. The crystal structure of a full SLO channel remains a major goal of research in our laboratory. In this section, I would like to quickly summarize results I obtained while trying to crystallize AcSLO1 or hSLO1, which I believe are significant for any future crystallization studies of SLO1 channels.

2.3.1) SLO1 proteolysis and truncation studies

Purified SLO1 channels are quite sensitive to proteolysis. Even in a typical purification procedure, where special care is taken to limit proteolysis to a minimum (inclusion of a very diverse protease inhibitor cocktail during cell lysis, keeping the temperature at 4°C or below during all stages of purification), proteolytic cleavage can be seen (Figure 16a). Treatment with specific proteases further reveals this sensitivity. The example of limited proteolysis with chymotrypsin is shown in Figure 16a: no robust, proteolysis-resistant protein core can be seen on SDS-PAGE (the same applies to many other common proteases: trypsin, elastase, subtilisin, Glu-C, Lys-C and Arg-C).

Sensitivity to proteolysis is often associated with the presence of poorly structured regions in a protein. SLO channels are very big proteins (~1100 residues per monomer) and contain many loops between secondary structure elements that are expected to be surface-exposed and disordered (151). Such poorly structured regions are typically a problem for crystallization because they create structural heterogeneity at the protein surface. In limited proteolysis studies, I could identify the long linker (~100 amino acids, see Figure 16b) between RCK1 and RCK2 as a major proteolytic site (data not shown). Interestingly, it is known that most of this linker can be removed without affecting channel function by co-expressing in *trans* a construct containing the transmembrane and RCK1 domains together with a construct containing RCK2 on its own (a simple deletion within a single construct does not work, surely because the linker bridges together two very distant parts within the protein) (151, 158). When I tested such co-expression with hSLO1 in HEK cells, the results looked fairly promising: the different domains assemble in the expected complete tetramer in a peak sharper than the wild-type protein itself (Figure 16c).

Additionally, I could show that the unstructured N- and C-termini as well as a long (~40 amino acids) unstructured loop in the middle of RCK2 could be removed without affecting the biochemical behavior of purified SLO1 (data not shown). Previous studies have shown that none of these parts are essential for function (151). Altogether, truncations of these parts, as well as truncation of the RCK1-RCK2 linker in a co-expression strategy, could facilitate crystallization by limiting structural heterogeneity.

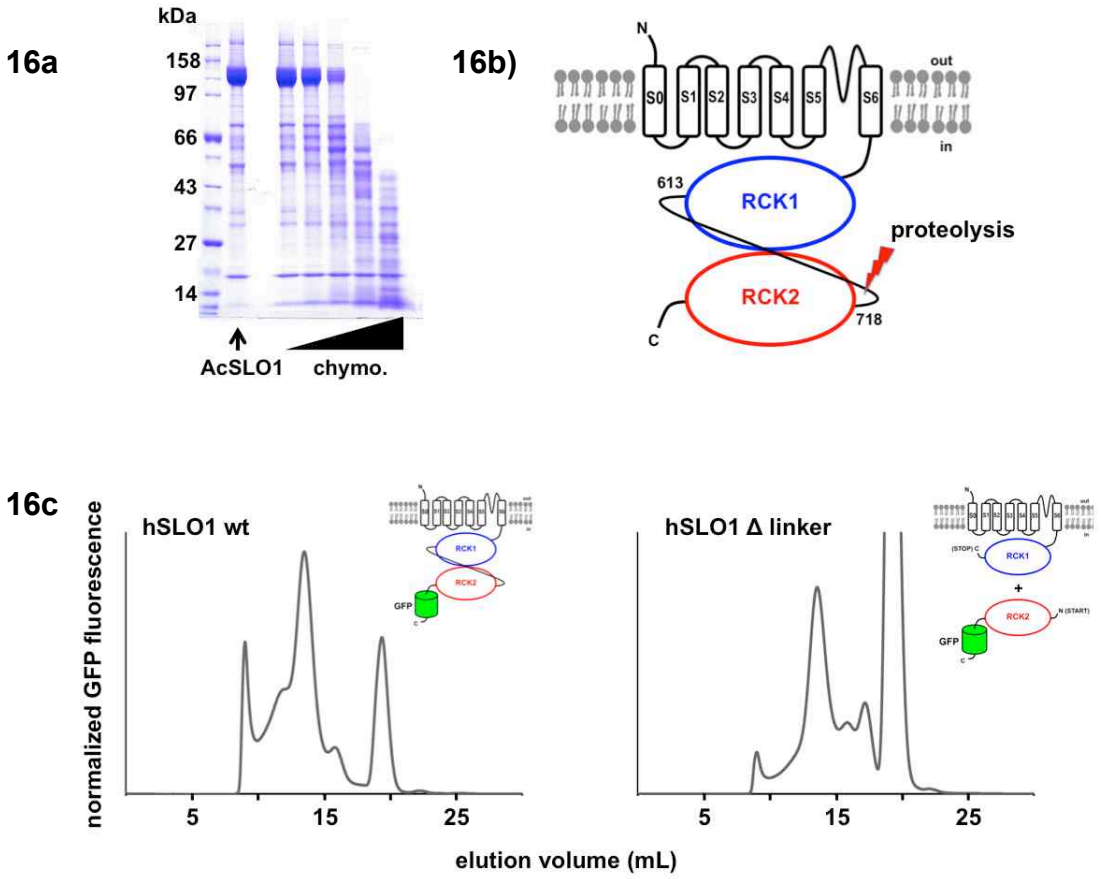

Figure 16: SLO1 proteolysis and RCK1-RCK2 linker deletion. 16a) AcSLO1 limited proteolysis. SDS-PAGE showing purified AcSLO1 from *Sf9* expression. Adding increasing concentrations of chymotrypsin does not reveal an obvious stable, protease resistant core. **16b)** The long RCK1-RCK2 linker is a major proteolytic site. **16c)** The RCK1-RCK2 linker can be removed using a strategy where two moieties of the SLO1 molecule are expressed in *trans* (insets). Shown are FSEC profiles from hSLO1 expression in HEK cells (Superose 6 column). The two traces are at the same scale. Upon linker removal, the whole hSLO1 channel still assembles as a proper tetramer. Interestingly, the hSLO1 tetramer elutes as a peak sharper that wild-type. The species eluting after 16 mL contain excess RCK2-GFP and free GFP.

2.3.2) Effect of divalent cations on SLO1 gel filtration behavior

The addition of ligand can often stabilize a purified protein. Ca^{2+} of course, but also Mg^{2+}, activate SLO1 (21). Adding high concentrations of Ca^{2+} and Mg^{2+} improved the behavior of purified SLO1 on gel filtration (Figure 17). I have not studied this effect in a systematic way, but the presence of divalent cations could be important for the stability of purified SLO1.

2.3.3) Choice of detergent for purification

The right choice of detergent, specific to each membrane protein, is often crucial for crystallization (186). I compared the gel filtration behavior of purified SLO1 channels in a large array of different detergents. Alkyl and Cymal maltosides, as well as polyoxyethylene glycol detergents gave similar gel filtration profiles, whereas glucosides (typically more dispersive) made the protein unstable (data not shown). Interestingly, the use of zwitteronic detergents such as amine-oxides or zwittergents improved gel filtration behavior. In particular, the profiles in LDAO or Zwittergent 3-12 seemed quite promising (Figure 20). Importantly, the elution volumes in LDAO or Zwittergent 3-12 suggested that SLO1 channels were still tetrameric in these detergents. However, functional studies need to be performed to insure that the use of these detergents preserves the channels in a functional state.

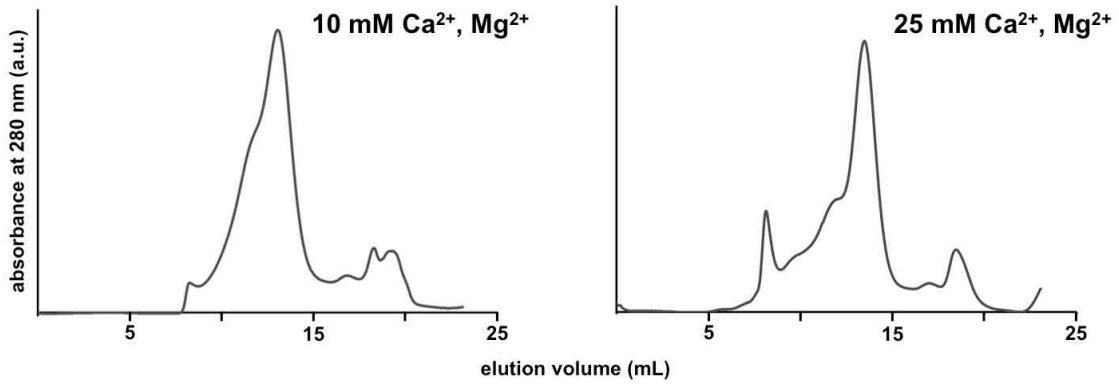

Figure 17: Effect of Ca^{2+} and Mg^{2+} on purified SLO1 gel filtration profile. Shown are gel filtration profiles (Superose 6 column) of purified AcSLO1 from *Sf9* expression. The two samples come from the same protein preparation. Addition of high concentration of divalents cations (Ca^{2+} and Mg^{2+}) improves the gel filtration behavior of AcSLO1: the elution peak is sharper and more monodisperse.

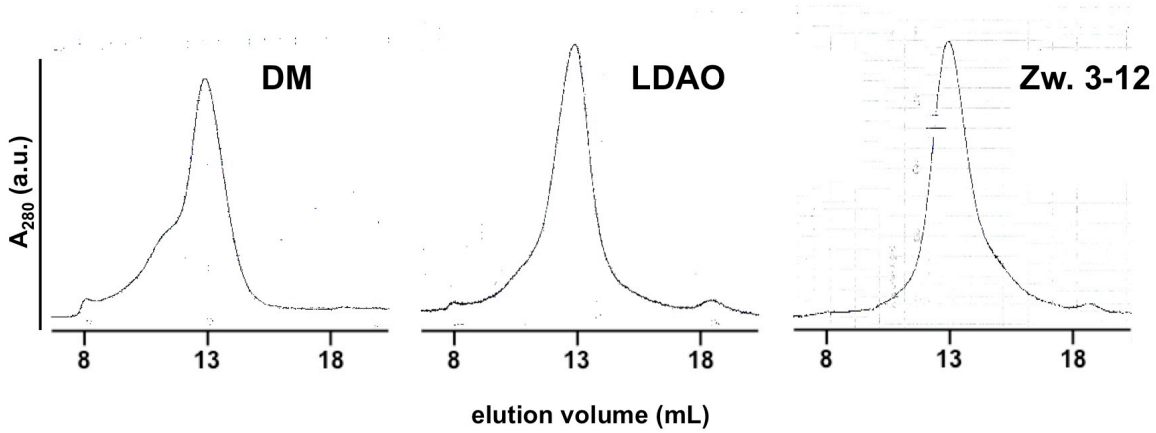

Figure 18: Comparing detergents for SLO1 solubilization. Shown are gel filtration profiles of purified AcSLO1 solubilized in DM, Zwittergent 3-12 or LDAO. All samples come from the same protein preparation. Zwitterionic detergents (Zw. 3-12, LDAO) improve the gel filtration behavior of AcSLO1.

2.4 – DISCUSSION

Expression of SLO channels in heterologous systems and purification

In summary, I have explored the heterologous expression of SLO channels in three different systems: HEK, *Pichia* and *Sf9* cells. Initial screens revealed that human and *Aplysia californica* SLO1 channels are promising targets for crystallization efforts. Large-scale expression in *Pichia* and *Sf9* led to the purification of milligram quantities of tetrameric hSLO1 or AcSLO1 solubilized in DM or DDM micelles. However, quantitative toxin binding studies revealed a major difference between these two expression systems. Purified SLO1 from *Sf9* expression bound IbTx, and electrophysiological studies on reconstituted proteins confirmed that the channels are indeed fully functional. On the other hand, SLO1 channels purified from *Pichia* expression did not bind IbTx and showed no functional activity when reconstituted in lipid membranes. What could explain this discrepancy?

I can think of three possibilities that would explain the absence of toxin binding and functional activity of SLO1 purified from *Pichia*: 1) *Pichia* yeast cells are not able to process and fold SLO1 channels, which only exist in the Metazoa kingdom. However, the fact that SLO1 from *Pichia* expression have their expected oligomeric form would suggest that this possibility is unlikely. Furthermore, the gel filtration behavior of proteins expressed in *Pichia* and *Sf9* is identical; 2) SLO1 from *Pichia* expression actually co-purifies with a yeast-specific contaminant that impedes toxin binding and functional activity. In theory, a small molecule binding strongly to the channel's extracellular mouth could physically prevent toxin binding and occlude ion flow. I have not studied whether any such species is present in the SLO1 purified samples, but this could

be done, for example by using mass spectrometry. This second explanation seems quite improbable, but cannot be entirely ruled out; 3) SLO1 function as well as toxin binding require the presence of a specific cofactor, for example from the cell membrane, that is lacking is yeast cells. This third possibility is by far the most reasonable.

The membrane composition of yeast cells is quite different from that of animal cells. For example, yeast completely lack cholesterol, which is an essential component of animal membranes. Instead, the yeast membrane is rich in another sterol, ergosterol (191). Studies of mammalian G-protein coupled receptors (GPCR) have shown that ergosterol and cholesterol, even though very similar in structure, do not have the same functional properties. In the case of the human μ-opioid GPCR, ergosterol cannot be substituted for cholesterol to promote protein function, and μ-opioid receptors are expressed in yeast in an inactive form, which does not bind classical agonists (192). Interestingly, adding cholesterol to the yeast membrane restores agonist binding and function (192). This example illustrates how the functional properties of membrane proteins expressed in yeast can be impaired by the singular composition of the yeast lipid membrane. No specific lipid requirement for SLO1 function has been described, but cholesterol itself could be a candidate. It is indeed interesting that digitonin, which is known to directly interact with cholesterol (and presumably solubilizes membrane proteins along with a small cholesterol-containing patch of membrane), has a very unique effect on SLO1 solubilization. Overall, probing whether SLO1 channels interact with specific components of the cell membrane is an important physiological question. The methods I developed, which for the first time allow large-scale purification of functional SLO1 channels, could open the way for such studies by providing an experimental system in which the precise molecular composition can be controlled.

CHAPTER THREE:

CRYSTAL STRUCTURES OF THE Ca^{2+}-BOUND SLO1 CYTOPLASMIC DOMAIN AND MECHANISM OF Ca^{2+} GATING

While still working on crystallizing a full-length SLO channel, we decided to also explore another strategy. As I described in Chapter 1, the gating of SLO channels by intracellular signals (Ca^{2+} for SLO1, Na^{+} for SLO2, pH for SLO3) is at the core of their physiological functions. Since intracellular activation of SLO channels is controlled by their large cytoplasmic domain (CTD) (23), we decided, together with my close collaborator and mentor Peng, to study the atomic structure of isolated CTDs from different SLO channels using X-ray crystallography. We reasoned that this structural information could teach us a lot about the molecular basis of SLO channel gating. In particular, we wanted to specifically address two questions: What kind of conformational change occurs in the CTD upon ligand binding or pH change in order to promote channel opening? How do the activation mechanisms of SLO1, SLO2 and SLO3 compare to one another?

To this end, Peng and I decided to screen SLO1, SLO2 or SLO3 CTDs from different species to identify the best candidates for crystallization. Based on the results from expression of full-length channels, we expressed constructs in *Sf9* as C-terminal PreScission-GFP-His_{10} fusions. Most CTDs we tested could be readily expressed. Together, we identified several promising targets from SLO1, SLO2 and SLO3 that crystallized in initial screens. Refining these crystals to diffraction-quality was challenging, and we decided to share the effort. Peng focused on SLO1, whereas I concentrated on SLO3.

Together with our co-worker Hsiung, who helped us with cell culture, and under Rod's continuous guidance, we solved three CTD crystal structures: a monomeric, Ca^{2+} bound structure of the human SLO1 (hSLO1) CTD (published in (193)); a tetrameric, Ca^{2+}-bound structure of the zebrafish SLO1 (zSLO1) gating ring (published in (194)); and a tetrameric structure of the human SLO3 (hSLO3)

gating ring. In this chapter, I will describe the structures we obtained of the SLO1 CTDs.

The first structure we solved, the monomeric hSLO1 CTD, defines for the first time the precise molecular organization of a SLO channel intracellular domain. Even though in our crystals the hSLO1 CTDs did not assemble in a gating ring, we could infer the tetrameric, functional organization of the hSLO1 domains by using low-resolution diffraction data from a SLO2.2 crystal. This oligomeric assembly was later confirmed by the structure of the hSLO1 gating ring solved by the laboratory of Youxing Jiang at UT Southwestern. This structure, solved in the absence of Ca^{2+}, defines the ligand-free, "closed" conformation of the SLO1 gating ring. To understand how the binding of Ca^{2+} in the SLO1 CTD changes the conformation of the protein, we solved the tetrameric gating ring structure of the zebrafish SLO1 CTD bound to its ligand. I will show how, together, these results illustrate how a Ca^{2+}-driven conformational change in the SLO1 CTD could translate into the opening of the channel transmembrane pore.

3.1 – STRUCTURE OF THE HUMAN SLO1 Ca^{2+} ACTIVATION APPARATUS

3.1.1) Crystallization and structure determination

Residues 341 to 1056 of the human SLO1 sequence were expressed in *Sf9* cells. This construct comprises the entire hSLO1 CTD, from the expected first structural element, with the exclusion of 57 amino acids at the very C-terminus that are predicted to be unstructured and are not essential for function (151). The protein was purified and crystallized in the presence of a high concentration of Ca^{2+} (50 mM). The native crystals diffracted X-rays to a resolution of 3.0 Å and belonged to space group $P6_322$, with one monomer per asymmetric unit. Experimental phases to 3.3 Å were derived from a multi-wavelength anomalous diffraction experiment with a selenomethionine-containing crystal, and the final structure was refined to $R_{work}/R_{free} = 0.25/0.28$ (Table 1).

3.1.2) Global structure of the hSLO1 CTD

The hSLO1 CTD crystallized in a monomeric form. The structure, shown in Figure 19a, reveals for the first time the precise molecular organization of the SLO1 intracellular domain. In particular, the structure shows unequivocally that the hSLO1 CTD is formed by a tandem of RCK domains (RCK1 shown in blue, RCK2 in red), as was originally predicted by sequence analysis (24, 122, 151) but was still matter of debate in the field (195). A salt-bridge interaction between the side chains of K448 and D481, which was originally identified as a signature of the presence of RCK1 in the SLO1 CTD (24), can be seen in the structure (Figure 19a). Similar to what is seen in the bacterial MthK channel, each RCK domain has a bi-lobed shape (Figure 19b): a large N-terminal lobe with a Rossman fold, and a smaller C-terminal lobe. These two lobes are linked by a helix-turn-helix

connector (αF-αG in RCK1 and αS-αT in RCK2) that forms the main interface in the RCK1-RCK2 tandem (Figure 19c). This interface is reminiscent of the "flexible interface" created through the dimerization of two separate identical RCK domains in MthK (122).

3.1.3) The Ca^{2+} bowl

Because of the uncertainty and disagreement in sequence-based models of the SLO1 channel CTD, there have been different proposals for the placement of the main SLO1 Ca^{2+} binding site, the Ca^{2+} bowl, in RCK2 (151, 195). The hSLO1 CTD structure reveals for the first time the precise location of the Ca^{2+} bowl (^{889}QFLDQDDDDDPD^{900}) between the last two β strands (βO and βP, see Appendix A) of the RCK2 N-terminal lobe. Interestingly, the position of the Ca^{2+} bowl within the hSLO1 CTD is in sharp contrast with the Ca^{2+} binding sites of MthK (Figure 19d). Whereas in MthK Ca^{2+} binds on the RCK1-RCK2 "flexible interface", in hSLO1 the Ca^{2+} bowl is positioned on the side of RCK2 (Figure 19a).

The experimental electron density for the Ca^{2+} bowl contained less detail than most of the experimental map, but the main chain was continuous, and certain side chain features emerged with cycles of model building and refinement (Figures 20a, 20b). The model was built on the basis of crystallographic data alone, independently of information from prior mutational studies. Interestingly, an atom that is more electron-dense than carbon, nitrogen, or oxygen accounted for the strongest electron density at the center of the Ca^{2+} bowl (Figure 20b): we attributed this density as a Ca^{2+} ion, given its presence at 50 mM concentration in the crystallization solution. Atoms making direct contact with the Ca^{2+} ion include two main-chain carbonyl oxygen atoms from Q889 and D892 and oxygen atoms from the side-chain carboxylate groups of D895 and

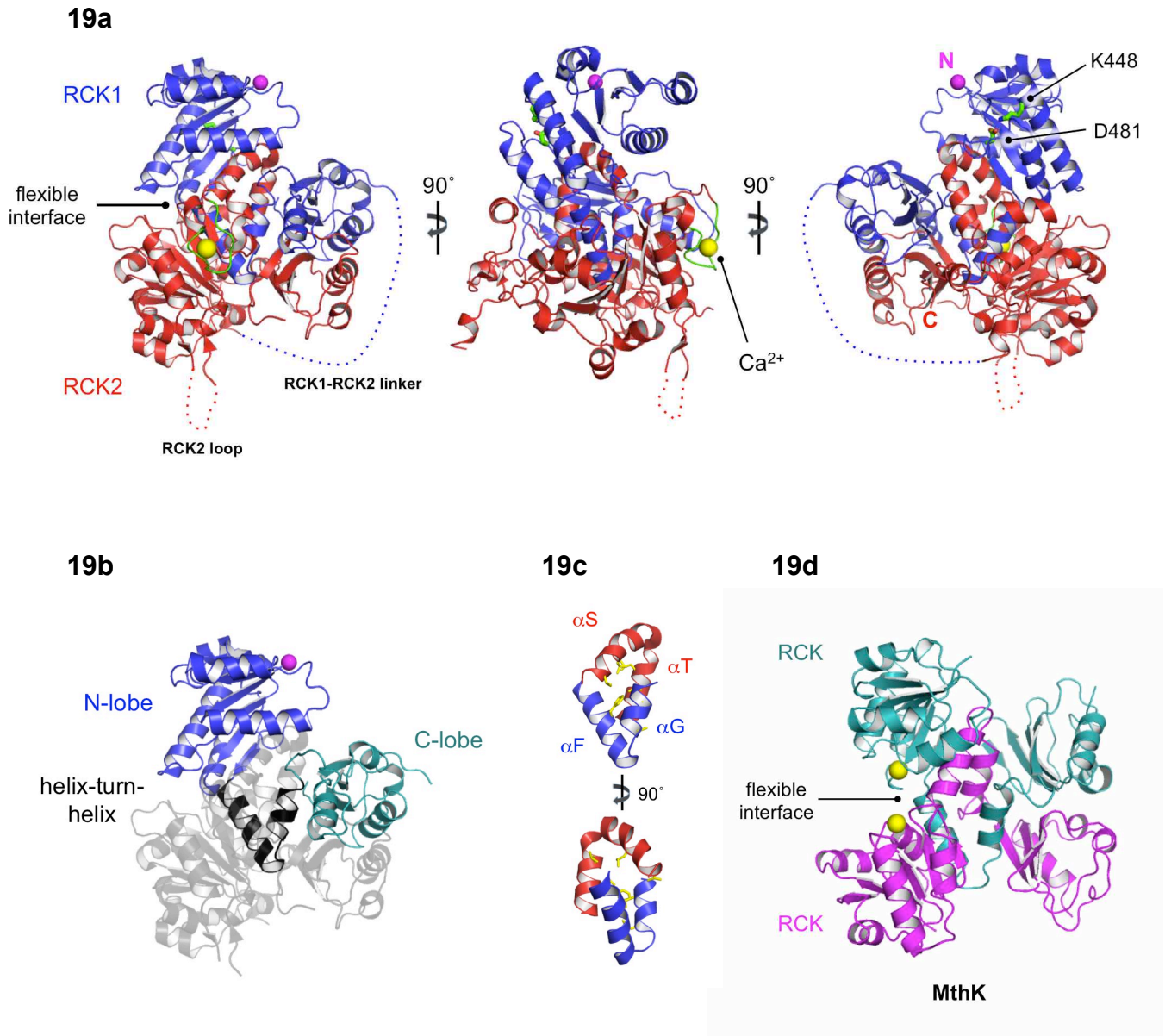

Figure 19: Monomer structure of the human SLO1 CTD. 19a) Cartoon representations of the hSLO1 CTD showing RCK1 in blue and RCK2 in red. The Ca^{2+} bowl is colored in green, and the Ca^{2+} ion is shown as a yellow sphere. Large disordered segments are indicated as dashed lines. The N-terminal residue (K343), connecting to the transmembrane ion-conduction pore, is shown as a magenta sphere. **19b)** Sub-domain organization of RCK1. The organization of the RCK2 domain is identical. **19c)** Close-up view of the αF-αG/αS-αT "flexible" interface. **19d)** Ca^{2+} binding sites in the bacterial MthK channel (PDB ID 1LNQ).

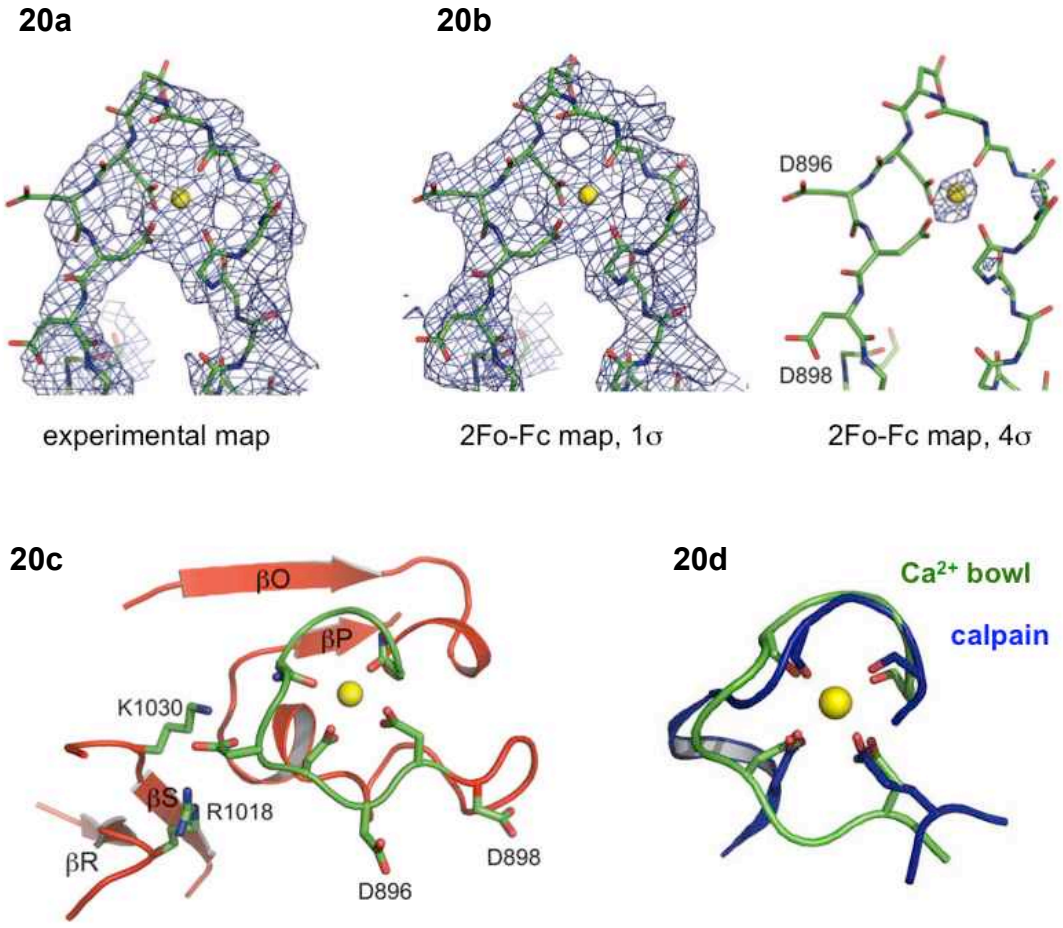

Figure 20: The Ca^{2+} bowl. 20a) Experimental electron density at 3.3 Å in the Ca^{2+} bowl region contoured at 1.0 σ. **20b)** Weighted 2Fo-Fc electron density at 3.0Å after refinement contoured at 1.0 σ and 4.0 σ. The final refined model is shown as sticks, with most side chains removed for clarity. **20c)** Structure of the Ca^{2+} bowl, showing key residues coordinating the Ca^{2+} ion (yellow sphere). **20d)** Superposition of the Ca^{2+} bowl and the Ca^{2+} binding site from the calpain-1 catalytic subunit (blue) (PDB ID 2R9F). The Ca^{2+} ion is shown as a yellow sphere.

D897 (Figure 20c). In searching the protein database of known structures, we observed a similar geometry of Ca^{2+} binding in a high-resolution crystal structure of calpain, which is an intracellular cysteine protease whose activity is regulated by Ca^{2+} (Figure 20d).

Our unbiased model for the Ca^{2+} bowl structure explains very well the results of in-depth Ala scanning mutagenesis studies of this region (1). The two most critical residues for Ca^{2+} activation, D895 and D897, are both directly involved in the coordination of the Ca^{2+} ion in the X-ray structure (Figure 20c). The third most effective mutation involved D894, which is not in direct contact with Ca^{2+} but forms salt bridges simultaneously with R1018 and K1030 in the C-terminal lobe of RCK2. D894 probably plays an important role in stabilizing the conformation of the Ca^{2+} bowl. The mutation D896A, on the other hand, had almost no effect on the channel's sensitivity to Ca^{2+} (160). In the X-ray structure, this side chain is directed out and away from the Ca^{2+} ion and does not make other protein contacts.

3.1.4) Quaternary assembly of the hSLO1 gating ring

In our hSLO1 crystals, the CTD is monomeric. However, we expected, by comparison with RCK-containing bacterial channels such as MthK, that in a SLO1 channel the CTDs from the four subunits assemble in a tetrameric "gating ring" at the intracellular face of the membrane (21, 122). Can we infer, from our monomeric hSLO1 CTD structure, the quaternary assembly of the hSLO1 gating ring?

To address this question, we used data from another SLO CTD that we could crystallize: the Na^+-activated chicken SLO2.2 (gSLO2.2) CTD. We purified and crystallized the gSLO2.2 CTD (amino acids 347 to 1201) in the presence of 500 mM Na^+. On gel filtration, the CTD eluted as a tetramer, and even under the

dispersive conditions of SDS-PAGE, the majority of protein migrates as a tetramer. Thus, the gSLO2.2 CTD forms a very stable tetrameric complex. The crystals diffracted X-rays to a resolution of 6 Å and were of space group I422, with one monomer (subunit) in the asymmetric unit (Table 1). Using a poly-Ala model of the hSLO1 CTD, we obtained a single outstanding solution in molecular replacement against the gSLO2.2 diffraction data. This solution indicates that the hSLO1 and gSLO2.2 CTDs must have very similar structures. By applying the crystallographic symmetry operators, we obtained the tetramer structure of the hSLO1 CTD (Figure 21a). This objective solution reveals the quaternary organization of subunits but not its exact atomic details because the resolution is low and the data are from the SLO2.2 homolog.

Importantly, the biological relevance of the SLO1 gating ring assembly is supported by previous functional studies. The "assembly interface" between RCK1 and RCK2 from two adjacent hSLO1 subunits has been studied by double-mutant cycle mutagenesis, and several amino-acid pairs have been shown to interact (151, 196). These amino acid pairs, including I441-L822, M442-L825, and I445-L825, are far away from each other in the monomer but are brought close together in space in the hSLO1 gating ring (Figure 21b).

A comparison of the gating rings from MthK and hSLO1 reveals a striking difference between the two proteins: whereas in MthK Ca^{2+} binds at the "flexible interface" within a RCK pair in the same subunit, in SLO1 the Ca^{2+} bowl is located at the "assembly interface" between two adjacent subunits (Figures 21a and 21c). This result emphasizes the profound functional differences between RCK-containing homologs, which I will discuss in detail in the final discussion chapter.

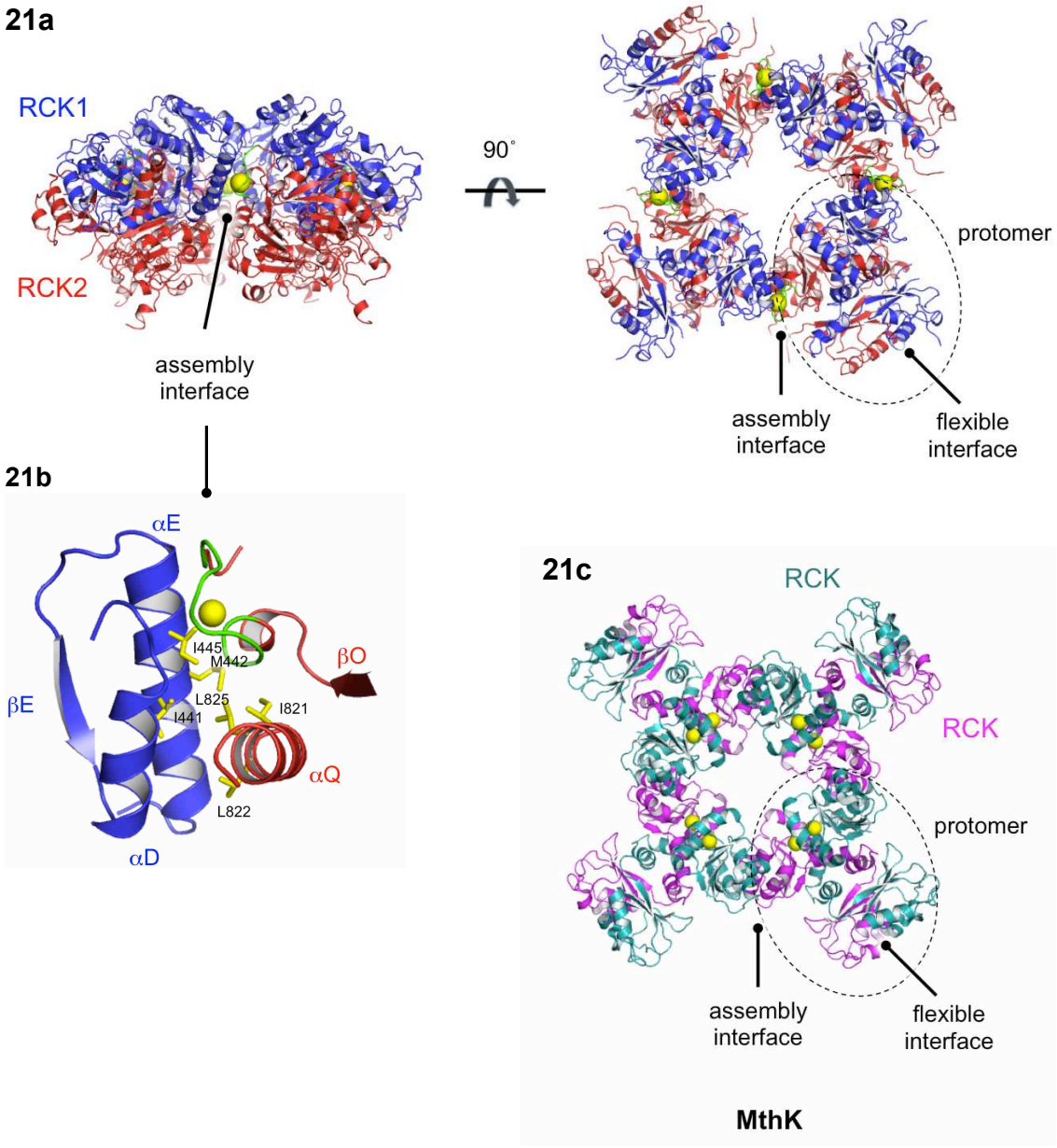

Figure 21: Gating ring assembly of hSLO1. 21a) Orthogonal views of the tetrameric hSLO1 gating ring structure using 6.0 Å diffraction data from the homologous chicken SLO2.2 CTD. View on the right is down the fourfold symmetry axis, with RCK1 in blue and RCK2 in red. The Ca^{2+} ions are shown as yellow spheres. The flexible and assembly interfaces are labeled. **21b)** Close-up view of the assembly interface. **21c)** Open gating ring structure from the MthK channel (PDB accession, 1LNQ), viewed down the fourfold axis.

3.1.5) Structure of the Ca^{2+}-free hSLO1 gating ring from the Jiang lab

Shortly after we published the structure of the monomeric Ca^{2+}-bound hSLO1 CTD, the laboratory of Youxing Jiang solved the X-ray structure of the hSLO1 CTD in a gating ring form, in Ca^{2+}-free conditions (197). To constrain tetramerization of the CTDs in the crystal, Jiang and co-workers fused the CTD N-terminus to a leucine-zipper domain from the GCN4 transcription factor that is known to assemble in a tetrameric coil-coiled helix bundle (197) (Figure 22a). Using this method, they obtained the tetrameric structure of the hSLO1 CTD gating ring at 3.1 Å resolution. Surprisingly, the tetrameric coil-coiled domain was disordered in the crystals, and could not be seen in the structure.

The hSLO1 gating ring structure of Jiang and colleagues (Figure 22b) matches extremely well with the tetrameric assembly we proposed based on the gSLO2.2 low-resolution data (193, 197). In particular, the inter-subunit "assembly interface", whose atomic details are now defined, is in excellent agreement with our model. The Ca^{2+} bowl sequence in this new hSLO1 gating ring structure sits at the same assembly interface.

The hSLO1 gating ring structure was solved in the absence of Ca^{2+}, thus representing the unliganded, most likely "closed" conformation of the SLO1 gating ring (197). This important structure therefore provides the first conformational snapshot of a eukaryotic SLO channel gating ring. Since this structure defines the Ca^{2+}-free, closed conformation of the SLO1 gating ring, the next important question to answer was how the binding of Ca^{2+} influences the structure of the SLO1 gating ring to promote channel opening. To address this, we focused our effort on finding conditions to obtain the crystal structure of a Ca^{2+}-bound SLO1 gating ring. Screening for SLO1 CTDs from many different species, we discovered that the CTD from the zebrafish SLO1 could be crystallized in the presence of Ca^{2+}, assembling in a gating ring.

22a

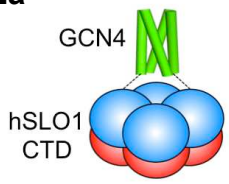

Figure 22: hSLO1 Ca^{2+}-free, closed gating ring structure. 22a) Schematic representation of the strategy used by Jiang and colleagues to stabilize the tetrameric assembly of the hSLO1 CTD: the CTD is fused to a helix from the GCN4 protein forming a very stable tetrameric coil-coil bundle. **22b)** Orthogonal views of the Ca^{2+}-free, closed hSLO1 gating ring structure.

22b

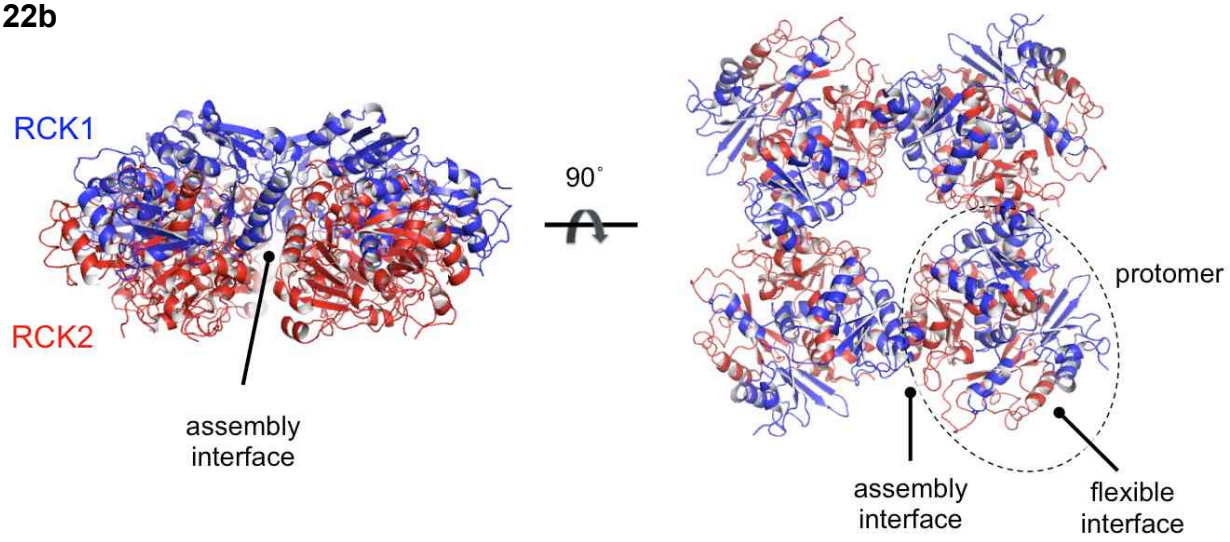

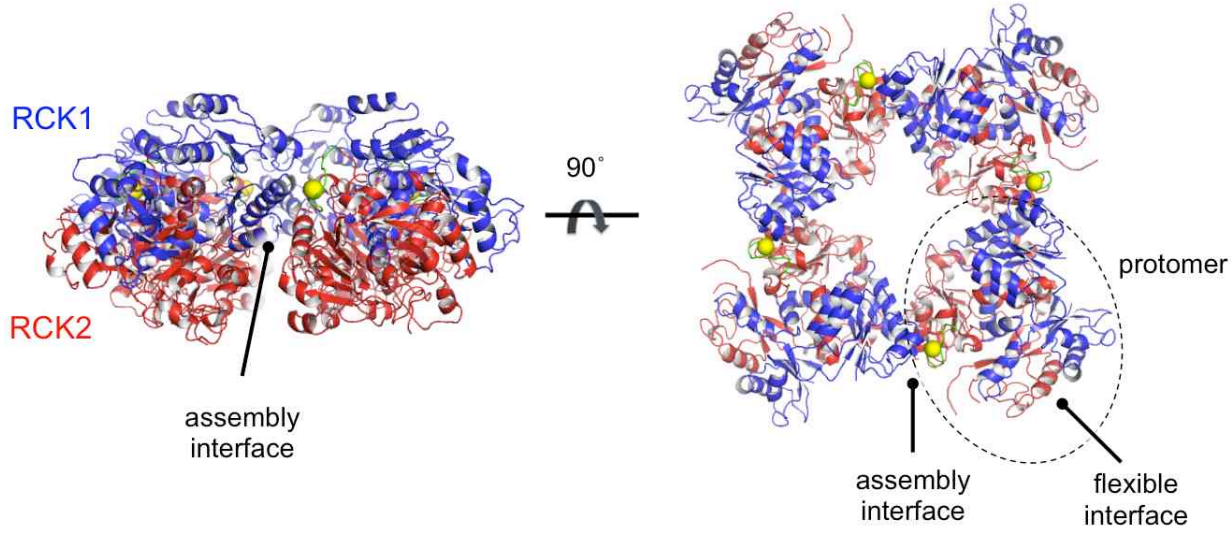

Figure 23: zSLO1 Ca^{2+}-bound, open gating ring structure. Orthogonal views of the Ca^{2+}-bound, open zSLO1 gating ring structure, using the same scale and orientation as in Figure 22b, The Ca^{2+} bowl is shown in green and Ca^{2+} ions as yellow spheres.

3.2 – STRUCTURE OF THE Ca^{2+}-BOUND, OPEN SLO1 GATING RING

3.2.1) Crystallization and structure determination

We used a CTD construct from the zebrafish SLO1 (zSLO1) channel containing two truncations (194): a truncation removing the disordered C-terminus (as in hSLO1) and a deletion of a large loop in RCK2 that was surface-exposed and disordered in our previous hSLO1 structure (193). We verified that these two deletions had no effect on the function of the full channel (194). The protein crystallized in the $P2_12_12_1$ space group, with eight CTD copies in the asymmetric unit. The crystals diffracted X-rays to 3.6 Å resolution. Initial phases were determined by molecular replacement using our previous hSLO1 CTD structure as a search model, and refinement using 8-fold crystallographic symmetry restraints led to a final model with $R_{work}/R_{free} = 0.26/0.29$ (Table 2).

3.2.2) Open structure of the SLO1 gating ring

An important aspect of the zSLO1 gating ring structure is the fact that the human and zebrafish SLO1 channels are extremely close in both amino acid sequence and functional properties. The two channels are 93% identical in terms of sequence, and their sensitivities to Ca^{2+} are essentially indistinguishable (data not shown). As a consequence, the ligand-bound, "open" zSLO1 gating ring structure can be directly compared to the Ca^{2+}-free, "closed" hSLO1 gating ring structure to assess potential conformational changes underlying Ca^{2+}-mediated gating.

The overall organization of the open zSLO1 gating ring is similar to the closed gating ring structure: the RCK1 domains from each subunit form a layer of the gating ring closest to the membrane, whereas a layer of RCK2 domains

assembles below (Figure 23). Electron density attributable to a Ca^{2+} ion is present in the Ca^{2+} bowl region, at the "assembly interface" between subunits, confirming the location of this Ca^{2+} binding site we originally inferred. The Ca^{2+} bowl structure itself is nearly identical to that of the monomeric Ca^{2+}-bound hSLO1 CTD (data not shown).

3.2.2) RCK1 N-lobe movement in the closed-to-open transition

What are the main structural differences between the Ca^{2+}-free, closed and the Ca^{2+}-bound, open SLO1 gating rings (shown in Figure 24a)? An objective comparison of conformational differences between the two structures is achieved by superimposing all Cα atoms of the tetrameric gating rings. Such a superposition reveals that most of the gating ring undergoes very little conformational change, especially the bottom RCK2 layer. In particular, only modest conformational differences occur at the intersubunit "assembly interface", except locally near the Ca^{2+} bowl (Figure 24b). However, the architecture of one region of the protein changes significantly between the closed and open structures: the top of the RCK1 layer facing the membrane, corresponding to the very N-terminal part of the CTD (from secondary structure elements βA to βC) in the RCK1 N-lobe. This conformational change is shown in more detail in Figure 24c, where the moving N-terminal region of the gating ring is highlighted in blue (the rest of the protein is colored in grey, and the front subunit is removed for clarity): in the Ca^{2+}-bound, open structure, the N-lobe region of the RCK1 layer moves upward. Importantly, the moving RCK1 N-lobe region contains the N-terminal CTD residue (Lys 343 in both hSLO1 and zSLO1, Cα shown as magenta sphere), which is connected to the transmembrane pore in the channel. It is interesting to note that the Ca^{2+} ion bound in the Ca^{2+} bowl is not directly at the interface between the moving βA-βC RCK1 N-lobe region and

the rest of the protein (Figure 24d). The overall conformational changes between the closed an open gating rings are best appreciated by looking at an interpolative movie where both structures are morphed (movie available at: http://tinyurl.com/7zx3bwb, part 1): the RCK1 N-lobes appear to "open up" on the membrane-facing surface of the gating ring in a way akin to petals opening on a flower. The upward movement of the RCK1 N-lobe between the closed and open conformations results in a significant increase in the diameter of the SLO1 gating ring (at the position of the N-terminal residues). This is shown in Figure 24e: the bulk of the protein (where conformational changes are only modest) is colored in grey, the N-terminal region of the RCK1 N-lobes is colored in blue and the Cα of Lys 343 is shown in magenta. The gating ring diameter, measured at the Lys 343 Cα, increases from 81 Å in the closed SLO1 to 93 Å in the open SLO1. Such dilation of the gating ring is reminiscent of what is seen between the closed and open conformations of the bacterial Ca^{2+}-activated MthK (see Chapter 1).

Again, the remodeling occurring at the inter-subunit interface upon Ca^{2+} binding is only modest. Instead, the major conformational change of the SLO1 gating ring during the closed-to-open transition is created principally by a structural rearrangement within individual subunits. The structures of single subunits from the Ca^{2+}-free hSLO1 and Ca^{2+}-bound zSLO1 are compared in Figure 25. In Figure 25b, the RCK2 domain is chosen as a point of reference to illustrate this intra-subunit rearrangement: the subunit structures are superposed by minimizing the distances between Cα atoms in the RCK2 domain (see Figure 25c where Cα distances are plotted onto the open subunit structure). We can see that the major conformational change involves the RCK1 N-terminus (βA to βC in the RCK1 N-lobe), which changes its angle and orientation with respect to rest of the structure.

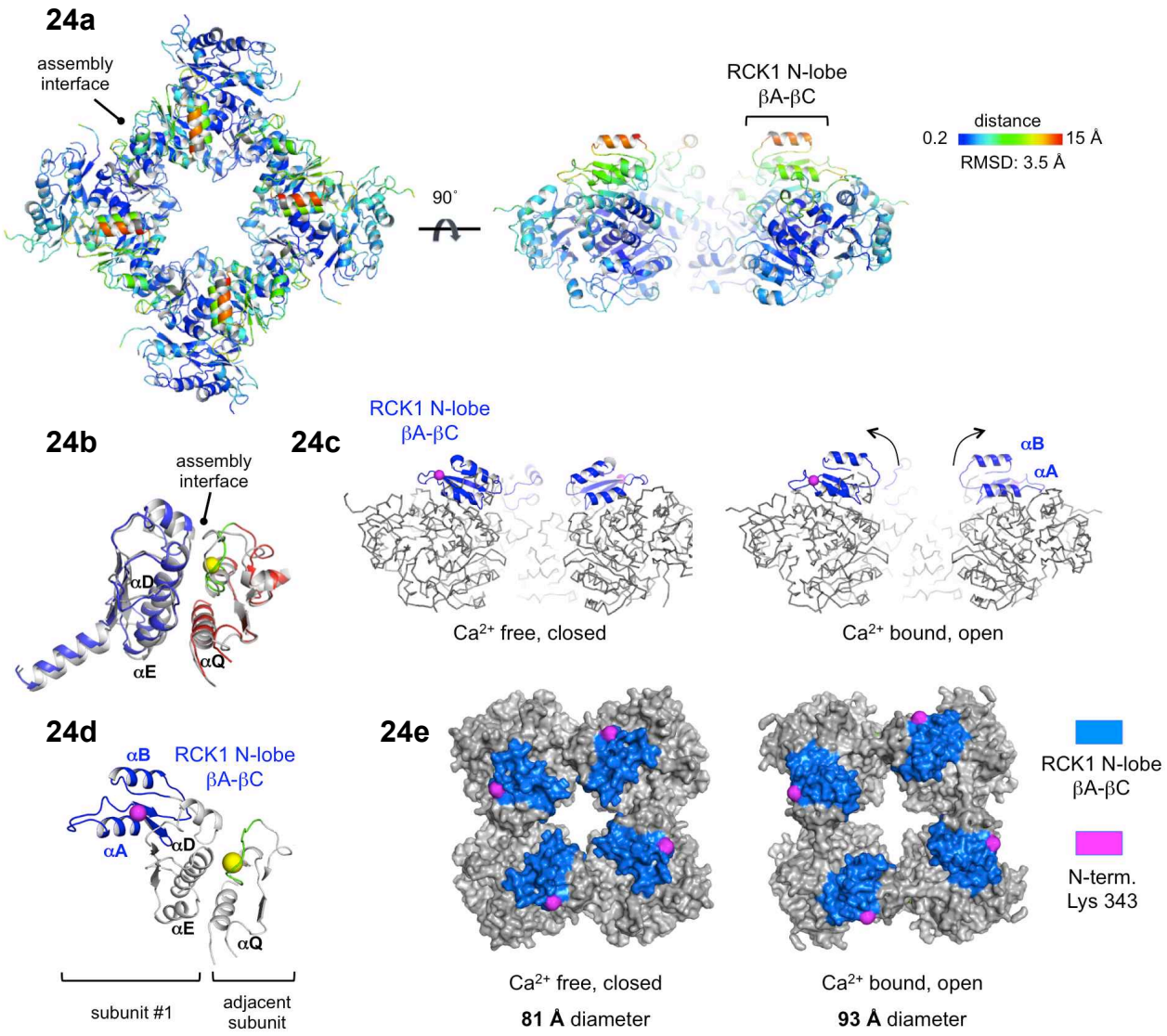

Figure 24: Conformational changes between the closed and open SLO1 gating rings structures. 24a) Structure of the Ca^{2+}-bound, open gating ring illustrating the result of an all-atom superposition with the Ca^{2+}-free, closed gating ring. The open gating ring structure is colored according to the distance between corresponding Cα positions in the two structures. In the side view (left), the front subunit is removed for clarity. **24b)** Superposition of the assembly interfaces from the closed (grey) and open (colored) gating ring structures. **24c)** Comparison of the closed and open structures using the same side view as in 24a. The structures are show in grey, except the βA-βC region of the RCK1 N-lobe, which is highlighted in blue (see text). The N-terminal Lys 343 is shown as magenta sphere. **24d)** Close-up view of the assembly interface and the βA-βC region of the RCK1 N-lobe. **24e)** Closed and open SLO1 gating rings structures viewed from the top, down the four-fold symmetry axis. The diagonal distance between the Cα atoms of diametrically opposed N-terminal residues (Lys 343) is indicated.

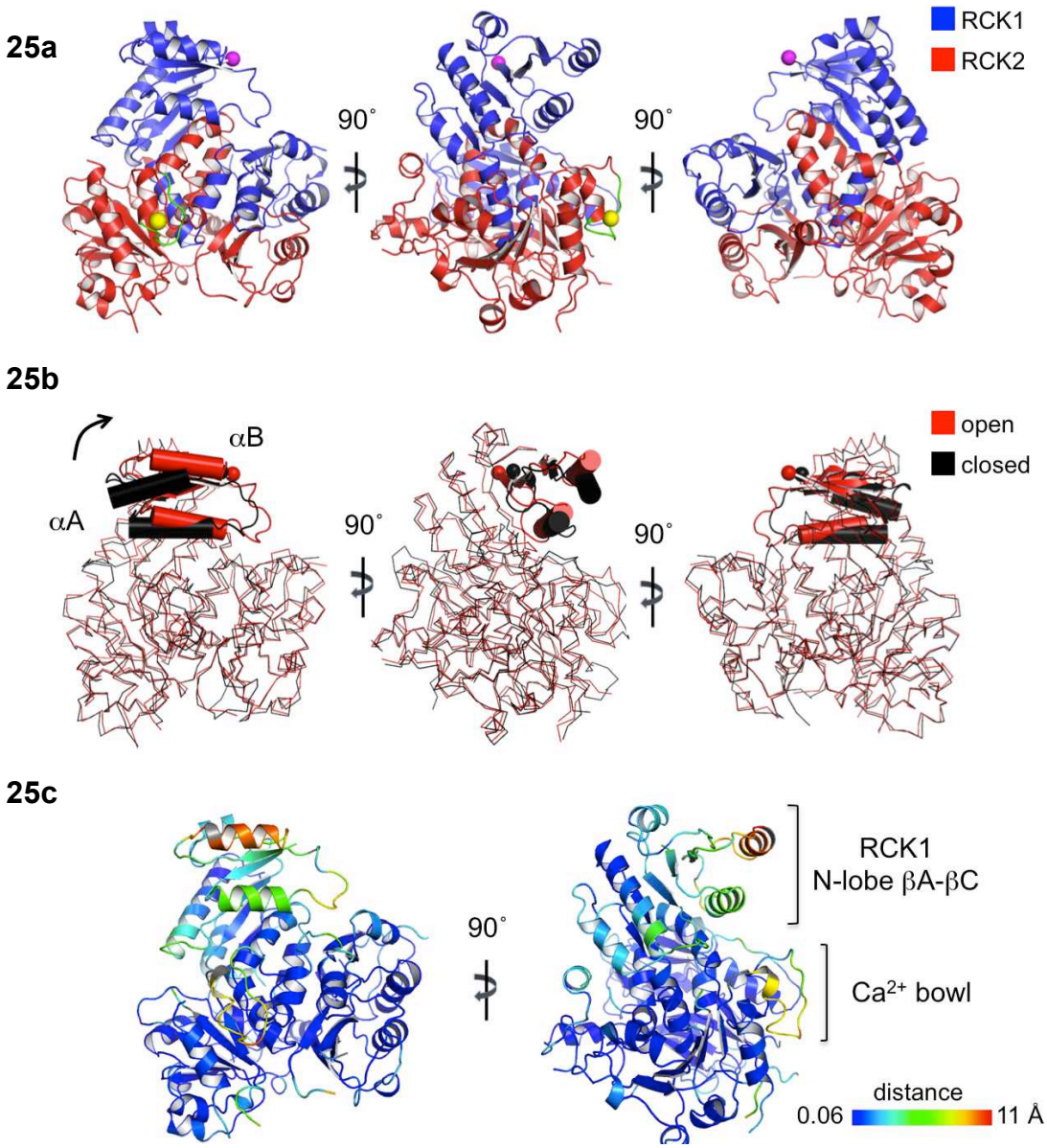

Figure 25: Conformational changes between subunits from the closed and open SLO1 structures. 25a) Structure of a subunit from the Ca^{2+} bound, open SLO1 gating ring. The N-terminal Lys 343 is shown as magenta sphere. **25b)** Same views as in 25a) showing a superposition of subunits from the open (in red) and closed (in black) SLO1 gating rings, aligning the RCK2 domains. Parts where the two structures align very well are shown in wire representation. The βA-βC region of the RK1 N-lobe, which orientation changes significantly between the two structures, is highlighted by showing a cartoon representation of secondary structure elements. The N-terminal Lys 343 is shown as a sphere. **25c)** Cartoon representation of the open SLO1 subunit colored according to the distance between Cα positions between the open and closed structures in the superposition shown in 25b).

3.3 – A STRUCTURAL MODEL FOR SLO1 Ca^{2+}-DRIVEN OPENING

Are the conformational changes we observe between the Ca^{2+}-free and Ca^{2+}-bound SLO1 gating ring structures compatible with the opening and closing of a K^+ channel? In other words, with these two conformations in hand, can we reconstruct the transition between a closed and an open SLO1 channel using our prior structural knowledge of K^+ channels?

To address this question, we constructed structural models of the closed and open conformations of a SLO1 channel using the SLO1 gating ring structures and the structures of closed (KcsA) and open (MthK) bacterial K^+ channel pores. The Ca^{2+}-bound structure of MthK served as the first reference for our model. We started with this open MthK structure and replaced its gating ring with the Ca^{2+}-bound zSLO1-channel gating ring. This step involved alignment of the four-fold axis followed by minimization of the distance between the N terminus of the SLO1 gating ring and the corresponding position within the MthK gating ring structure, through least-squares minimization of the distances between residues 343 of all four SLO1 subunits and the corresponding residues, 116, of all four MthK subunits. The resulting model of an open SLO1-channel gating ring with an open K^+ pore is shown in Figure 26a. The distance between the C-terminal residue of the inner helix of the pore and the N-terminal residue of RCK1, which was not constrained in making the model, is 33 Å. In a second step, we replaced the open MthK pore with the closed KcsA pore by aligning the invariant selectivity filter, and replaced the Ca^{2+}-bound zSLO1 gating ring with the Ca^{2+}-free hSLO1 gating ring by aligning the nearly invariant RCK2 layer. The resulting model of a Ca^{2+}-free SLO1 gating ring with a closed K^+ pore is shown in Figure 26b. In this closed model, the distance between the C-terminal residue of

the inner helix and the N-terminal residue of RCK1, which again was not constrained in making the model, is 32 Å. In this analysis, the similar pore-to-gating-ring distance (32 Å) in the open model and the closed model suggests that the magnitude of conformational change observed within the gating ring is compatible with the magnitude of change known to occur in the pores of other kinds of K^+ channels. This result reinforces the conclusion that the Ca^{2+}-free hSLO1 and Ca^{2+}-bound zSLO1 gating ring structures represent two conformations directly relevant to Ca^{2+}-driven gating in SLO1 channels. An interpolative movie illustrating our analysis is available at http://tinyurl.com/7zx3bwb (part 2).

Altogether, the SLO1 CTD structures we solved offer important new insights into the mechanism of Ca^{2+} gating in SLO1 channels. The first structure of the monomeric hSLO1 CTD describes the precise molecular organization of the SLO1 Ca^{2+}-activation apparatus, formed by a tandem of RCK domains. The structure also defines the precise position of the Ca^{2+} bowl, on the side of RCK2, which has an unexpected structural consequence: in SLO1 channels, this main Ca^{2+} binding site is located at the assembly interface between subunits, in sharp contrast with the position of the ligand binding site in bacterial RCK-containing channels. By solving the structure of the Ca^{2+}-bound zSLO1 gating ring, and comparing it with the structure of the Ca^{2+}-free hSLO1 gating ring from the Jiang lab, we now have the first molecular snapshots of the conformational changes involved in SLO1 Ca^{2+}-driven opening. During the closed-to-open transition, a major conformational change occurs in the RCK1 N-lobes facing the membrane, leading to a dilation of the gating ring that we can directly link to the opening of the transmembrane K^+-conducting pore.

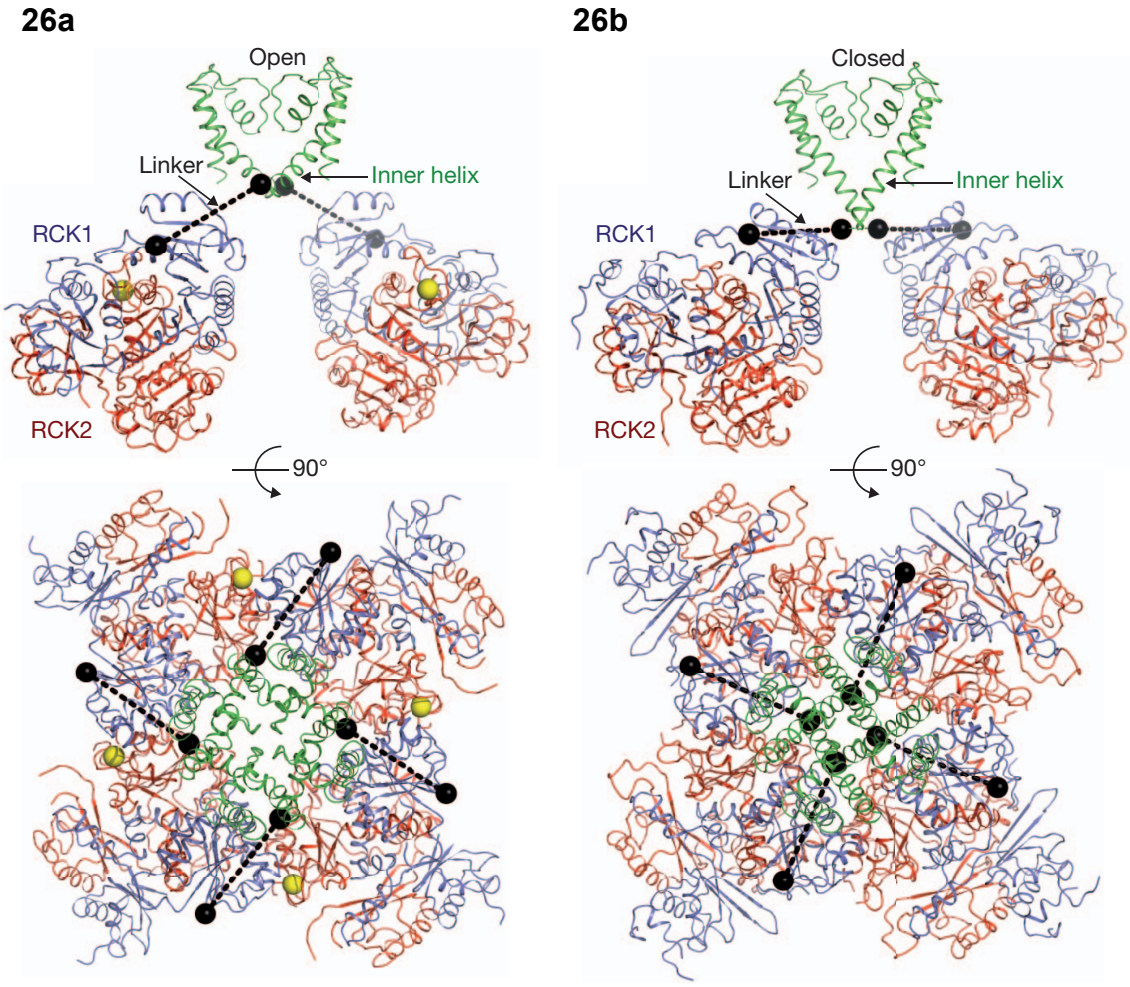

Figure 26: A Ca^{2+}-gating model for the SLO1 channel. 26a) Views of the SLO1 channel model with an open gating ring and an open pore. The structure of the Ca^{2+}-bound SLO1 gating ring is docked onto the open MthK channel (PDB accession 1LNQ) by aligning the gating rings. Yellow spheres represent Ca^{2+} ions. The N-terminal residues of RCK1 and the C-terminal residues of the inner helices are shown as black spheres. **26b)** Views of the BK channel model with a Ca^{2+}-free gating ring and a closed pore. Here, the Ca^{2+}-bound gating ring in 26a) is replaced by the Ca^{2+}-free gating ring (PDB accession 3NAF) and the open MthK pore in 26a) is replaced by the closed KcsA pore (PDB accession 1K4C). The inner helix from KcsA is truncated to match the length in MthK.

This work paves the way for a precise molecular understanding of Ca^{2+} activation in SLO1 channels. In particular, we can now directly address how the energy of Ca^{2+} binding is transduced into the conformational changes we observe (and ultimately into mechanical work to open the channel pore) by designing specific experiments based on our structural knowledge. At another level, our data and analysis now define the precise conformation of two end points in the Ca^{2+}-induced gating conformational transition of the SLO1 gating ring. Given the large conformational change that occurs upon Ca^{2+} binding, it should in principle be now possible to identify small molecules that stabilize one conformation or the other, with direct therapeutic implications considering the vast range of disorders linked to SLO1 function.

CHAPTER FOUR:

CRYSTAL STRUCTURE OF THE HUMAN SLO3 CTD:

IMPLICATIONS FOR PH SENSING IN SLO3 CHANNELS

Our work on SLO1 channels defined the conformational changes occurring at the intracellular level during Ca^{2+}-activation: the upward movement of the RCK1 N-lobe region upon Ca^{2+} binding triggers opening of the transmembrane ion-conduction pore. What, then, about other channels in the SLO family? Are the mechanistic principles of intracellular activation conserved? To address this question, I turned to the pH-sensitive, alkalization-activated SLO3 channels, which are the closest homologs of SLO1 (see Chapter 1). I focused on the human and mouse SLO3 channels, aiming at understanding the molecular mechanisms of pH sensing in these proteins. To this end, I solved a structure of the human SLO3 gating ring. Interestingly, a comparison with the SLO1 gating ring structures reveals that the organization of the N-lobe region of the RCK1 domains in the tetrameric hSLO3 gating ring matches closely the open conformation of the SLO1 gating ring.

To further understand the mechanistic principles of pH gating in SLO3 channels, I performed functional mutagenesis with the goal of identifying protein residues responsible for pH sensing. Whereas the direct functional analysis of the human SLO3 channel proved prohibitively challenging because of low protein expression, I could identify the residues responsible for pH sensing in the mouse SLO3 homolog. These residues are located at the interface between the RCK1 N-lobe and RCK2. This lead me to propose a model for pH sensing in the mouse SLO3 channel in which the direct effect of pH increase is to drive the movement of the RCK1 N-lobes to open the channel. Surprisingly, the protein residues forming the pH sensor in mouse SLO3 are not conserved in SLO3 channels from other species. SLO3 channels, which are specific to mammalian sperm cells, offer a striking example of the extremely fast evolution of proteins specialized in reproduction.

4.1 – STRUCTURE OF THE HUMAN SLO3 GATING RING

4.1.1) The human SLO3 channel is activated by an increase in intracellular pH

As I presented in Chapter 1, SLO3 channels are specific to mammalian sperm cells, where variations in intracellular pH directly regulate many physiological processes (32). So far, only the function of the mouse homolog of SLO3 has been studied in detail. Electrophysiological studies have shown that, in mouse sperm cells, SLO3 currents are activated by an increase in intracellular pH (1-3). Furthermore, the pH-dependence of mSLO3 currents has been characterized in depth using heterologous expression (95, 198). I became interested in the human SLO3 (hSLO3) homolog because of its direct relevance to human physiology, but hSLO3 channels had never been studied functionally. I therefore decided to first characterize the pH dependence of hSLO3 currents, using heterologous expression.

I expressed SLO3 channels in *Xenopus laevis* oocytes, a standard expression system for electrophysiological studies (199). *Xenopus* oocytes are extremely large single cells (>1 mm diameter) in which RNA coding for an ion channel (or other protein of interest) can be directly injected. The oocyte cellular machinery then induces expression of the channel, and the corresponding currents can be studied by electrophysiological techniques. To study intracellular activation of SLO3 channels I used the inside-out patch-clamp technique, where a patch of the oocyte membrane is isolated within a glass pipette in a configuration exposing its intracellular surface. The intracellular solution applied to such an "inside-out" patch can thus be controlled, while the corresponding electrical currents are recorded.

The results of such recordings are presented in Figure 27a, which shows currents of a single inside-out patch from an hSLO3-expressing oocyte. The currents are elicited by a series of voltage steps from -140 to + 180 mV. Clearly, the hSLO3 currents are pH-sensitive: as the intracellular pH is increased, the current density increases as well. For comparison, the same experiment performed on the mouse mSLO3 homolog is shown in Figure 27b. Plotting the maximum SLO3 current (i.e., at +180 mV) as a function of H^+ concentration reveals that the pH dependences of hSLO3 and mSLO3 channels are extremely similar (Figure 27c). However, comparing the total amount of current between hSLO3 and mSLO3 reveals an important difference between these two channels: in *Xenopus* oocytes, hSLO3 channels are poorly expressed compared to mSLO3 (compare the current scale between Figures 27a and 27b). This property makes the functional analysis of hSLO3 technically challenging. Using other expression systems (HEK cells or *Sf9* cells) for electrophysiology did not overcome this problem (data not shown). In HEK cells, tagging hSLO3 with GFP shows an accumulation of GFP signal in the peri-nuclear region, suggesting that the hSLO3 protein is difficultly expressed at the plasma membrane (data not shown).

These functional studies on human SLO3 channels expressed in *Xenopus* oocytes establish for the first time that hSLO3 currents are alkalization-activated, with a pH-dependence very similar to the well-studied mSLO3 homolog.

4.1.2) Crystallization of the hSLO3 CTD and structure determination

Based on these results, I became interested in understanding the molecular mechanisms of pH sensing in mouse and human SLO3 channels. To this end, I decided to study the structure of cytoplasmic domains (CTDs) from these channels, expressed in *Sf9* cells as described in Chapter 3. Only the hSLO3 CTD could be expressed at levels compatible with structural analysis

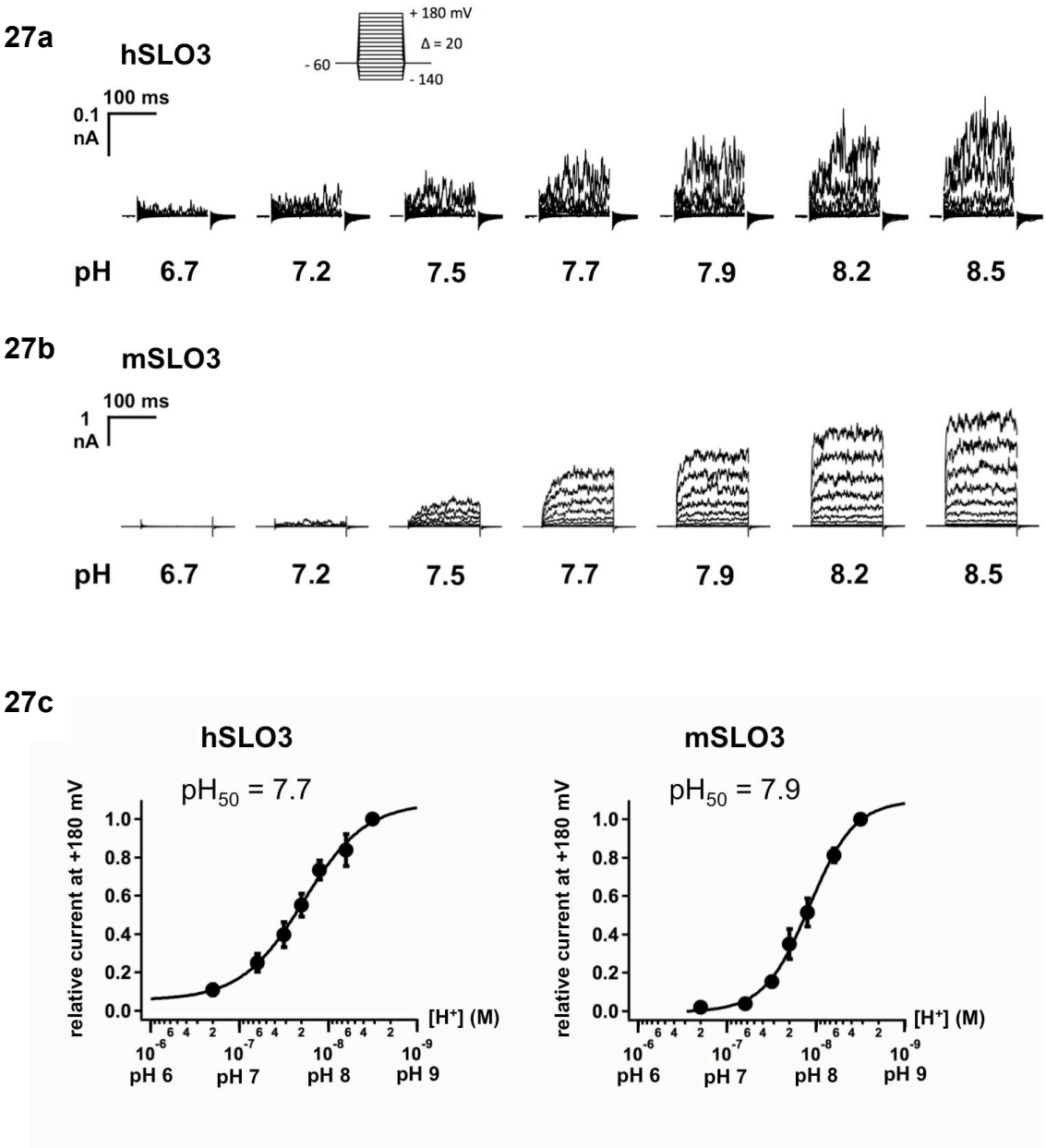

Figure 27: pH activation of human and mouse SLO3 channels. 27a) Representative inside-out patch currents recorded from a *Xenopus* oocyte expressing human hSLO3 channels. Channel opening was elicited by voltage pulses from -140 to +180 mV in 20 mV increments (see inset, holding voltage: -60 mV). The hSLO3 patch was sequentially bathed in solutions of increasing pH. The capacitive currents are masked for clarity. **27b)** Recordings as in 27a), showing currents from a mouse mSLO3 patch. 27c). **27c)** Plot of maximal current at +180 mV as a function of intracellular $[H^+]$, normalized to current at pH 8.5. Error bars show the standard error of the mean (hSLO3, n=3; mSLO3, n=5). pH dependence is fitted to a Hill curve.

(interestingly, the relative expression levels of the CTDs from hSLO3 and mSLO3 is opposite the expression levels of the whole channels).

Preliminary biochemical analysis showed that the hSLO3 CTD is most stable at high pH, and assembles as a tetramer during purification (data not shown). Crystals were obtained using poly-ethylene-glycols (PEGs) as precipitants, and PEG chain length was critical to optimize diffraction. The best crystals were grown using PEG12000 and diffracted X-rays to ~3.3 Å resolution. The hSLO3 CTD crystallized in the I222 space group, containing two CTD subunits in the asymmetric unit.

Diffraction of X-rays by these crystals was very anisotropic, and analysis revealed that diffraction in the a* and b* directions of the reciprocal cell are the weakest. The final dataset I used for structure determination makes use of data recorded from two different crystals, which varied in their degree of anisotropy. Reflection data were merged and scaled together in the final dataset. The scaled dataset was anisotropically corrected to resolution limits of 3.8, 3.4 and 3.3 Å along the reciprocal cell directions a*, b*, and c*, respectively, using the diffraction anisotropy server at UCLA (200). The final model was refined against data to 3.4 Å resolution.

The structure was solved by molecular replacement using the monomeric hSLO1 CTD structure as a search model. Importantly, the first step of structure refinement required rigid-body adjustment of the RCK1 N-lobe. The final model was refined to R_{work}/R_{free} = 0.25/0.27 (Table 3). Application of the crystallographic symmetry operators revealed that the hSLO3 CTDs assemble in a gating ring in the crystals.

4.1.3) Structure of the hSLO3 gating ring

The structure of the hSLO3 gating ring is shown in Figure 28a. The overall domain organization is similar to the SLO1 gating structures: in the hSLO3 gating ring, RCK1 domains form an upper layer facing the membrane (with the RCK1 N-lobe regions at the top) and RCK2 domains form a layer at the bottom. The secondary structure elements forming the "assembly interface" between subunits are conserved between hSLO3 and SLO1: helices αD and αE in the RCK1 domain of one subunit contact the helix αQ in the RCK2 domain of an adjacent subunit (see Figure 28b). A notable difference between SLO1 and hSLO3 occurs in the RCK2 region corresponding to the Ca^{2+} bowl in SLO1: the equivalent residues in hSLO3 form an extended alpha helix (named αQ'), which becomes part of the inter-subunit assembly interface (Figure 28b). The structure of an isolated subunit from the SLO3 gating ring is shown in Figure 28c. The overall domain organization of the hSLO3 CTD subunit is the same as for the SLO1 CTD subunit, showing a tandem of RCK domains brought together by a large interface, which principally consists of the helix-turn-helix motifs from the RCK1 and RCK2 domains.

4.1.3) Comparison with the SLO1 gating ring structures

The sequence of the human SLO3 channel shares a high degree of homology with the sequence of SLO1 channels. In particular, the sequence of the human SLO3 CTD is 42% identical to the sequence of the CTD from either human or zebrafish SLO1 channels. How, then, does the structure of the hSLO3 gating ring compare with either the closed or open structure of the SLO1 gating ring?

Before we examine the structures of the hSLO3 and closed or open SLO1 gating rings, let us first compare the structures of isolated subunits from each of

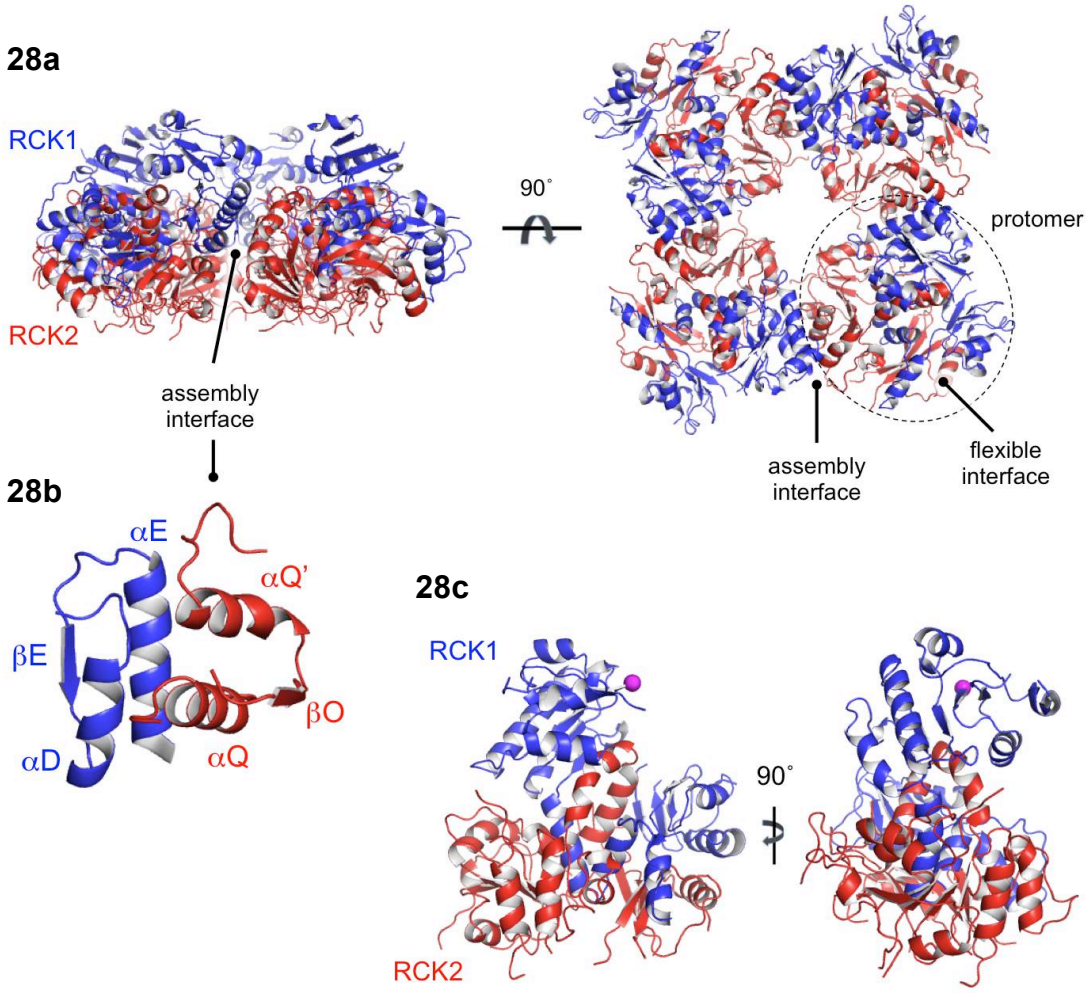

Figure 28: Structure of the human SLO3 gating ring. 28a) Cartoon representation of the hSLO3 gating ring structure with RCK1 colored in blue and RCK2 in red. The gating is viewed from the side (left) and form the top, down the four-fold symmetry axis (right). The inter-subunit assembly interface and intra-subunit RCK1-RCK2 flexible interface are labeled. **28b)** Close-up view of the hSLO3 assembly interface, with secondary structure elements labeled. In SLO3 an extended helix, αQ', is present in the region equivalent to the Ca^{2+} bowl in SLO1. 28c) Cartoon representation of a single subunit from the hSLO3 gating ring. The RCK1 domain is colored in blue, RCK2 is colored in red and the N-terminal residue (Lys 331, equivalent to Lys 343 in SLO1) is shown as a magenta sphere.

these tetrameric rings. The overall sub-domain organization of the hSLO3 CTD subunit is the same as in SLO1: both RCK domains are formed by a N-terminal lobe with a Rossman fold topology, followed by a helix-turn-helix motif and a C-terminal lobe (Figure 29a). However, the relative orientation of the sub-domains in the hSLO3 subunit is quite different than in the closed or open SLO1 structures. A comprehensive comparison reveals that, in the hSLO3 isolated subunit, the RCK1 N-lobe sub-domain changes its orientation with respect to the rest of the structure compared to either the closed or open conformation of the SLO1 subunit. This is shown in Figure 29b, where the SLO1 isolated subunits are aligned onto an hSLO3 subunit by superimposing the Cα atoms of all residues except the RCK1 N-lobe. The regions excluding the RCK1 N-lobe align very well. However, the orientation of the hSLO3 RCK1 N-lobe matches neither conformation of the SLO1 subunit.

If we now compare the structures of the entire gating rings between hSLO3 and the two conformations of SLO1, the direct result of the re-orientation of the RCK1 N-lobes in the individual hSLO3 subunits is that the hSLO3 ring does not align well with either the open or closed SLO1 rings. An objective comparison of these structures is achieved by superimposing all Cα atoms of the tetrameric gating rings. The total Cα RMSDs (calculated using all Cα from a tetrameric ring) of these superpositions are very high (4.7 Å for the hSLO3/open SLO1 superposition; 5.9 Å for the hSLO3/closed SLO1 superposition). However, an interesting difference can be noticed in the region formed by the RCK1 N-lobes from all four subunits (which I will from now on refer to as the "RCK1 N-lobe layer"). In the superposition using all Cα atoms, the RMSD in the RCK1 N-lobe layer (RMSD calculated using Cα belonging to the RCK1 N-lobes from all four subunits) between the hSLO3 and open SLO1 gating rings is 3.9 Å, versus 6.0 Å when hSLO3 is compared to the closed SLO1 conformation. This is shown

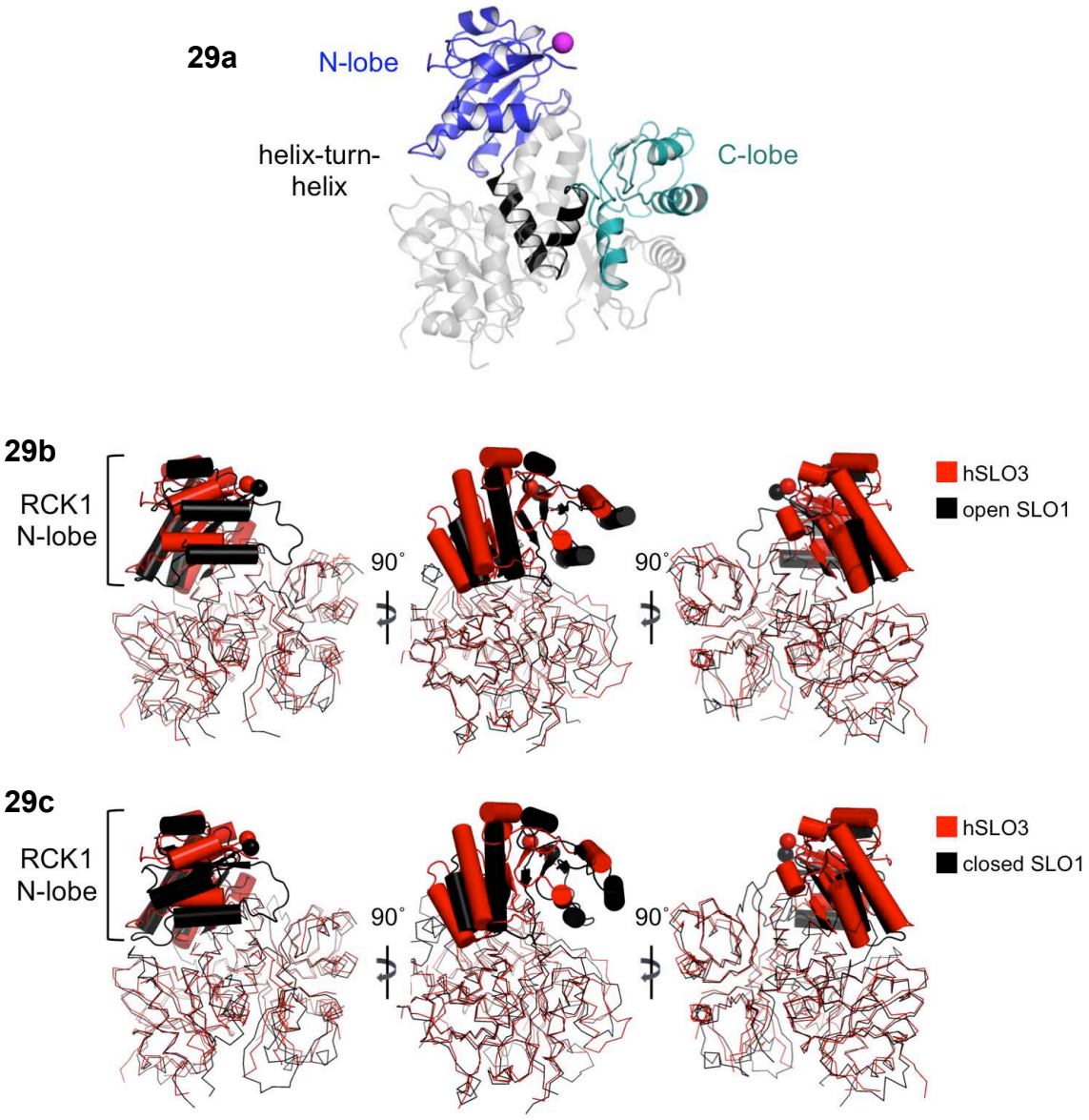

Figure 29: Comparison between the structure of individual subunits from the hSLO3 and SLO1 gating rings. 29a) Sub-domain architecture of the hSLO3 subunit, shown for RCK1. The sub-domain organization of RCK2 is identical. Magenta sphere shows the position of the N-terminal residue. **29b)** Superposition of subunits from hSLO3 (red) and the open conformation of the SLO1 gating ring (black). The subunits were superimposed using the Cα of all atoms excluding the RCK1 N-lobe region. **29c)** Same as 29b) but using the closed conformation of the SLO1 gating ring.

in Figure 30. In Figure 30, the all-Cα superimposed structures are viewed looking from the top of the gating ring, down the four-fold symmetry axis, and the RCK1 N-lobe layers are shown in ribbon representation (SLO3 colored red, SLO1 colored black). For the rest of the gating ring, where the structures do not align well, only the SLO3 structure is shown, in grey. Qualitatively, the objective all-Cα superpositions show that the overall structure of the hSLO3 gating is significantly different from either conformation of the SLO1 gating ring, but that the layer formed by the RCK1 N-lobes from all four hSLO3 subunits seems to align relatively well with the equivalent region of the open, but not the closed, conformation of SLO1. Another important aspect, independent of any superposition, can be seen in Figure 30a. Measured from equivalent N-terminal residues (K332 in hSLO3, K343 in SLO1, shown as spheres), the diameter of the hSLO3 gating ring (94 Å) matches almost exactly the diameter of the open SLO1 gating ring (93 Å, versus 81 Å in the closed SLO1 gating ring).

To further compare the structure of the RCK1 N-lobe layer between the tetrameric hSLO3 and SLO1 gating rings, I performed another structural alignment by superimposing the Cα atoms in this region (using all four subunits). The results are shown in Figure 31. This analysis reveals that, in the hSLO3 tetrameric gating ring, the structure of the RCK1 N-lobe layer matches very closely the corresponding region in the open conformation of the SLO1 gating ring (RMSD, measured using atoms from all four subunits: 2.7 Å), whereas the rest of the structures align quite poorly (RMSD, measured using atoms from all four subunits: 6.5 Å) (Figures 31a, 31c). When the closed conformation of the SLO1 gating is used in the same superposition, no significant alignment is observed in any part of the structures (Figures 31b, 31c).

The hSLO3 structure was solved by molecular replacement using the structure of the monomeric Ca^{2+}-bound hSLO1 CTD (PDB ID 3MT5) as search

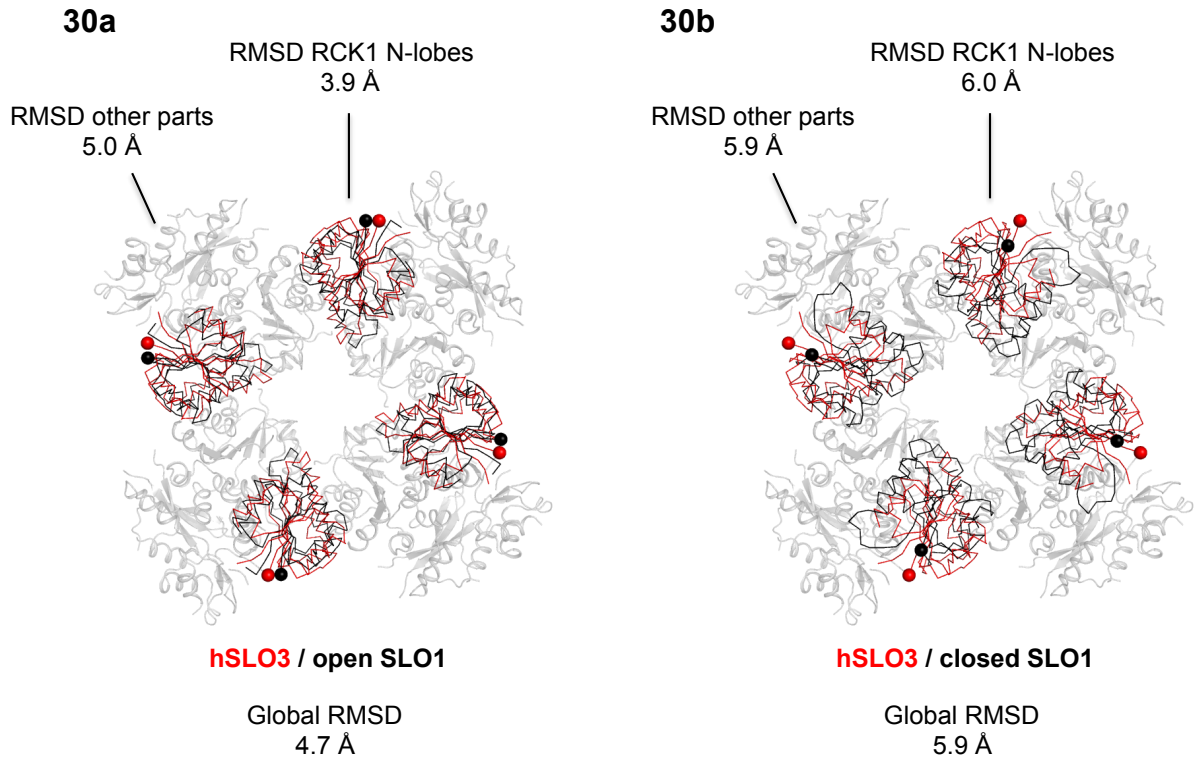

Figure 30: All-Cα atoms superposition of the hSLO3 and open/closed SLO1 gating rings. 30a) Objective superposition of the hSLO3 and open SLO1 gating rings by aligning all Cα from the tetrameric structures. The gating rings are viewed from the top, down the four-fold symmetry axis. The RCK1 N-lobe regions from the hSLO3 (in red) or the open SLO1 (in black) gating rings are shown as ribbon. The rest of the protein, for which the superposition is poor and is not shown, is drawn as a grey cartoon corresponding to the hSLO3 gating ring structure. The N-termini are shown as spheres. **30b)** Same as 30a), but using the closed SLO1 structure.

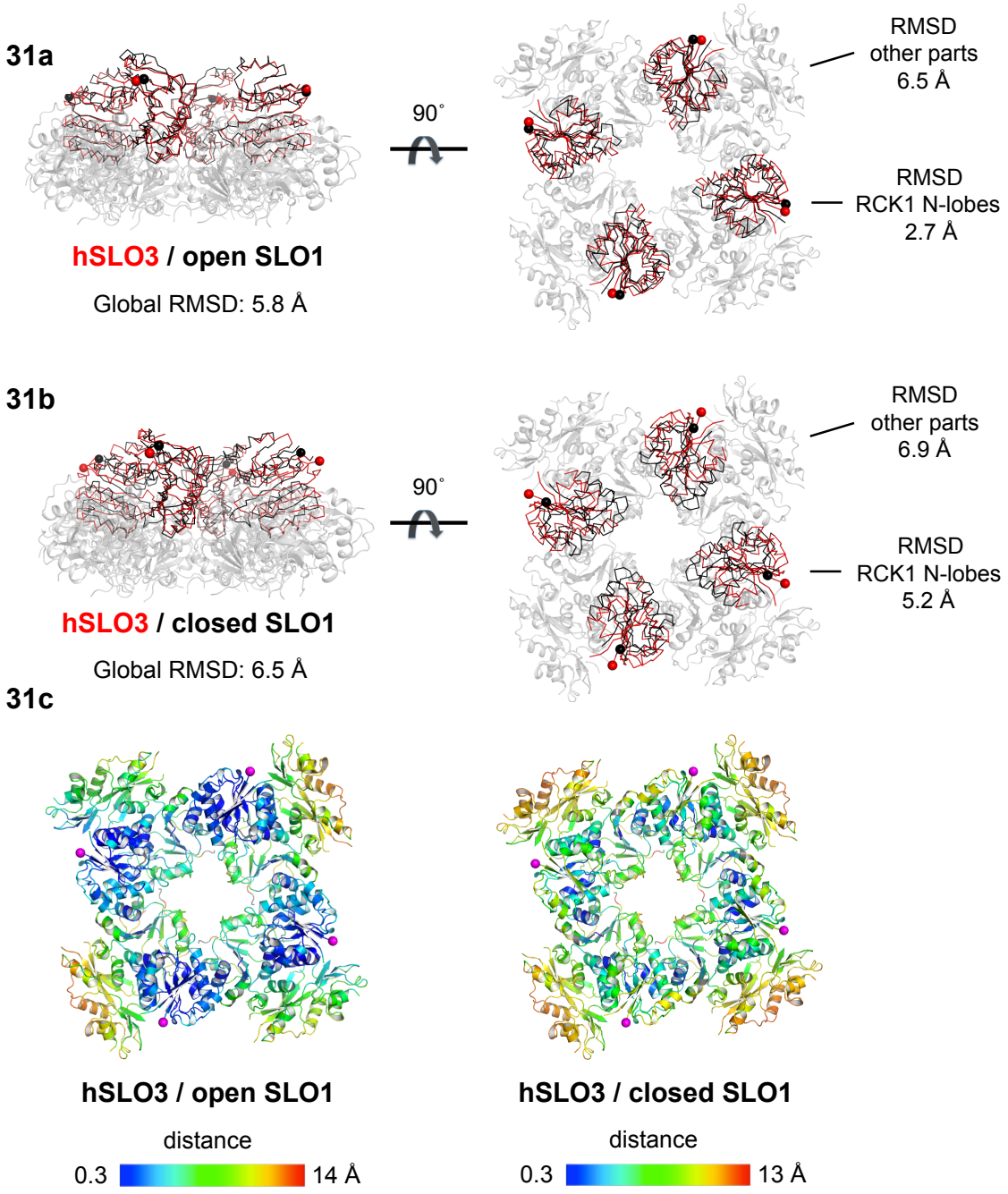

Figure 31: RCK1 N-lobes superposition of the hSLO3 and open/closed SLO1 gating rings. 31a) Superposition of the hSLO3 and open SLO1 gating ring structures by aligning the RCK1 N-lobes from all four subunits. The RCK1 N-lobe regions from the hSLO3 (in red) or the open SLO1 (in black) gating rings are shown as ribbon. The rest of the protein, for which the superposition is poor and is not shown, is drawn as a grey cartoon. The N-termini are shown as spheres. **31b)** Same as 31a), but using the closed SLO1 structure. **31c)** Cartoon representation of the hSLO3 gating ring colored according to the distance between Cα positions in the same superpositions as in 31a) or 31b). Same view as in 31a) or 31b), right. The gating ring N-terminus is shown as a magenta sphere.

model. The conformation of this Ca^{2+}-bound hSLO1 monomer is very similar to the conformation of an isolated subunit from the open SLO1 gating ring. Since the hSLO3 structure was solved at relatively low resolution (3.4 Å), I wanted to ensure that the conformation of the SLO1 search model had no effect on the final hSLO3 structure, and especially on the architecture of the RCK1 N-lobe. To test this, I used an unbiased molecular replacement strategy in which the SLO1 subunit used as search model is separated into two independent parts: the RCK1 N-lobe on the one hand, and the rest of the subunit on the other. In a first round of molecular replacement, only the part excluding the RCK1 N-lobe is used as search model (searching for two copies, because the asymmetric unit in the hSLO3 crystals contains two protomers). This gives a first solution, where the position of the non-RCK1 N-lobe atoms are defined. In a second round of molecular replacement, this first solution is fixed and only the isolated RCK1 N-lobe is used as searched model (again, searching for two copies). This gives a final solution representing the whole hSLO3 subunit. The hSLO3 gating ring structure can then be generated by applying the crystallographic symmetry operators. The result of this unbiased molecular replacement strategy shows that the final hSLO3 gating ring structure is independent of whether the closed or open conformation of a SLO1 subunit is used as search model. In each case, the final architecture of the hSLO3 gating ring (in particular in the RCK1 N-lobe layer) matches the refined structure that I described in this chapter (data not shown).

Altogether, the hSLO3 gating ring structure resembles most closely the open conformation of the SLO1 gating ring. Most importantly, the architecture of the RCK1 N-lobe layer in hSLO3 coincides with the architecture observed in the open SLO1 gating ring, and the overall diameters of the hSLO3 and open SLO1 gating rings are identical. Since in SLO1 channels the orientation of the RCK1 N-

lobe layer is the main structural determinant of the open vs. closed state of the gating ring, it is likely that the hSLO3 structure represents the open conformation of the hSLO3 gating ring[1]. The fact that hSLO3 and SLO1 channels are highly homologous in amino acid sequence reinforces this hypothesis. In particular, the length of the linkers connecting the CTDs to the transmembrane pore is absolutely conserved, so that the identical diameters of the hSLO3 and open SLO1 gating rings could drive the opening of the pore in a similar manner.

It is interesting to stress that, whereas the architecture of the RCK1 N-lobe layer is conserved between the hSLO3 structure and the open conformation of SLO1, in the rest of the gating ring the hSLO3 and open SLO1 structures do not align. In particular, the architecture of the "bottom layer" formed by the RCK2 domains (shown in grey in Figure 31a) is very different in these two gating rings. Again, this is a direct consequence of the different positioning of the RCK1 N-lobe within the individual subunits of these two structures. To "compensate" for this re-positioning, the specific orientation of subunits with respect to one another is changed between the hSLO3 and open SLO1 tetramers so as to keep the architecture of the RCK1 N-lobe layer, but not of the rest of the gating ring, unaltered. This raises the possibility that the specific architecture of the RCK1 N-lobe layer is constrained between SLO1 and SLO3 channels, which I will develop more in the final discussion chapter.

[1] The hSLO3 crystals were grown in a solution with an initial pH of ~6.8, at which hSLO3 channels are expected to be mostly closed. However, the actual pH in a protein crystal is hard to define and, maybe most importantly, the pH dependence of the isolated hSLO3 gating ring does not have to be the same as for the entire channel. The value of pH in which the crystals were grown might therefore be somewhat irrelevant to estimate whether the structure represents the open or closed conformation of the hSLO3 gating ring based on the pH dependence of hSLO3 currents.

In conclusion, the structure of the hSLO3 gating ring provides the first molecular snapshot of the pH-sensing unit from a SLO3 channel. However, a mechanistic understanding of how an increase in intracellular pH drives the opening of SLO3 channels is still lacking. To address this important question, I decided to perform functional mutagenesis on SLO3 channels with the goal of identifying the amino acid residue(s) responsible for pH sensing. Unfortunately, due to the very low expression of hSLO3 currents in heterologous systems, direct mutagenesis analysis of hSLO3 channels proved to be prohibitively challenging. As a consequence, I decided to perform mutagenesis in the mouse mSLO3 homolog, whose pH dependence is very similar to hSLO3. Furthermore, the two channels share a significant percentage of sequence identity (67 %).

4.2 – MECHANISM OF PH SENSING IN MOUSE SLO3 CHANNELS

4.2.1) pH sensing residues in mSLO3

To identify the pH sensing residues in mouse SLO3 channels, I modified single amino-acids by introducing point mutations in the mSLO3 sequence (usually to alanine), and analyzed the pH-dependence of the corresponding mutant channels by electrophysiology in *Xenopus* oocytes. I focused my analysis on amino-acids containing protonable side-chains (namely: Asp, Glu, His, Lys and Arg). I tested the effect of mutations in different regions of the mSLO3 CTD, insisting on protonable residues located at protein interfaces that could be important for channel function: the inter-subunit assembly interface (in particular, I mutated all protonable residues around a large region corresponding to the Ca^{2+} bowl in SLO1), the RCK1-RCK2 helix-turn-helix hinge, and the interface between the RCK1 N-lobe and the rest of the protein structure.

Out of > 40 positions tested (see Appendix B), mutations of only two residues had a significant effect on the pH dependence of mSLO3: His 417 located in the RCK1 N-lobe, and Asp 912 located in the RCK2 helix-turn-helix motif. The pH dependences of the mSLO3 D912N and H417A mutants are shown in Figure 32. All traces are normalized to the maximal current obtained at pH 8.5 ($[H^+]$ = 3.2 10^{-9} M). The pH dependence of mSLO3 D912N is dramatically impaired compared to wild-type, whereas the H417A mutation abolishes all pH sensitivity in the range studied here (pH 7.2 to 8.5, $[H^+]$ 6.3 10^{-8} M to 3.2 10^{-9} M).

A more detailed analysis of the functional effects of the D912N and H417A mutations in mSLO3 is still under way. However, a qualitative observation suggests that the mutant D912N or H417A mSLO3 channels are constitutively more open than wild-type mSLO3. This can be observed in experiments in which

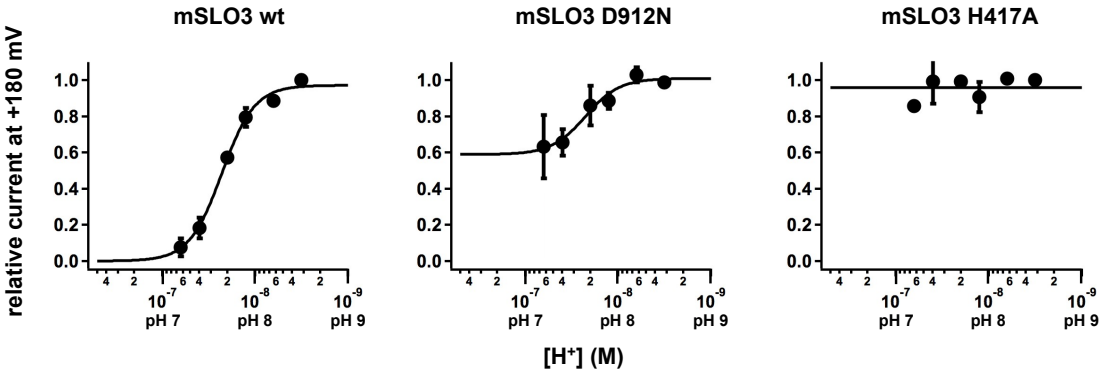

Figure 32: D912N and H417A mutants in mSLO3 channels. pH dependences of wild-type, and mutant D912N and H417 channels are shown as in Figure 27. Each point is the mean of two independent measurements.

the resting membrane potential of intact *Xenopus* oocytes expressing the different channels is measured. In ND-96 buffer approximating physiological conditions (96 mM extracellular [Na^+], 2 mM extracellular [K^+]), the presence of constitutively open K^+ channels in the oocyte membrane would drive the resting potential to more negative values (the reversal potential for K^+ in this system is around -100 mV). This is precisely what is observed with the D912N and H417 mutants. Whereas oocytes expressing wild-type mSLO3 channels have a typical resting potential of -40 mV, oocytes expressing either the D912N or H417A mutants have typical a resting potential of -70 mV. Importantly, this is not due to an increase in expression of the mutant channels compared to wild-type (data not shown). Rather, the D912N and H417A mutant channels appear to be significantly more open than wild-type mSLO3 under resting conditions.

4.2.2) H417 and D912 in the mSLO3 CTD, and conservation in other SLO3 channels

The functional effects of the D912N and H417A mutations in mSLO3 raise the possibility that these residues form the "pH sensor" of mSLO3 channels, in other words that the protonation state of either or both D912 and H417 side chains is the molecular determinant for pH sensing in mSLO3. Can we evaluate this hypothesis by looking at where these residues are located within the mSLO3 CTD? And are these residues conserved in other SLO3 channels, such that the pH sensor they might be the same in other species?

D912 is conserved in all SLO3 channels, but also in SLO1 channels. However, H417 is surprisingly not conserved in the SLO3 family: in all other species for which the SLO3 sequence is known, the residue at position 417 is a non-protonable proline (Figure 33a). Does this mean that H417 is unlikely to be part of the pH sensor in mouse SLO3 channels? As I will describe next, I believe

that H417 is indeed the pH sensing residue in the mouse SLO3 protein (i.e. the residue which protonation state directly changes upon pH increase, leading to channel opening). Rather, the non-conservation of H417 is most likely the consequence of two processes: on the one hand, the inherent structural and functional plasticity of the gating ring scaffold, and on the other hand, the extremely rapid evolution of proteins specialized in reproduction (such as the sperm-specific SLO3), which is well described and believed to be an important driving force for speciation, limiting cross-species fertilization (201, 202). I will discuss this idea further in the final discussion chapter.

Since H417 is not conserved in the human SLO3 channel (where it is a proline), it is difficult to directly use the hSLO3 structure to understand the functional effects of the H417A mutation in mSLO3. The structure of the SLO1 CTD, on the other hand, offers important insights. In SLO1, the residue corresponding to mSLO3 H417 is a lysine (K428 in hSLO1), conserved across SLO1 species. K428 is located in the loop between secondary structure elements βD and αD in the RCK1 N-lobe. Interestingly, in the SLO1 CTD structure (in the closed as well as open state), K428 is involved in a salt bridge interaction with the conserved aspartate corresponding to mSLO3 D912 (D921 in hSLO1). The K428-D921 salt-bridge makes a direct structural connection between the bottom of the RCK1 N-lobe and the RCK2 domain in SLO1 channels. The position of these residues is shown in Figure 33b, where I used the structure of the Ca^{2+}-free hSLO1 CTD structure and replaced K428 with a histidine. In hSLO3, the presence of a proline at position 417 changes dramatically the structure of the βD-αD loop, which kinks away from RCK2 (Figure 33c). The specific architecture of this loop in hSLO3 is most likely due to the unique structural properties of proline residues. It is possible that, in mSLO3, the presence of a histidine induces a loop conformation resembling what is seen in SLO1.

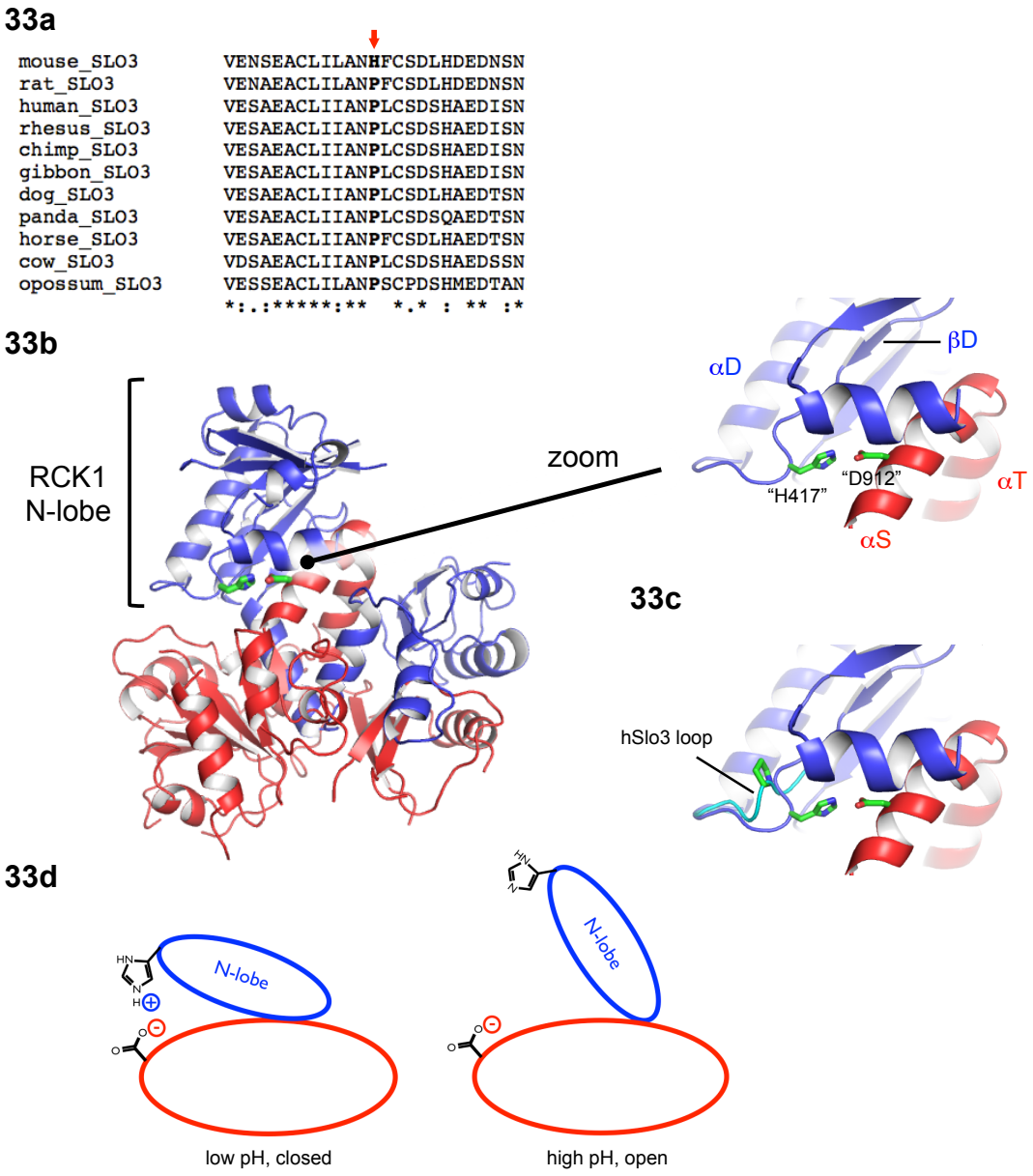

Figure 33: A model for pH gating in mSLO3 channels. 33a) Sequence comparison of SLO3 channels at the position corresponding to H417 in mSLO3. In all other species, this residue is a proline. **33b)** In SLO1 channels, the residues equivalent to mSLO3 H417 and D912 form a salt-bridge interaction. The structure from a single subunit of the Ca^{2+}-free hSLO1 gating ring is shown, with K428 (equivalent to mSLO3 H417) replaced by an histidine. The putative salt-bridge formed by H417 and D912 in mSLO3 connects the RCK1 N-lobe and the RCK2 domain in a single subunit. **33c)** Architecture of the βD-αD loop in the hSLO3 structure. **33d)** Mechanistic model for pH gating in mSLO3 channels. As the intracellular pH increases, H417 is deprotonated and the salt-bridge interaction with D912 is lost, leading to an upward movement of the RCK1 N-lobe domain.

4.2.3) A model for pH sensing in mouse SLO3 channels

The structural arrangement shown in Figure 33b offers a natural hypothesis for the mechanism of pH sensing in mouse SLO3 channels. A salt-bridge interaction between D912 an H417 would be ideally located to control the position of the RCK1 N-lobe with respect to the rest of the mSLO3 CTD. In SLO1, the major conformational change during the closed-to-open transition involves precisely the movement of the RCK1 N-lobes with respect to the rest of the gating ring. Furthermore, the similar arrangement of the RCK1 N-lobes between the hSLO3 and open SLO1 gating ring structure suggests that pH gating in SLO3 channels could involve a repositioning of the RCK1 N-lobes similar to what is observed in SLO1 channels. Therefore, I propose that the salt-bridge interaction between D912 and H417 in the CTD subunits form the pH-sensitive element of the mSLO3 gating ring. Which of these two residues could then be the actual pH sensor? H417 is perfectly suited to be the pH-sensing residue, since the histidine side-chain has the unique property of having a pKa falling right into the physiological range of pH in cells (203).

These observations lead me to propose a model for pH sensing in mSLO3 channels shown in Figure 33d. At low pH, H417 is protonated and makes a salt-bridge interaction with D912, stabilizing the "closed" conformation of the SLO3 gating ring. As pH is increased, H417 is deprotonated, the high-energy salt-bridge interaction is lost and the RCK1 N-lobe is free to change its angle with respect to the rest of the structure, leading to channel opening.

This model is based on three aspects revealed by the functional mutagenesis studies I presented. First, D912 and H417 are the only amino-acids whose mutation affected the pH-dependence of mSLO3 currents in a rather extensive mutagenesis screen. Second, the H417A mutation completely abolishes pH sensing in mSLO3 whereas D912N has a less dramatic effect, compatible with

the idea that the protonation state of H417 is the main determinant of mSLO3 pH dependence. Third, the H417A and D912N mutant channels appear to be constitutively more open than wild-type mSLO3. This is precisely what would happen in the context of the model, since in the absence of charges at positions 417 or 912, the salt-bridge interaction would be lost and the low-pH, "closed" state of the mSLO3 channel would be constitutively destabilized.

Additional experiments are needed to verify the model. In particular, a crucial prediction would be that mutations replacing H417 by an arginine or a lysine (H417R or H417K), which side-chains are expected to be constitutively protonated in the range of pH considered here due to their high pKa, would lock the corresponding mutant mSLO3 channels in a low-pH-like, "closed" conformation since the salt bridge would be constitutively present. Another test could involve functional experiments were positions 417 and 912 would cross-linked in a mutant mSLO3: upon cross-linking, the mutant channels should be "closed". These additional experiments are still ongoing.

4.2.4) An experimental system for functional mutagenesis of hSLO3 channels

If H417 is indeed the pH sensing residue in mSLO3, the fact that it is not conserved in the sequence of other SLO3 channels (in particular hSLO3) is quite surprising, especially considering that the pH dependences of mSLO3 and hSLO3 are very similar (recall Figure 27). To understand how mouse and human SLO3 channels could share almost identical pH sensitivities using different molecular mechanisms, we need to understand the molecular details of pH sensing in the human hSLO3 channel. As I described above, the low expression of hSLO3 in heterologous systems prevents mutagenesis experiments in practice. Such low functional expression could be explained by the fact that a specific cofactor or interaction partner, missing in heterologous systems, is required for

efficient protein folding and/or trafficking of hSLO3 channels. Very recently, a study identified a new protein interacting with mSLO3 channels in mouse sperm cells (106). This protein, LRRC52, belongs to the family of leucine-rich-repeat-containing membrane proteins, which also includes a protein known to interact with SLO1 (83). LRRC52 is present in the human genome, and I decided to test whether the human hLRRC52 interacts with hSLO3 channels in heterologous systems, and whether its presence would facilitate the expression of hSLO3 currents.

Co-expressing hLRRC52 with hSLO3 in *Xenopus* oocytes, I observed that this is indeed the case. hSLO3 currents recorded from oocytes expressing both hSLO3 and hLRRC52 are greatly increased compared to oocytes expressing hSLO3 alone (Figure 34a). The currents recorded from hSLO3 + hLRRC52 most likely originate from hSLO3 activity: these currents are blocked by the internal application of Ba^{2+}, a non-specific blocker of K^+ channels, and furthermore no currents can be observed when hLRRC52 is expressed on its own (data not shown).

Co-expression with hLRRC52 modifies the functional properties of hSLO3 channels. First, the kinetics of channel opening is slowed down (see the different time scales in Figure 34a). Second, the pH-dependence of hSLO3 + hLRRC52 currents is shifted to lower pH compared to hSLO3 expressed alone (Figure 34b). The fact that LRRC52-co-expression has an activating effect on SLO3 channel at a given pH has been described for the mouse mSLO3 homolog. Figure 34c shows the results of co-expression of mSLO3 channels with the mouse mLRRC52 protein: pH activation is shifted to lower pH, but this activation effect is less

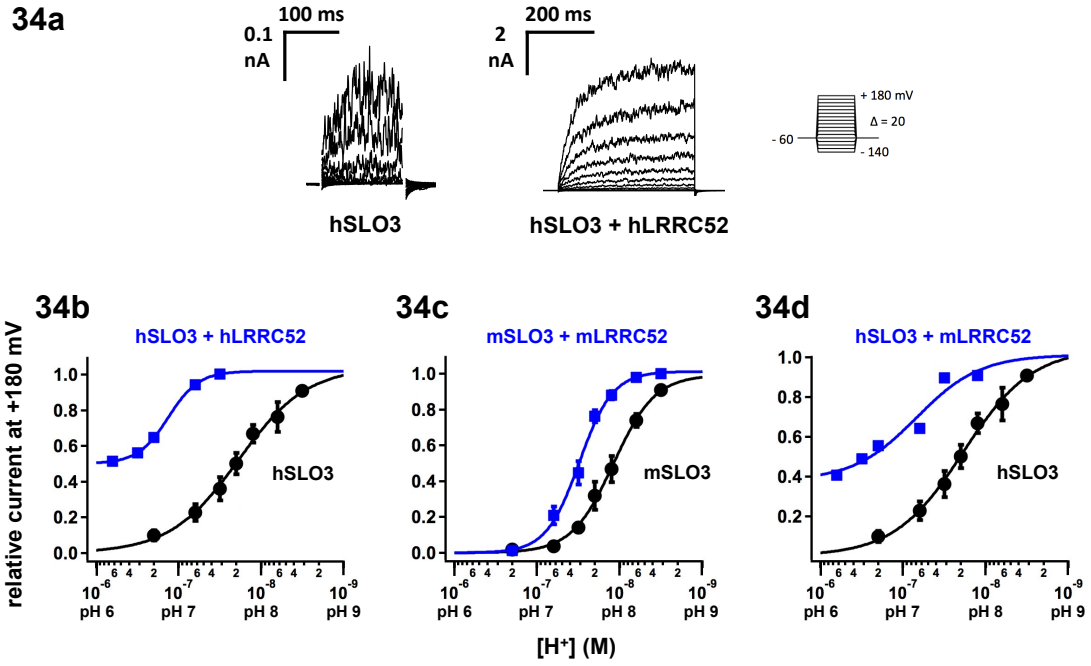

Figure 34: Co-expression of SLO3 channels with LRRC52. 34a) Representative inside-out patch currents recorded from *Xenopus* oocytes expressing either hSLO3 channels alone or hSLO3 channels and hLRRC52 proteins. **34b-d)** Effect of LRRC52 co-expression on the pH dependence of hSLO3 and mSLO3 channels. Each figure illustrates a specific combination of SLO3 and LRRC52 homologs: human SLO3 + human LRRC52 in 34b); mouse SLO3 + mouse LRRC52 in 34c); human SLO3 + mouse SLO3 LRRC52 in 34d). Errors bars, when shown, represent the standard errors from 3-5 independent measurements. For the hSLO3/hLRRC52 and hSLO3/mLRRC52 co-expression, the results shown are from a single experiment.

pronounced than for the human hSLO3 channels. The precise effects of the interaction between hSLO3 channels and LRRC52 require further analysis, which is still under way. Nonetheless, the pH-dependence observed with the co-expression of SLO3 and LRRC52 is likely to reflect the pH sensitivity of the SLO3 channel itself. For example, the human and mouse homologs of LRRC52 affect the pH-dependence of, respectively, hSLO3 and mSLO3 channels in a different manner (Figures 34b-d). However, co-expressing hSLO3 with the mouse LRRC52 resembles the co-expression of hSLO3 with human LRCC52 (Figure 34d), suggesting that the identity of the SLO3 channel, and not the LRRC52 protein, defines the pH-dependence of the SLO3/LRRC52 complex.

Overall, hLRRC52 co-expression facilitates expression of pH-sensitive hSLO3 channels. I believe I now have a robust system in hand in which I can analyze the molecular basis of hSLO3 pH-gating using functional mutagenesis. This paves the way for the direct comparison of the mechanism of pH sensing in human vs. mouse SLO3 channels. At another level, the results presented here describe for the first time that hLRRC52 might be an important physiological partner of hSLO3 channels. Testing whether this is indeed the case in human sperm cells would be very interesting.

In conclusion, my studies of the structure of the human SLO3 gating ring on the one hand, and of the mechanism of pH sensing of mouse SLO3 channels on the other hand establish a first step towards understanding the molecular basis of pH sensing in SLO3 channels. The fact that the mechanism of pH gating seem not be conserved between the human and mouse homologs make a definitive interpretation difficult, but I hope that mutagenesis studies on the human SLO3 channel itself (using co-expression with LRRC52 proteins) will allow us to decipher this difference.

Nonetheless, the structural and functional studies appear to agree on one point: both suggest that, in SLO3 channels, conformational changes restricted to the RCK1 N-lobe regions of the tetrameric gating ring might control pH-gating. The significance of this hypothesis will be discussed in more details in the final discussion chapter.

CHAPTER FIVE: DISCUSSION

INTRACELLULAR GATING OF SLO CHANNELS BY EUKARYOTIC GATING RINGS

In the preceding chapters I have presented my Ph.D. work, part of a very collaborative effort, that describes the crystal structures of the intracellular gating modules from three eukaryotic SLO K^+ channels: the monomeric structure of the Ca^{2+}-bound cytoplasmic domain (CTD) from the human SLO1 channel; the tetrameric structure of the Ca^{2+}-bound, open gating ring from the zebrafish SLO1 channel; and the tetrameric structure of the human SLO3 gating ring. These structures, together with the Ca^{2+}-free, closed SLO1 gating ring structure from the Jiang laboratory, provide the molecular foundations to understand how intracellular signals (Ca^{2+} binding in SLO1, Na^+ binding in SLO2 or pH increase in SLO3) control the opening of SLO channels. We now have in hand a precise framework in which to interpret the vast array of functional analysis that has been performed on these proteins over more than three decades. My own studies on the mechanism of pH sensing in the mouse SLO3 channel are an illustrative example in this respect.

In this final chapter, I will summarize my main results and examine them in three different contexts. First, I will compare the similarities and differences between the mechanisms of intracellular Ca^{2+} gating of the SLO1 and the bacterial MthK channel. This is an interesting example of how, through evolution, two proteins containing very similar domains can achieve the same function (i.e., activation by intracellular Ca^{2+}) using different strategies. This example also highlights the functional and structural plasticity of the gating ring scaffold. Second, I will come back to the comparison of hSLO3 gating ring with the open conformation of the SLO1 gating ring and show how this comparison could indicate convergent mechanistic principles in SLO1 and SLO3 channels. Finally, I will look at how our structural studies suggest an added level of complexity in the function of SLO channels in that the intracellular gating rings, in addition to regulating the ion-conduction pore directly, may also modulate the voltage sensor domains.

5.1) Ca^{2+} sensing in SLO1 and MthK channels

The crystal structures of the SLO1 CTDs reveal for the first time the precise molecular organization of the intracellular Ca^{2+}-sensing apparatus in SLO1 channels. The main conclusions of these studies are threefold. First, individual SLO1 CTD subunits are formed by two tandem RCK domains (RCK1 and RCK2), whose architecture is closely related to the RCK domains found in bacterial K^+ channels. Second, the CTDs from each subunit of a tetrameric SLO1 channel assemble in a gating ring structure at the intracellular surface of the membrane. In the tetrameric SLO1 gating ring, RCK1 domains from all four subunits form a layer at the top, while RCK2 domains form a layer at the bottom. The Ca^{2+} bowl in the SLO1 CTD is located on the side of the RCK2 domain and creates four Ca^{2+} binding sites on the outer perimeter of the tetrameric gating ring, at the interface between individual subunits. Third, Ca^{2+} binding in the SLO1 gating ring induces a major conformational change in the upper layer of RCK1 domains. This translates into an expansion of the gating ring diameter (measured from the CTD N-terminal residues) that we can directly relate to the opening of the transmembrane ion-conduction pore.

To date, the best-described example of an ion channel in which gating is mediated by intracellular ligand binding in RCK domains is the bacterial Ca^{2+}-activated K^+ channel MthK (122). As I presented in the introduction chapter, MthK and related RCK-containing prokaryotic channels are believed to be evolutionarily related to the eukaryotic SLO channels (24, 152), perhaps representative of an ancestral K^+ channel from which SLO1 evolved. In this context, it is interesting to compare the structures and mechanisms of Ca^{2+} activation between SLO1 and MthK.

At first glance, the structures of the intracellular gating modules of SLO1 and MthK are highly similar. The bi-lobed architecture of individual RCK

domains is strikingly conserved between the two channels: each RCK domain is formed by a N-terminal lobe with a Rossman fold topology, followed by a helix-turn-helix motif and a C-terminal lobe. In MthK, two separate identical RCK domains (created by an alternative Met start site) dimerize through a large "flexible interface" around their helix-turn-helix motifs in a similar manner than RCK1 and RCK2 domains assemble in the SLO1 CTD. Four MthK RCK dimers (equivalent to four CTD protomers in SLO1) assemble in a gating ring structure in which the inter-subunit "assembly interfaces" involve the same secondary structure elements as in the SLO1 gating ring (122). Finally, the open and closed structures of the MthK gating ring (122, 155) reveal that channel opening is triggered by an increase in diameter of the gating ring upon Ca^{2+} binding, like in SLO1.

However, despite these structural resemblances, the actual mechanisms of Ca^{2+} sensing in SLO1 and MthK channels are strikingly different. First of all, the ligand binding site in SLO1 sits in a rather unexpected location based on the expected properties of RCK domains. The α/β Rossman fold seen in RCK domains is a very common structural motif found in enzymes or ligand binding proteins, in which the active site or ligand binding site is located at the C-terminal end of the central β sheet (24, 204-206). RCK domains found in prokaryotic channels or transporters are no exception to this rule, and examples include Ca^{2+} binding in MthK (122) or nucleotide binding in the Trk/Ktr transporter family (207, 208). Surprisingly, the Ca^{2+} binding site in the SLO1 RCK2 domain (the Ca^{2+} bowl) is not located at this preferred position but rather sits on the side of RCK2. As a consequence, in the tetrameric context of the SLO1 gating ring, Ca^{2+} binds at the "assembly interface" between subunits, in marked

contrast with MthK where the Ca^{2+} binding sites are located at the "flexible interface" within single RCK dimers (Figure 35).

Another important difference between the Ca^{2+}-binding CTDs from SLO1 and MthK lies in the symmetry (or lack thereof) of their structures. Again, the MthK CTD "protomer" is an obligate dimer of identical RCK domains because both RCK domains originate from the repeated translation of a single gene (122). As a result, the MthK gating ring structure possesses, in addition to the global four-fold symmetry axis of the channel, two additional two-fold symmetry axes in the plane of the gating ring (colored green in Figure 35): the top and bottom RCK layers in the MthK gating ring share the same architecture, and the whole intracellular structure can be "flipped" upside-down (around one of the two-fold axes) without consequence. On the other hand, the two RCK domains of a SLO1 subunit are separately encoded within the same gene (perhaps originally through a gene duplication process), which allowed the RCK1 and RCK2 domains to evolve independently. The end result is that, in the SLO1 gating ring, the top RCK1 layer is structurally different than the bottom RCK2 layer. This has a direct consequence on the ligand-induced conformational changes observed in the closed-to-open transition of the SLO1 and MthK gating rings. As I described in Chapter 3, the conformational changes in the SLO1 gating ring are mostly restricted to the upper RCK1 layer (Figure 24, see also the interpolative movie at http://tinyurl.com/7zx3bwb). In contrast, in the MthK gating ring, the conformational changes are the same in the top and bottom layers as imposed by the added symmetry, and Ca^{2+} binding causes an expansion of the ring's height in addition to the dilation effect (155). The conformational changes between the closed and open conformations of the MthK gating ring are best appreciated by looking at an interpolative movie where the two conformations are morphed (available at http://tinyurl.com/cwob2wp). Comparing the Ca^{2+}-induced

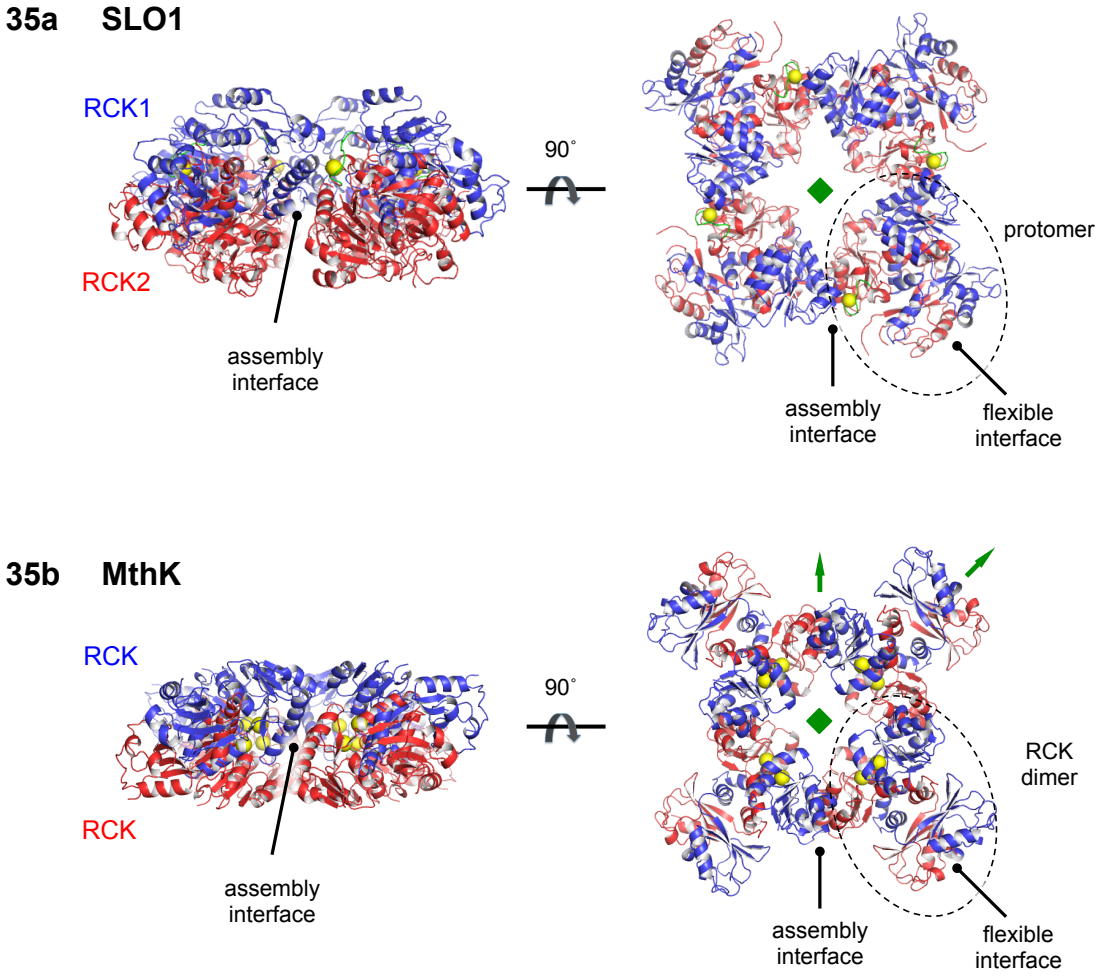

Figure 35: Comparison of the SLO1 and MthK gating ring structures. 35a) Cartoon representation of the Ca^{2+} bound SLO1 gating ring. RCK1 and RCK2 domains are colored blue and red, respectively. Ca^{2+} ions are shown as yellow spheres. **35b)** Cartoon representation of the Ca^{2+} bound MthK gating ring. RCK domains forming the top and bottom layers of the structure are colored blue and red, respectively. Ca^{2+} ions are shown as yellow spheres. In both 35a) and 35b), symmetry axes are shown in green in the right panels (square: four-fold axis perpendicular to the plane of the figure, arrows: two-fold axes in the plane of the figure).

conformational changes between the MthK and SLO1 gating ring structures highlights the profound mechanistic differences between these two related proteins. Overall, this comparison presents an interesting example of how the evolution of molecular structure within a class of proteins can give rise to different mechanistic strategies to perform a similar function (i.e., triggering the opening of the conduction pore of an ion channel upon Ca^{2+} binding).

At this point of the discussion, it is interesting to go back to the model I put forward for the mechanism of pH sensing in the mouse mSLO3 channel. In this model, which remains to be tested, the "pH sensor" in mSLO3 is located at the flexible interface, between the bottom of the RCK1-N lobe and the RCK2 helix-turn-helix motif within the same mSLO3 subunit. Hence in mouse SLO3 channels (which are believed to have evolved from a SLO1 ancestor as the result of a gene duplication event (209)), the pH sensor is located at a different interface than the Ca^{2+} sensor in SLO1. This example, together with the comparison of SLO1 and MthK, highlights the fact that gating ring scaffold capable of very high functional and structural plasticity. The numerous interfaces existing in these structures offer many opportunities for mechanistic remodeling, even between closely related channels. This inherent plasticity might manifest itself most dramatically in SLO3 channels. In the context of the rapid evolution of proteins specialized in reproduction, it is perhaps not so surprising to observe that mechanisms of pH sensing can be substantially remodeled between species because the gating ring scaffold allows just that. There are probably multiple ways to bias the conformation of a gating ring structure upon pH change, especially since pH will affect the protonation state of many side chains in the protein. Maybe during the rapid evolution of SLO3 channels, these different possible mechanisms were extensively sampled.

5.2) Comparing hSLO3 and SLO1 structures: functional implications

As I already presented in Chapter 4, comparing the structures of the gating ring from the human SLO3 channel with the open or closed structure of the SLO1 gating ring reveals interesting differences as well as, perhaps most importantly, similitudes between these structures. In the hSLO3 gating ring structure, the ring's diameter matches almost perfectly the diameter of the open SLO1 gating ring (94 Å vs. 93 Å, respectively, measured from the Cα position of the N-terminal residues of two opposite subunits; the diameter of the closed SLO1 gating ring is 81 Å). Moreover, the structure of the RCK1 N-lobes from all four subunits in the hSLO3 gating ring matches closely the structure of the same region in the open SLO1 gating ring, whereas the bottom RCK2 layers from the same two structures do not align. If the hSLO3 gating ring is compared with the closed conformation of the SLO1 gating ring, no significant similarity can be detected between the two tetrameric structures. This led me to propose that the human SLO3 gating ring structure represents the "open" conformation of the hSLO3 intracellular pH-gating module.

I believe that the significant conservation of molecular architecture in the RCK1 N-lobe layer between the gating rings of the hSLO3 and Ca^{2+}-bound SLO1 channels reveals an interesting structural constraint. In a simple description of SLO channel gating by intracellular signals, the gating ring can be viewed as a module that simply transduces chemical energy (e.g., binding of Ca^{2+}) into mechanical work used to pull open the channel's transmembrane helices. In this context, only the overall diameter of the gating ring (measured at the N-terminal positions connecting to the pore), but not the details of the gating ring structure, determines channel opening. Considering the significant conservation of amino-acid sequence between SLO1 and SLO3 channels (in particular, the spring-like transmembrane-to-CTD linkers have exactly the same length), it is perhaps not

surprising that the gating rings from both channels would reach equivalent diameters in the open state. But in the context of the high structural plasticity of the gating ring scaffold, and keeping in mind the rapid evolution of SLO3 channels, it is not hard to imagine that a completely different architecture could have evolved in SLO3 channels that would preserve the same overall diameter as in SLO1, but not the actual structure of the RCK1 layer of the gating ring. Then, if the hSLO3 structure really does represent the open conformation of the hSLO3 gating ring, what could explain the structural conservation we observe in the RCK1 N-lobe layer? I can mostly think of two (non-exclusive) possibilities. The first possibility would be that the RCK1 N-lobe layer, being the "active" region of the gating ring that rearranges during intracellular activation, is structurally constrained in the same way that the geometry of the active site (but not necessarily the rest of the structure) is conserved within a class of enzymes. Once an efficient molecular solution (in our case, a specific rearrangement of the RCK1 N-lobe layer) exists to perform a given function (in our case, opening the channel pore), the same solution is conserved during evolution. A correlate of this hypothesis would be that, in the closed state of the hSLO3 gating ring, the architecture of the RCK1 N-lobe layer would match the closed conformation of the SLO1 gating ring. The second explanation would be that, in SLO channels, the RCK1 N-lobe region interacts with other parts of the protein, and that this interaction constrains structurally the position of the RCK1 N-lobes. It is possible, as I will discuss in the next section of this chapter, that a significant molecular interface exists between the RCK1 N-lobe layer and the transmembrane domain of a SLO channel. In this case, the conserved architecture of the SLO1 and SLO3 transmembrane domains (expected based on sequence homology) would constrain the actual position of the RCK1 N-lobes between SLO1 and SLO3 channels in a similar manner.

5.3) A possible interface between eukaryotic gating rings and voltage-sensing domains

With the structures of the gating ring we now have in hand, it becomes possible to estimate what the structure of a full SLO channel might look like. I created models of a full SLO1 channel with an open or closed gating ring by using the same models used in Figure 26 (page 80) and replacing the ion conduction pores by the transmembrane domain of the paddle chimera voltage-dependent K_V channel (141) by aligning the invariant selectivity filters. The result is shown in Figure 36. In both the open and closed conformation, the SLO1 gating ring appears to fit well against the surface of the transmembrane K_V domain, with ridges from the gating ring fitting naturally into grooves that exist between the voltage sensors and the pore. Interestingly, the part of the SLO1 gating ring coming in close contact with the transmembrane domain in these models is precisely the βA-βC region of the RCK1 N-lobe, i.e. the part whose structure changes the most dramatically in the close-to-open transition of the SLO1 gating ring (Figure 36, recall also Figure 24 page 76). This raises the possibility that interactions with the transmembrane domain might functionally regulate the movement of the RCK1 βA-βC regions in the channel, and therefore influence intracellular gating. Importantly, previous experiments support the idea of a structural connection between the gating ring and the transmembrane domains of the SLO1 channel. In particular, functional studies have identified a putative Mg^{2+} binding site bridging two Glu residues located in the βA-βC region of the RCK1 N-lobe to amino acids on the voltage sensor (210, 211).

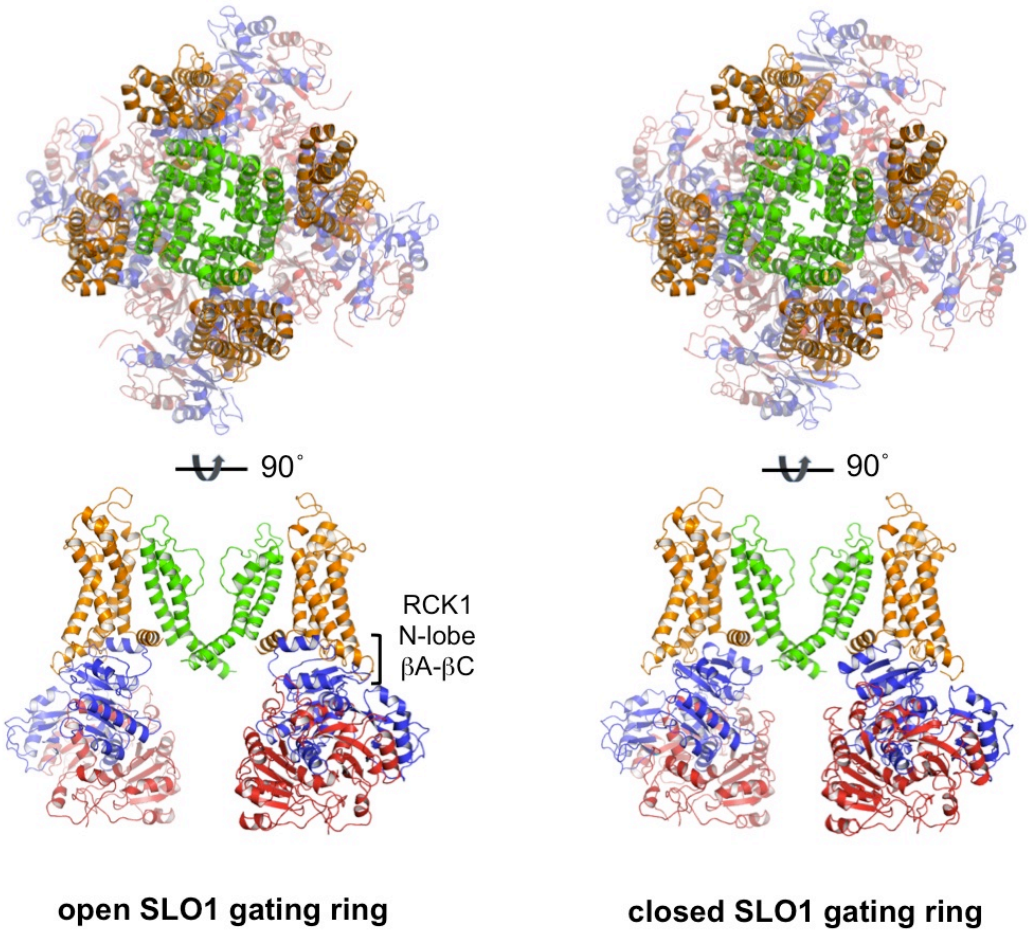

Figure 36: Models of the SLO1 channel. Cartoon representation of the molecular models of the SLO1 channel obtained by docking the transmembrane domain of the K_V chimera channel (PDB ID 2R9R) onto the models shown in Figure 26 (page 80). Models obtained using the open and closed conformation of the SLO1 gating ring are shown on the left and right panels, respectively. Voltage-sensor domains (VSD) are colored orange, pore domains are colored green and RCK1 and RCK2 domains are colored blue and red, respectively. In the side view (bottom panels), all domains at the front and the back are removed for clarity.

Overall, this very simple modeling exercise suggests that, in eukaryotic SLO channels, the interface between the gating ring and the voltage sensor domains could be larger than previously appreciated. A direct physical interaction between these two gating modules would allow the two synergistic signals required for channel activation (membrane voltage and intracellular cue) to modulate each other. Only the structure of an entire SLO channel would directly address this hypothesis. Considering the progress we made for the recombinant expression and purification of SLO channels in *Sf9* cells (presented in Chapter 2), I am confident that the long-awaited crystal structure of a SLO channel is forthcoming. I have no doubt that such structure would reveal an unprecedented level of complexity that would be fascinating to decipher in terms of functional mechanisms.

MATERIALS AND METHODS

1) SLO constructs expression and purification

Protein expression in *Pichia* yeast

Protein constructs (described below in the relevant sections) were sub-cloned in the PICZ-c vector (Invitrogen). *Pichia pastoris* cells (HIS+ strain of SMD1163, Invitrogen) were transformed by electroporation (BioRad Micropulser) using vector linearized with PmeI as described in the manufacturer's manual. Transformants were selected on YPDS plates (Invitrogen) containing 400-1200 µg/ml Zeocin (Invitrogen), and used to inoculate small-scale cultures in BMGY medium (Invitrogen) grown at 30°C overnight. For large-scale expression, 1-L cultures in BMGY medium were inoculated using the small-scale cultures and cells were grown at 30°C until OD_{600} reached ~20. Cells were then pelleted, resuspended in BMM medium (Invitrogen) and expressed overnight at 30°C. Cells were harvested by centrifugation, flash-frozen in liquid N_2 and stored at -80°C.

Protein expression in *Sf9* cells

Protein constructs were sub-cloned in the pFastBac vector (Invitrogen) and baculovirus was generated using the Bac-to-Bac system (Invitrogen) following the instructions manual. *Sf9* cells were cultured at 27°C in supplemented Grace's insect cell medium (Invitrogen) to a density of ~ 1.0 10^6/mL before infection with baculovirus. Infected cells were cultured for ~60 hours at 27°C, then harvested by centrifugation and washed in ice-cold PBS. Cell pellets were flash-frozen in liquid N_2 and stored at -80°C.

Protein expression in HEK cells

Protein constructs were sub-cloned in the pCGFP-EU vector (175). HEK cells were grown in 6-well plates in DMEM medium (Invitrogen) in a 37°C incubator. HEK cells reaching ~90% confluence were transfected using lipid-mediated transfection (Lipofetamine 2000, Invitrogen). Transfected cells were used 48h thereafter.

Protein constructs

The following genes where used as template for subcloning: human SLO1 HsloM3 (GI: 507922, a gift from L. Toro); *Aplysia californica* SLO1 (GI: 39545756, a gift from L. Kaczmarek); rat SLO2.2 (GI: 11177892, a gift from L. Kaczmarek); mouse SLO3 (GI: 86646081, a gift from L. Salkoff); human SLO3 (GI:157074213), chicken SLO2.2 (GI: 20338417) and zebrafish SLO1 (GI: 189526846) genes were identified in database searches and were synthetized by Bio Basics, Inc. For recombinant expression, constructs of interest were fused to a C-terminal GFP followed by a deca-histidine affinity tag (GFP-His_{10}) or a 1D4 tag (GFP-1D4, amino-acid sequence for 1D4: TETSQVAPA). A PreScission protease (GE Healthcare) cleavage site (LEVLFQG) was introduced before the C-terminal GFP. The PreScission recognition sequence and a cloning site (EcoRI) result in a stretch of amino acids SNSLEVLFQ attached to the C-terminus of all constructs. CTD constructs of human hSLO1, chicken gSLO2.2, zebrafish zSLO1 and human hSLO3 were expressed as GFP-His_{10} fusions in *Sf9* cells included the following amino acids: for hSLO1, residues 341-1056; for gSLO2.2, residues 347-1201, for zSLO1, residues 341–1060 with a loop deletion (839–872); for hSLO3, residues 330-1041 with a loop deletion (831-852).

Fluorescence size-exclusion chromatography

Small-scale cultures of *Pichia*, *Sf9* or HEK were lysed in a buffer containing (in mM): 150 KCl (unless stated otherwise), 50 TRIS pH 8.0; 1 EDTA; 40 DDM; 10 dithiothreitol (DTT) containing protease inhibitor cocktail IV (EMD Biosciences). Size-exclusion chromatography on a Superose-6 column (GE Healthcare) was carried out in buffer containing (in mM): 150 KCl, 20 TRIS pH 8.0; 1 EDTA; 1 DDM; 10 DTT. GFP fluorescence was monitored using a Shimadzu RF-10AXL detector.

Cell lysis

The following lysis methods were used: frozen *Pichia* cells were lysed in a Retsch, Inc. Model MM301 mixer mill (5 x 3.0 min. at 25 cps), keeping the grinding jars in liquid N_2 between milling cycles. *Sf9* cells were disrupted by sonication on ice. HEK cells were lysed by resuspension in detergent-containing buffer (typically 40 mM DDM). The following cocktail of protease inhibitors was used for all large-scale purification protocols described here: 3 μg/ml aprotinin, 2 mM benzamidine, 5 μg/ml leupeptin, 2 μg/ml pepstatin A, 200 μg/ml 4-(2-Aminoethyl) benzenesulfonyl fluoride hydrochloride, and 250 μM phenylmethane sulphonylfluoride (Sigma-Aldrich). Deoxyribonuclease (DNase) 1 (Worthington) was also included in all lysis buffers.

Purification of detergent-solubilized SLO1 channels

Pichia or *Sf9* cells expressing human or *Aplysia* SLO1 GFP-1D4 constructs were lysed at 4°C in buffer containing: 150 mM KCl; 50 mM HEPES KOH; 50 mM DDM or DM; final pH 8.0, containing DNase and protease inhibitors. Lysate was incubated for 3 hours at 4°C to allow membrane protein extraction, then clarified by centrifugation (30,000xg, 45', 4°C). Supernatant was added to 1D4-affinity

resin pre-equilibrated in 150 mM KCl, 10 mM HEPES KOH, 4 mM DM, final pH: 7.4. Suspension was layered with argon gas and incubated overnight at 4°C, mixing by gentle inversion. Resin was collected on a column by gravity, washed with 2 column volumes (CV) of buffer (150 mM KCl, 10 mM HEPES KOH, 4 mM DM, final pH: 7.4, flow rate 0.2 mL/min), and eluted in buffer supplemented with 1 mg/ml 1D4 peptide (AnaSpec, Inc.) over 1 hour at room temperature. 10 mM DTT and PreScission protease (1:40 w/w) were added to the eluted protein. Protease cleavage was carried out for 4 hours at 4°C, after which the protein was concentrated and further purified by gel filtration at 4°C on a Superose-6 column in buffer containing: 150 mM KCl; 20 mM HEPES KOH; 6 mM DM 10 mM DTT; final pH: 7.4. The fraction corresponding to the tetramer peak was isolated and concentrated to ~1-5 mg/mL.

Purification of CTD constructs

CTD constructs of human hSLO1, chicken gSLO2.2, zebrafish zSLO1 and human hSLO3 were expressed as GFP-His_{10} fusions in *Sf9* cells. The following buffers were used during cell lysis at 4°C. For hSLO1, gSLO2.2 and zSLO1 (in mM): 300 NaCl, 50 HEPES pH 8.0, 10 imidazole, and 5 β-mercaptoethanol (β–ME), containing DNase and protease inhibitors. For hSLO3 (in mM): 500 KCl; 50 K-phosphate; 10 imidazole and 5 β–ME, final pH 8.0, containing DNase and protease inhibitors. The cell lysate was clarified by ultracentrifugation (250,000xg, 80', 4°C). Supernatant was applied by gravity onto TALON metal affinity resin (Clontech) pre-equilibrated in lysis buffer, at 4°C. The resin was then washed with 10 column volumes of lysis buffer supplemented with extra 10 mM imidazole and eluted in lysis buffer supplemented with extra 290 mM imidazole (all steps at 4°C). 10 mM DTT and PreScission protease (1:40 w/w) were added to the eluted protein. Protease cleavage was carried out overnight at

4°C, after which the protein was concentrated and further purified by gel filtration at 4°C on a Superose-6 column. The following gel filtration buffers were used. For hSLO1 (in mM): 150 NaCl, 20 TRIS pH 8.0, 50 $CaCl_2$, 20 DTT, and 1.5 TRIS(2-carboxyethyl)phosphine (TCEP). For gSLO2.2 (in mM): 500 NaCl, 20 TRIS pH 8.0, 20 DTT, and 1.5 TCEP. For zSLO1 (in mM): 150 NaCl, 20 HEPES pH 8.0, 20 DTT. For hSLO3 (in mM): 500 KCl, 20 K-phosphate, 20 DTT, 1.5 TCEP, final pH 8.5. For crystallization experiments, all proteins were concentrated to 5-6 mg/mL. For the zSLO1 CTD, 10 mM $CaCl_2$ was added to the protein before crystallization.

2) IbTx binding studies

Recombinant IbTx expression and purification

Recombinant iberiotoxin (IbTx) expression in *E. coli* was based on protocols originally described for charybdotoxin (188, 212), with minor modifications. IbTx was expressed in *E. coli* BL21(DE3) cells as a fusion construct containing the T7 gene 9 sequence and a factor Xa cleavage site before the toxin N-terminus. Large-scale bacterial cultures were grown in standard LB medium at 37°C and protein expression was induced when OD_{600} reached 0.9 using 0.5 mM IPTG. Induction was carried out for 2.5 hours, after which the cells were pelleted and flash-frozen in liquid N_2. Cells were resuspended in ice-cold lysis buffer (in mM): 50 NaCl, 10 TRIS pH 8.0, 2 EDTA, 7 β–ME, containing DNase and protease inhibitors. Mechanical lysis was performed using a French press. The lysate was clarified by centrifugation (30,000xg, 45', 4°C), after which DNA was precipitated using 30% w/v streptomycin sulfate, stirring for 10' on ice. The solution was spun down (30,000xg, 20', 4°C), and solid ammonium sulfate was slowly added to the supernatant (31 g ammonium sulfate per 100 mL of supernatant, i.e. 50%

saturation). Ammonium sulfate precipitation was carried on overnight at 4°C under gentle stirring. The precipitate was collected by centrifugation (30,000xg, 20′, 4°C) and the pellet dissolved in 50 mM NaCl, 50 mM TRIS pH 7.0, 5 mM β-ME. The T7 gene 9-IbTx fusion was then purified by ion-exchange chromatography on a DE-52 column at 4°C (salt gradient: 50 to 500 mM NaCl in 50 mM TRIS pH 7.0, 5 mM β-ME). Fractions containing the fusion protein were dialyzed against 100 mM NaCl, 20 mM HEPES pH 8.0, 1 mM β-ME for 3 days at 4°C. After diluting the dialyzed protein solution to A_{280} = 2.0 (in dialysis buffer), 1 mM $CaCl_2$ was added and the fusion protein was cleaved using 10 μg/mL trypsin (45′ at room temperature (RT), stirring). IbTx was isolated using ion-exchange chromatography on a mono-S column (salt gradient: 10-1000 mM NaCl in 10 mM HEPES, pH 8.0). The main fraction (pure IbTx) was isolated and supplemented with 5% v/v acetic acid, then incubated for 4 hours at 65°C for cyclization of the N-terminal glutamine. IbTx was then further purified by HPLC on a C_{18} column, using a 10-45 % gradient (buffer A: 0.1 % trifluoroacetic acid (TFA) in H_2O; buffer B: 0.1 % TFA in 9:1 acetonitrile:H_2O). The purified IbTx was collected and lyophilized, and its mass confirmed by mass spectrometry.

For the purification of the IbTx-D19C mutant, the same protocol was followed except that a glutathione adduct was formed after trypsin cleavage by the sequential addition of 0.5 mM DTT (30′ at RT, stirring) and oxidized glutathione (1h at RT, stirring).

IbTx resin generation

The gluthatione-protected IbTx-D19C mutant was reacted with 10 mM DTT in 50 mM Na-phosphate pH 7.0 (30′ at RT), and the reduced toxin was purified by HPLC as described above. The IbTx-D19C fraction was lyophilized in a vacuum concentrator and dissolved in coupling buffer (50 mM TRIS pH 8.2, 5 mM Na-

EDTA), then incubated at RT for 30 minutes. The toxin was then coupled to SulfoLink resin (Pierce) using the free sulfhydryl group of the introduced Cys19 (5 hours at RT with gentle stirring). Any unreacted iodoacetamide groups on the resin were then capped by treatment of the resin with 1% β-ME in coupling buffer for 1 h at RT. Following the capping reaction, the resin was extensively washed in coupling buffer, and stored at 4°C as 50 % slurry in 50 mM NaCl, 10 mM Na-phosphate pH 7.0, 0.05 % Na-azide. A control resin "mock" resin was also produced in which the iodoacetamide groups were simply capped with 1% β-ME.

IbTx labeling

The IbTx-D19C mutant was labeled using maleimide derivatives by reaction onto the sulfhydryl group of the introduced Cys19 using protocols previously described for ChTx (188). Briefly, IbTx-D19C was deprotected and HPLC purified as described above. The deprotected toxin was then reacted using slight excess (1.1 x) of NEM derivatives in 50 mM NaCl, 50 mM Na-phosphate pH 7.0. The reaction was carried out for 15 minutes at room temperature, after which the labeled IbTx was purified by HPLC as described above. Two maleimide derivatives were used: the fluorescent tetramethylrhodamine-5-maleimide (Molecular Probes) and the radioactive ^{14}C-N-ethylmaleimide (Perkin Elmer). For the reaction with ^{14}C-N-ethylmaleimide, two diastereomers were obtained and both forms were used. Masses of the labeled compounds were confirmed by mass spectrometry. To measure the specific activity of ^{14}C-IbTx, toxin concentration was determined using absorbance at 280 nm and the theortical extinction coefficient predicted on the basis of the amino-acid sequence: $\varepsilon = 7400$ M^{-1} cm^{-1}. The measured specific activity was 31.5 ±0.3 Ci/mol.

IbTx pull-down assays and ^{14}C-IbTx binding assays

To avoid the use of reducing agents during the IbTx binding assays on solubilized SLO1 channels, 5 mM iodoacetamide was added at the beginning of cell lysis during SLO1 purification to cap endogenous cysteines. Then, reducing agents were omitted during all the steps of channel purification described above.

Pull-down assays were typically performed in assay buffer containing 150 KCl (unless stated otherwise), 50 HEPES pH 8.0 and 3 mM DM. 150 μL of solution containing solubilized SLO1 channel was incubated with 20 μL of IbTx-resin (40 μL of 50 % slurry) and binding was carried out at room temperature for 90 minutes under gentle mixing. The beads were then washed extensively in ice-cold assay buffer (using sequential centrifugation steps). Resin-bound channels were eluted by boiling the resin in 1x SDS-sample buffer before SDS-PAGE analysis.

^{14}C-IbTx binding assays were performed following previously described protocols (182, 183), with a few modifications. SLO1 channels were purified in binding buffer containing 150 mM KCl, 20 mM HEPES pH 7.4, 50 mM $CaCl_2$ and 6 mM DM. Binding reaction were set up in a total volume of 100 μL by mixing 100 nM receptor (i.e., tetrameric channel) with 10-1000 nM ^{14}C-IbTx and incubating the reaction for 1 hour at RT with gentle shaking. Channel-toxin complexes were recovered on G4 glass filters (Whatman) pre-incubated in 0.5 % polyethyleneimine (in H_2O). The filters were washed extensively in ice-cold buffer (150 mM KCl, 20 mM HEPES pH 7.4) using a vacuum filtering system. The washed filters were finally counted for ^{14}C radiation by scintillation. Non-specific binding was determined from control samples containing a large excess (> 60 x) of unlabeled IbTx.

3) Crystallization and structure determination

Monomeric Ca^{2+}-bound hSLO1 CTD structure and gSLO2.2 crystals

The hSLO1 CTD was crystallized at 20°C by hanging-drop vapor diffusion against reservoir solution containing 50 mM TRIS, 9-12% (v:v) PEG 400, and 100 mM potassium phosphate (pH 8.0). Tetragonal crystals belonging to space group I422 grew to full size within a week and were cryoprotected by increasing the concentration of PEG 400 to 30% in the reservoir solution supplemented with 500 mM NaCl. Diffraction data for native crystals of human SLO1 CTD were measured at the Advanced Photon Source beamline 24 ID-C. Diffraction data for selenomethionine-substituted crystals of the hSLO1 CTD and the gSLO2.2 CTD crystals were collected at beamline X29 from the National Synchrotron Light Source. All diffraction images were processed with the HKL2000 program suite (213). Initial MAD phasing for hSLO1 CTD was calculated using SOLVE/RESOLVE (214). Thirteen selenium sites were found and the solvent-flattened electron density map at 3.3 Å resolution was of high quality. The protein chain was readily traceable and iterative model building was carried out in COOT (215). Rounds of refinement were performed with REFMAC. The final model was refined to 3.0 Å resolution with R_{work} = 0.246 and R_{free} = 0.278. A few disordered loop regions were not built due to poor electron density and the final refined model includes residues 343-570, 577-613, 677-806, 817-833, 869-945, 949-1020, and 1025-1056. All side chains but two (L353 and W477) were modeled. The majority (94.6%) of the residues lie in the most favored region in a Ramachandran plot (216), with the remaining 5.4% in the additionally allowed regions. One Ca^{2+} ion and one SO_4^{2-} were modeled in the structure. For molecular replacement, a poly-alanine model for the refined SLO1 CTD structure was used as the search model against the 6.0 Å diffraction data from the gSLO2.2 CTD. A

unique solution with a standout Z-score was identified using the program PHASER (1). Data collection and structure refinement statistics are shown in Table 1. All structural illustrations and electron density maps were prepared with PYMOL (www.pymol.org).

Open structure of the zSLO1 gating ring

Crystals of the zebrafish SLO1 CTD were grown at 20°C using hanging-drop vapor diffusion by mixing equal volumes of protein and a reservoir solution containing 50 mM 2-(N-morpholino)ethanesulfonic acid (MES), 4% (w/v) PEG 4000 and 100 mM potassium sodium tartrate (pH 6.3). The crystals grew to a maximum size of about 0.2 mm x 0.2 mm x 0.3 mm within three days. Before being flash frozen in liquid nitrogen, the crystals were briefly transferred to a cryoprotectant solution containing 50 mM MES, 6% (w/v) PEG 4000, 100mM potassium sodium tartrate, 150mM NaCl, 10 mM $CaCl_2$ and 30% ethylene glycol (pH 6.3). The crystals belong to space group $P2_12_12_1$ and the unit cell has dimensions of a = 137.65 Å, b = 210.82 Å and c = 238.76 Å with $\alpha = \beta = \gamma = 90°$. Each asymmetric unit contains eight protein subunits.

Diffraction data were measured at beamline X29 of the National Synchrotron Light Source and were processed with the HKL2000 program suite (1). The scaled data set was anisotropically corrected to resolution limits of 4.0, 3.6 and 3.6 Å along the reciprocal cell directions a*, b*, and c*, respectively, using the diffraction anisotropy server at the University of California, Los Angeles (200). An isotropic B factor of 229.98 $Å^2$ was applied to restore the magnitude of the high-resolution reflections diminished by anisotropic scaling. The structure was determined by molecular replacement using the monomeric Ca^{2+}-bound human SLO1 CTD (PDB ID 3MT5) as the search model. Initial phases were improved by eight-fold non-crystallographic symmetry averaging carried out with DM from

the CCP4 program suite (217). Iterative model building was carried out in COOT (1). Rounds of refinement were performed with CNS (218) and REFMAC (219), and strong eight-fold non-crystallographic symmetry restraints were maintained throughout refinement. The final model was refined to a resolution of 3.6 Å with R_{work} = 0.260 and R_{free} = 0.289. A few disordered regions were not modeled owing to weak electron density, and the final refined model includes residues 343–571, 581–614, 688–810, 817–837, 875–949, 953–1,024 and 1,029–1,059. Residues for which side-chain density was poorly defined were modeled as alanines. The majority (95.9%) of the residues lie in the most favored region in a Ramachandran plot, with the remaining 4.1% in the additionally allowed regions. Eight Ca^{2+} ions were modeled in the Ca^{2+} bowls from the two gating rings in the crystal. Data collection and structure refinement statistics are shown in Table 2. All structural illustrations were prepared with PYMOL (www.pymol.org). The multiple-chain morphing script for CNS (220) was used to generate coordinates for the movies described in Chapter 3.

hSLO3 gating ring structure

Crystals of the human SLO3 CTD were grown at 20°C using hanging-drop vapor diffusion by mixing equal volumes of protein and a reservoir solution containing 50 mM K-phosphate, 3% (w/v) PEG12000 and 1 M ammonium formate (final pH: 6.3). The pH of the final solution obtained by mixing equal amounts of protein and reservoir solutions was measured to be 6.8. The crystals grew to a maximum size of about 0.4 mm x 0.15 mm x 0.05 mm within three days. Crystals were sequentially transferred into cryoprotective solutions (all containing 500 mM KCl, 70 mM K-phosphate, 4% (w/v) PEG12000, 1 M ammonium formate, final pH 6.4) containing increasing concentrations of ethylene glycol (5%, 10%, 20%, final ethylene glycol concentration of 30 % (w/v)) before being flash-frozen

in liquid N_2. The crystals belong to space group I222 and the unit cell has dimensions of a = 124.54 Å, b = 157.94 Å and c = 249.01 Å with $\alpha = \beta = \gamma = 90°$. Each asymmetric unit contains two CTD subunits.

Diffraction data were measured at beamline X29 of the National Synchrotron Light Source and were processed with the HKL2000 program suite (213). Diffraction of X-rays by these crystals was very anisotropic, and analysis revealed that diffraction in the a* and b* directions of the reciprocal cell are the weakest. In the final dataset used for structure determination, diffraction data collected from two independent crystals that varied in their degree of diffraction anisotropy were merged. These reflections were scaled together in SCALEPACK (213) to produce a unique, final dataset. The scaled data set was anisotropically corrected to resolution limits of 3.8, 3.4 and 3.3 Å along the reciprocal cell directions a*, b*, and c*, respectively, using the diffraction anisotropy server at the University of California, Los Angeles (200). An isotropic B factor of 105.89 $Å^2$ was applied to restore the magnitude of the high-resolution reflections diminished by anisotropic scaling. The structure was determined by molecular replacement using the monomeric Ca^{2+}-bound human SLO1 CTD (PDB ID 3MT5) as the search model. Structure refinement was carried out in REFMAC (219) using strong two-fold non-crystallographic symmetry restraints. Iterative model building was carried out in COOT (215). The final model was refined to a resolution of 3.4 Å with R_{work} = 0.248 and R_{free} = 0.268. A few disordered regions were not modeled owing to weak electron density, and the final refined model includes residues 332–353, 362–371, 378–559, 567–601, 681–702, 706–806, 812-829, 858-932, 952-970, 981-1007, 1014-1040 and 1,029–1,059. Residues for which side-chain density was poorly defined were modeled as alanines. The majority (93.0%) of the residues lie in the most favored region in a Ramachandran plot, with the remaining 7% in the additionally allowed regions. Data collection and

structure refinement statistics are shown in Table 3. All structural illustrations were prepared with PYMOL (www.pymol.org).

4) Electrophysiology

Purified SLO1 channel reconstitution

Channel reconstitution was done following the procedure described in (221). Lipids (1-Palmitoyl-2-oleoyl-*sn*-glycero-3-phosphoethanolamine: 1-Palmitoyl-2-oleoyl-*sn*-glycero-3-phosphoglycerol, i.e. POPE:POPG, 3:1 w/w) in chloroform were transferred with a glass syringe into a glass test tube, dried with an argon stream, washed with pentane, and then placed under room vacuum for 30 minutes. Dried lipids were then hydrated with dialysis buffer containing 450 mM KCl and 10 mM HEPES-KOH pH 7.4 at a lipid concentration of 10 mg/ml. The lipid suspension was vortexed briefly and sonicated 5-10 times (30 second each) to produce small unilamellar vesicles. DM was added into the vesicle suspension to a final concentration of 10 mM. The mixture was rotated for 30 minutes at room temperature and then solubilized SLO1 protein was added to the lipid/detergent mixture to a protein-to-lipid ratio (w/w) ranging from 0.1 to 1.0. Detergent concentration was then raised to 17.5 mM. The mixture was incubated for two hours at room temperature and then dialyzed against the dialysis buffer at 4°C. The buffer was changed every 12 hours. After three days the vesicles were collected, flash-frozen with liquid nitrogen, and stored at −80°C.

Bilayer recordings

The bilayer experiments followed published procedures (221, 222). Lipids (POPE:POPG 3:1 w/w) were dried under argon and dissolved in decane, then

were painted over a 300 μm hole in a polystyrene partition that separated two aqueous chambers. Once formation and thinning of a planar lipid membrane was detected through monitoring of the electrical capacitance, lipid vesicles were delivered to the membrane surface with a pipette. Vesicle fusion was facilitated by the presence of a salt gradient across the membrane: 15 mM KCl on the side opposite vesicle addition (trans side) and 150 mM KCl on the side of vesicle addition (cis side). Both sides were buffered with 10 mM HEPES-KOH at pH 7.4. After vesicle fusion, the salt concentration on the trans side was raised to 150 mM.

Patch-clamp electrophysiology

Full length hSLO3 channel was cloned into the pGEM-HE vector (223). The constructs of mSLO3 in pOX (94) and of human and mouse LRRC52 in pXMX were generous gifts from L. Salkoff and C. Lingle, respectively. Plasmids were linearized and capped cRNA was produced by *in vitro* transcription using the mMessage mMachine reagents (Invitrogen). cRNA was purified using phenol/chloroform extraction and ethanol purification, and stored at -80°C. Oocytes were dissected from anesthetized *Xenopus leavis* (African clawed frogs) by a survival surgery. Oocytes were immediately treated with collagenase (2 mg/mL) for 1.5 hours, rinsed with a Ca^{2+}-free OR-2 solution (82.5 mM NaCl, 2.5 mM KCl, 1 mM $MgCl_2$, 5 mM HEPES pH 7.6) and stored in ND-96 solution (96 mM NaCl, 2 mM KCl, 1.8 mM $CaCl_2$, 1 mM $MgCl_2$, 5 mM HEPES pH 7.6) containing fresh gentamycin (50 mg/L). Within 2 days of dissection, oocytes were injected with ~10 ng of purified RNA. For SLO3/LRRC52 co-expression studies, the two constructs were injected in a 1:1 w/w ratio. Electrophysiological measurements were made 3-6 days after injection. Oocytes were incubated at 18°C.

For recording, inside-out patches were excised from freshly devitellinized oocytes using fire-polished glass pipettes with a typical resistance of 0.8-1.2 MΩ. Large pipettes were used in order to increase the amplitude of SLO3 current in a patch. Axopatch amplifier 200B (Axon Instruments), a digitizer (Axon Instruments DigiData 1440A) and Clampex 10.2 software (Axon Instruments) were used in the recording of data. Patches were excised in an inside-out configuration, exposing the intracellular face of membrane and embedded channels to a bath solution controlled by a custom-built gravity-flow perfusion system. Pipette solution contained (in mM): 140 K-gluconate, 20 HEPES, 2 $MgCl_2$, with pH adjusted to 7.0. Bath solutions contained (in mM): 140 K-gluconate, 20 HEPES, 5 EGTA (acid form), and pH was carefully adjusted with KOH to the desired value. During recording, the membrane voltage was held at -60 mV and currents were elicited by pulsing the voltage from -140 to +180mV in 20-mV increments.

TABLES

Table 1: Summary of crystallography data for the monomeric Ca^{2+}-bound hSLO1 CTD structure presented in Chapter 3

Datasets	Native	Selenium			gslo2.2 CTD
Resolution (Å)	3.0	3.3			6.0
Space Group	$P6_322$	$P6_322$			I422
Source	APS 24ID-C	BNL X29			BNL X29
Cell Constants a, b, c (Å) a, b, g((°))	a = b = 144.5 c = 182.2 90, 90, 120	a = b = 145.1 c = 182.4 90, 90, 120			a = b = 126.3 c = 239.0 90, 90, 90
		Peak	Inflection	Remote	
Wavelength (Å)	0.9792	0.9792	0.9793	0.9640	1.0750
Completeness (%)	99.9 (99.9)	99.8 (100)	99.8 (100)	99.8 (100)	95.3 (96.7)
R_{merge}	0.089 (0.738)	0.105 (0.493)	0.100 (0.533)	0.130 (0.745)	0.108 (0.746)
Reflections	23149	17611	17641	17649	2520
I/σ	19.6 (2.4)	18.8 (3.3)	18.2 (3.1)	13.9 (2.2)	21.4 (3.1)
Redundancy	5.8 (5.9)	7.0 (7.2)	7.0 (7.2)	7.0 (7.2)	9.1 (9.6)
MAD Phasing (SOLVE/RESOLVE)					
Number of sites	13				
Resolution (Å)	3.3				
Overall Figure of Merit	0.70				
Refinement					
Resolution (Å)	50 - 3.0				
R_{work}	0.249 (0.327)				
R_{free}	0.282 (0.324)				
Number of atoms					
Protein	4692				
Ligand (Ca^{2+})	1				
Average B factors ($Å^2$)	67.1				
Ramachandron plot					
Favored (%)	94.3				
Allowed (%)	5.7				
Disallowed (%)	0				
RMSD Bond lengths(Å)	0.010				
RMSD Bond angles (°)	1.214				

R_{free} was calculated with 5% of the data.
Numbers in parentheses represent values in the highest-resolution shell.

Table 2: Summary of crystallography data for the Ca^{2+}-bound zSLO1 gating ring structure presented in Chapter 3

	Zebrafish SLO1 CTD
Data collection	
Resolution (Å)	3.6
Space group	$P2_12_12_1$
Source	BNL X29
Cell dimensions: *a*, *b*, *c* (Å)	137.65, 210.82, 238.76
α, *β*, *γ*((°))	90, 90, 90
Wavelength (Å)	1.075
Completeness (%)	99.4 (99.5)
R_{merge}	0.103 (0.794)
$I/\sigma I$	11.9 (1.5)
Redundancy	4.2 (4.2)
Refinement	
Resolution (Å)	
Low	48
High (*a**, *b**, *c**)[a]	4.0, 3.6, 3.6
No. of reflections (total / test)	71878 / 3620
Completeness (%)[b]	93.8 (30.9)
R_{work}	0.283 (0.386)
R_{free}	0.293 (0.391)
Number of atoms	
Protein	37304
Ligands (Ca^{2+})	8
Average B factors ($Å^2$)	99.3
Ramachandron plot	
Favored (%)	95.9
Allowed (%)	4.1
Disallowed (%)	0
RMSD Bond lengths (Å)	0.007
RMSD Bond angles (°)	1.138

R_{free} was calculated with ~5% of the data.
Numbers in parentheses represent values in the highest-resolution shell.
[a] Reflections beyond these limits were excluded from refinement after anisotropic correction (*a**, *b**, and *c** indicate reciprocal cell directions).
[b] Completeness after anisotropic correction.

Table 3: Summary of crystallography data for the hSLO3 gating ring structure presented in Chapter 4

Datasets	Dataset #1	Dataset #2	Merged dataset
Resolution (Å)	3.3	3.4	3.3
Space Group	I222	I222	I222
Source	BNL X29	BNL X29	
Cell Constants a, b, c (Å)	a = 124.10 b= 158.90 c = 248.27	a = 124.53 b= 157.94 c = 249.00	a = 124.54 b = 157.94 c = 249.00
α, β, γ((°))	90, 90, 90	90, 90, 90	90, 90, 90
Wavelength (Å)	1.075	1.29	
Completeness (%)	99.6 (100)	99.7 (100)	99.9 (100)
R_{merge}	0.081 (0.810)	0.095 (0.957)	0.124 (>1)
Reflections	23149	17611	2520
I/σ	15.9 (1.6)	12.5 (1.3)	15.0 (1.8)
Redundancy	4.8 (4.8)	3.5 (3.4)	8.3 (8.3)
Refinement (using anisotropic correction)			
Resolution (Å)	50 - 3.4 (a*, b*, c*: 3.8, 3.4, 3.4)[a]		
Completeness[b]	90.0 (38.6)		
R_{work}	0.248 (0.324)		
R_{free}	0.266 (0.286)		
Number of atoms			
Protein	8154		
Average B factors (Å^2)	69.6		
Ramachandron plot			
Favored (%)	93		
Allowed (%)	7		
Disallowed (%)	0		
RMSD Bond lengths(Å)	0.008		
RMSD Bond angles (°)	1.002		

R_{free} was calculated with 5% of the data.
Numbers in parentheses represent values in the highest-resolution shell.
[a] Reflections beyond these limits were excluded from refinement after anisotropic correction (*a**, *b**, and *c** indicate reciprocal cell directions).
[b] Completeness after anisotropic correction

APPENDIX

Appendix A: Sequence alignment of SLO family RCK domains

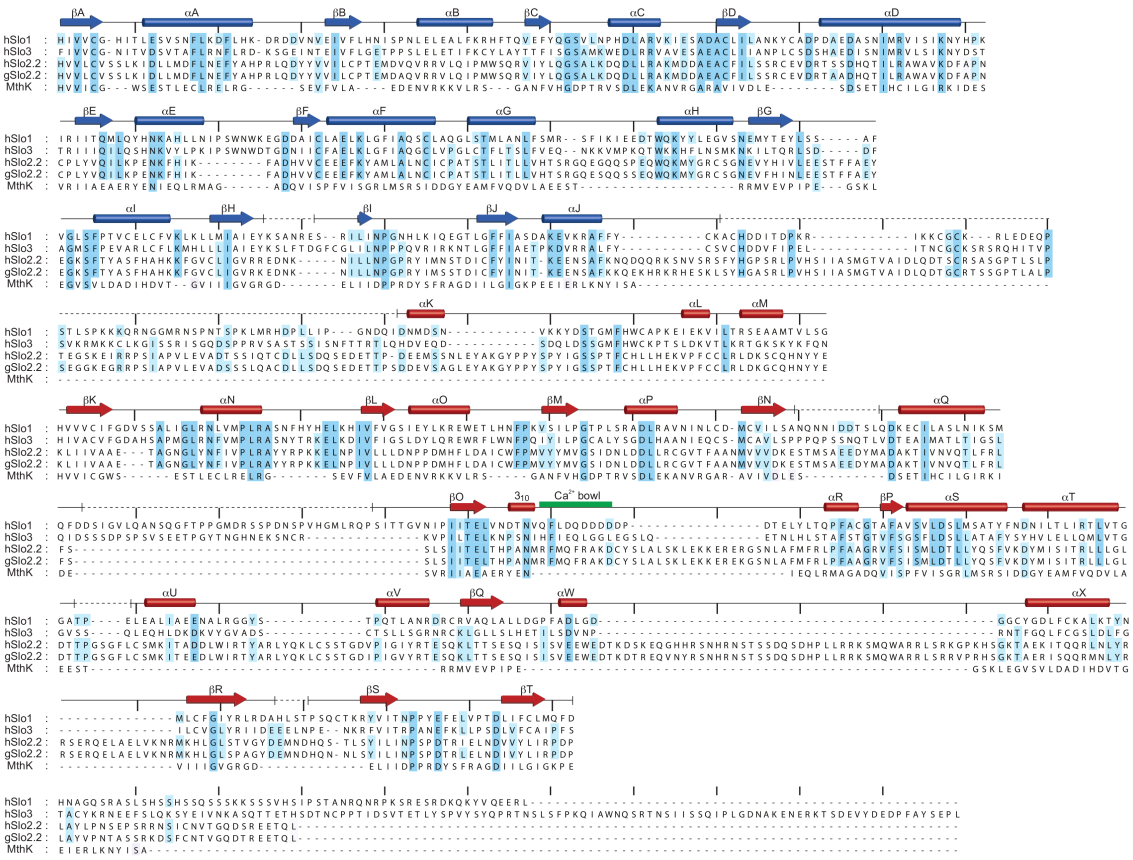

Sequence alignment of SLO family RCK domains. Human sequences representing the three main families of SLO channels (hSLO1, hSLO2.2 and hSLO3) are aligned together with a chicken SLO2 family member (gSLO2.2) and MthK. The alignment of hSLO1 and MthK is based on their known RCK domain structures. The MthK sequence is repeated to align to the second RCK domain present in SLO family sequences. In regions with low sequence identity and significant insertions and deletions, manual alignment was aided by the SLO1 structure. Two levels of shading indicate sequence identity across all SLO family members (dark blue) versus identity across only 3 of 4 representative members (light blue). The same shading is extended to the MthK sequence when identical to the Slo family sets. The definition of sequence identity was relaxed to include D/E and K/R substitutions.

Appendix B: List of point mutations tested on mouse SLO3

E161Q*	H417A	K871A
D162N*	H423A	H877A
K320N	K479A	E880Q
K329N	E502Q	D886N
K332A	K505A	H895A
D343N	K510A	D912N
H354A	H511A	Y920F
K356A	K515A	H923A
E359Q	H516A	R1005A
E363Q	K522A	D1010N[#]
C382A	K524A	E1011Q[#]
H383A	H607A	E1012Q[#]
R401A	R709A	E1013Q[#]
R402A	R770A	R1020A

*tested in the same construct

[#]tested in the same construct

REFERENCES

1. Hille B. 2001. Ion channels of excitable membranes 3rd ed HILLE Bertil: Librairie Lavoisier. *Sunderland*:.

2. Ackerman MJ and Clapham DE. 1997. Ion channels--basic science and clinical disease. *N. Engl. J. Med.* 336(22):1575–1586.

3. Seyfarth E-A. 2006. Julius Bernstein (1839–1917): pioneer neurobiologist and biophysicist. *Biol Cybern* 94(1):2–8.

4. Gouaux E and MacKinnon R. 2005. Principles of selective ion transport in channels and pumps. *Science* 310(5753):1461–1465.

5. MacKinnon R. 2004. Potassium channels and the atomic basis of selective ion conduction (Nobel Lecture). 4265–4277.

6. Rudy B. 1988. Diversity and ubiquity of K channels. *Neuroscience* 25(3):729–749.

7. Coetzee WA, Amarillo Y, Chiu J, Chow A, Lau D, McCormack T, Moreno H, et al. 1999. Molecular diversity of K+ channels. *Ann. N. Y. Acad. Sci.* 868:233–285.

8. Jentsch TJ, Stein V, Weinreich F, and Zdebik AA. 2002. Molecular structure and physiological function of chloride channels. *Physiol. Rev.* 82(2):503–568.

9. Armstrong C and Hille B. 1998. Voltage-Gated Ion Channels Review and Electrical Excitability. *Neuron*:.

10. Catterall WA. 1995. Structure and function of voltage-gated ion channels. *Annu. Rev. Biochem.* 64:493–531.

11. Hodgkin AL and Huxley AF. 1952. A quantitative description of membrane current and its application to conduction and excitation in nerve. *J. Physiol. (Lond.)* 117(4):500–544.

12. Murata Y, Iwasaki H, Sasaki M, Inaba K, and Okamura Y. 2005. Phosphoinositide phosphatase activity coupled to an intrinsic voltage sensor. *Nature* 435(7046):1239–1243.

13. Diss JKJ, Fraser SP, and Djamgoz MBA. 2004. Voltage-gated Na+ channels: multiplicity of expression, plasticity, functional implications and pathophysiological aspects. *Eur. Biophys. J.* 33(3):180–193.
14. Sibaoka T. 1962. Excitable cells in Mimosa. *Science* 137(3525):226.

15. Pickard BG. 1973. Action Potentials in Higher Plants. *Botanical Review* 39(2):172–201. New York Botanical Garden Press.

16. Eckert R and Brehm P. 1979. Ionic mechanisms of excitation in Paramecium. *Annu. Rev. Biophys. Bioeng.* 8:353–383.

17. Kralj JM, Hochbaum DR, Douglass AD, and Cohen AE. 2011. Electrical Spiking in Escherichia coli Probed with a Fluorescent Voltage-Indicating Protein. *Science* 333(6040):345–348.

18. Salkoff L, Butler A, Ferreira G, Santi C, and Wei A. 2006. High-conductance potassium channels of the SLO family. *Nat. Rev. Neurosci.* 7(12):921–931.

19. MacKinnon R. 1991. Determination of the subunit stoichiometry of a voltage-activated potassium channel. *Nature* 350(6315):232–235.

20. Shen K, Lagrutta A, Davies N, Standen N, Adelman J, and Morth R. 1994. Tetraethylammonium Block of Slowpoke Calcium-Activated Potassium Channels Expressed in Xenopus-Oocytes - Evidence for Tetrameric Channel Formation. *Pflugers Arch.* 426(5):440–445.

21. Cui J, Yang H, and Lee US. 2009. Molecular mechanisms of BK channel activation. *Cell. Mol. Life Sci.* 66(5):852–875.

22. Meera P, Wallner M, Song M, and Toro L. 1997. Large conductance voltage- and calcium-dependent K+ channel, a distinct member of voltage-dependent ion channels with seven N-terminal transmembrane segments (S0-S6), an extracellular N terminus, and an intracellular (S9-S10) C terminus. *Proc. Natl. Acad. Sci. U.S.A.* 94(25):14066–14071.

23. Xia X-M, Zhang X, and Lingle CJ. 2004. Ligand-dependent activation of Slo family channels is defined by interchangeable cytosolic domains. *J. Neurosci.* 24(24):5585–5591.

24. Jiang Y, Pico A, Cadene M, Chait BT, and MacKinnon R. 2001. Structure of the RCK domain from the E. coli K+ channel and demonstration of its presence in the human BK channel. *Neuron* 29(3):593–601.

25. Jaggar JH, Porter VA, Lederer WJ, and Nelson MT. 2000. Calcium sparks in smooth muscle. *Am. J. Physiol., Cell Physiol.* 278(2):C235–56.

26. Orio P, Rojas P, Ferreira G, and Latorre R. 2002. New disguises for an old channel: MaxiK channel beta-subunits. *News Physiol. Sci.* 17:156–161.

27. Robitaille R, Garcia ML, Kaczorowski GJ, and Charlton MP. 1993. Functional colocalization of calcium and calcium-gated potassium channels in control of transmitter release. *Neuron* 11(4):645–655.

28. Gola M and Crest M. 1993. Colocalization of active KCa channels and Ca2+ channels within Ca2+ domains in helix neurons. *Neuron* 10(4):689–699.

29. Grunnet M. 2004. Coassembly of Big Conductance Ca2+-activated K+ Channels and L-type Voltage-gated Ca2+ Channels in Rat Brain. *J. Biol. Chem.* 279(35):36445–36453.

30. Bhattacharjee A and Kaczmarek L. 2005. For K channels, Na is the new Ca. *Trends Neurosci.* 28(8):422–428.

31. Budelli G, Hage TA, Wei A, Rojas P, Jong Y-JI, O'Malley K, and Salkoff L. 2009. Na+-activated K+ channels express a large delayed outward current in neurons during normal physiology. *Nat. Neurosci.* 12(6):745–750.

32. Lishko P, Kirichok Y, Ren D, Navarro B, Chung J-J, and Clapham DE. 2011. The Control of Male Fertility by Spermatozoan Ion Channels. *Annu. Rev. Physiol.*:.

33. Meech RW. 1978. Calcium-dependent potassium activation in nervous tissues. *Annu. Rev. Biophys. Bioeng.* 7:1–18.

34. Marty A. 1981. Ca-dependent K channels with large unitary conductance in chromaffin cell membranes. *Nature* 291(5815):497–500.

35. Latorre R, Oberhauser A, Labarca P, and Alvarez O. 1989. Varieties of calcium-activated potassium channels. *Annu. Rev. Physiol.* 51:385–399.

36. Marty A. 1983. Ca-2+-Dependent K+ Channels with Large Unitary Conductance. *Trends Neurosci.* 6(7):262–265.

37. Latorre R and Miller C. 1983. Conduction and selectivity in potassium channels. *J. Membr. Biol.* 71(1-2):11–30.

38. Elkins T, Ganetzky B, and Wu CF. 1986. A Drosophila mutation that eliminates a calcium-dependent potassium current. *Proc. Natl. Acad. Sci. U.S.A.* 83(21):8415–8419.

39. Atkinson NS, Robertson GA, and Ganetzky B. 1991. A component of calcium-activated potassium channels encoded by the Drosophila slo locus. *Science* 253(5019):551–555.

40. Adelman JP, Shen KZ, Kavanaugh MP, Warren RA, Wu YN, Lagrutta A, Bond CT, and North RA. 1992. Calcium-activated potassium channels expressed from cloned complementary DNAs. *Neuron* 9(2):209–216.

41. Butler A, Tsunoda S, McCobb DP, Wei A, and Salkoff L. 1993. mSlo, a complex mouse gene encoding "maxi" calcium-activated potassium channels. *Science* 261(5118):221–224.

42. Sausbier U, Sausbier M, Sailer CA, Arntz C, Knaus H-G, Neuhuber W, and Ruth P. 2006. Ca2+ -activated K+ channels of the BK-type in the mouse brain. *Histochem. Cell Biol.* 125(6):725–741.

43. Clapham DE. 1995. Calcium signaling. *Cell* 80(2):259–268.

44. Clapham DE. 2007. Calcium signaling. *Cell* 131(6):1047–1058.

45. Berridge MJ, Lipp P, and Bootman MD. 2000. The versatility and universality of calcium signalling. *Nat. Rev. Mol. Cell Biol.* 1(1):11–21.

46. Ghatta S, Nimmagadda D, Xu X, and O'Rourke ST. 2006. Large-conductance, calcium-activated potassium channels: structural and functional implications. *Pharmacol. Ther.* 110(1):103–116.

47. Faber ESL and Sah P. 2003. Calcium-activated potassium channels: multiple contributions to neuronal function. *Neuroscientist* 9(3):181–194.

48. Suarezkurtz G, Garcia M, and Kaczorowski G. 1991. Effects of Charybdotoxin and Iberiotoxin on the Spontaneous Motility and Tonus of Different Guinea-Pig Smooth-Muscle Tissues. *J Pharmacol Exp Ther* 259(1):439–443.

49. Nelson MT, Cheng H, Rubart M, Santana LF, Bonev AD, Knot HJ, and Lederer WJ. 1995. Relaxation of arterial smooth muscle by calcium sparks. *Science* 270(5236):633–637.

50. Fettiplace R and Fuchs PA. 1999. Mechanisms of hair cell tuning. *Annu. Rev. Physiol.* 61:809–834.

51. Wang ZW, Saifee O, Nonet ML, and Salkoff L. 2001. SLO-1 potassium channels control quantal content of neurotransmitter release at the C. elegans neuromuscular junction. *Neuron* 32(5):867–881.

52. Latorre R, Vergara C, and Hidalgo C. 1982. Reconstitution in Planar Lipid Bilayers of a Ca2+-Dependent K+ Channel from Transverse Tubule Membranes Isolated from Rabbit Skeletal Muscle. *Proc. Natl. Acad. Sci. U.S.A.* 79(3):805–809. National Academy of Sciences.

53. Funabashi K, Ohya S, Yamamura H, Hatano N, Muraki K, Giles W, and Imaizumi Y. 2010. Accelerated Ca2+ entry by membrane hyperpolarization due to Ca2+-activated K+ channel activation in response to histamine in chondrocytes. *AJP: Cell Physiology* 298(4):C786–C797.

54. Gees M, Colsoul B, and Nilius B. 2010. The Role of Transient Receptor Potential Cation Channels in Ca2+ Signaling. *Cold Spring Harbor Perspectives in Biology* 2(10):a003962–a003962.

55. Sausbier M, Hu H, Arntz C, Feil S, Kamm S, Adelsberger H, Sausbier U, et al. 2004. Cerebellar ataxia and Purkinje cell dysfunction caused by Ca2+-activated K+ channel deficiency. *Proc. Natl. Acad. Sci. U.S.A.* 101(25):9474–9478.

56. Sausbier M, Arntz C, Bucurenciu I, Zhao H, Zhou X-B, Sausbier U, Feil S, et al. 2005. Elevated blood pressure linked to primary hyperaldosteronism and impaired vasodilation in BK channel-deficient mice. *Circulation* 112(1):60–68.

57. Meredith AL, Thorneloe KS, Werner ME, Nelson MT, and Aldrich RW. 2004. Overactive bladder and incontinence in the absence of the BK large conductance Ca2+-activated K+ channel. *J. Biol. Chem.* 279(35):36746–36752.

58. Rüttiger L, Sausbier M, Zimmermann U, Winter H, Braig C, Engel J, Knirsch M, et al. 2004. Deletion of the Ca2+-activated potassium (BK) alpha-subunit but not the BKbeta1-subunit leads to progressive hearing loss. *Proc. Natl. Acad. Sci. U.S.A.* 101(35):12922–12927.

59. Werner ME, Zvara P, Meredith AL, Aldrich RW, and Nelson MT. 2005. Erectile dysfunction in mice lacking the large-conductance calcium-activated potassium (BK) channel. *J. Physiol. (Lond.)* 567(Pt 2):545–556.

60. Lu R, Alioua A, Kumar Y, Eghbali M, Stefani E, and Toro L. 2006. MaxiK channel partners: physiological impact. *J. Physiol. (Lond.)* 570(Pt 1):65–72.

61. Fury M, Marx SO, and Marks AR. 2002. Molecular BKology: the study of splicing and dicing. *Sci. STKE* 2002(123):pe12.

62. Schubert R and Nelson MT. 2001. Protein kinases: tuners of the BKCa channel in smooth muscle. *Trends Pharmacol. Sci.* 22(10):505–512.

63. Tian L, Jeffries O, McClafferty H, Molyvdas A, Rowe ICM, Saleem F, Chen L, et al. 2008. Palmitoylation gates phosphorylation-dependent regulation of BK potassium channels. *Proc. Natl. Acad. Sci. U.S.A.* 105(52):21006–21011.

64. Tang XD, Xu R, Reynolds MF, Garcia ML, Heinemann SH, and Hoshi T. 2003. Haem can bind to and inhibit mammalian calcium-dependent Slo1 BK channels. *Nature* 425(6957):531–535.

65. Garcia-Calvo M, Knaus HG, McManus OB, Giangiacomo KM, Kaczorowski GJ, and Garcia ML. 1994. Purification and reconstitution of the high-conductance, calcium-activated potassium channel from tracheal smooth muscle. *J. Biol. Chem.* 269(1):676–682.

66. Knaus HG, Garcia-Calvo M, Kaczorowski GJ, and Garcia ML. 1994. Subunit composition of the high conductance calcium-activated potassium channel from smooth muscle, a representative of the mSlo and slowpoke family of potassium channels. *J. Biol. Chem.* 269(6):3921–3924.

67. Knaus HG, Folander K, Garcia-Calvo M, Garcia ML, Kaczorowski GJ, Smith M, and Swanson R. 1994. Primary sequence and immunological characterization of beta-subunit of high conductance Ca(2+)-activated K+ channel from smooth muscle. *J. Biol. Chem.* 269(25):17274–17278.

68. Xia XM, Ding JP, and Lingle CJ. 1999. Molecular basis for the inactivation of Ca2+- and voltage-dependent BK channels in adrenal chromaffin cells and rat insulinoma tumor cells. *J. Neurosci.* 19(13):5255–5264.

69. Wallner M, Meera P, and Toro L. 1999. Molecular basis of fast inactivation in voltage and Ca2+-activated K+ channels: a transmembrane beta-subunit homolog. *Proc. Natl. Acad. Sci. U.S.A.* 96(7):4137–4142.

70. Uebele VN, Lagrutta A, Wade T, Figueroa DJ, Liu Y, McKenna E, Austin CP, Bennett PB, and Swanson R. 2000. Cloning and functional expression of two families of beta-subunits of the large conductance calcium-activated K+ channel. *J. Biol. Chem.* 275(30):23211–23218.

71. Behrens R, Nolting A, Reimann F, Schwarz M, Waldschütz R, and Pongs O. 2000. hKCNMB3 and hKCNMB4, cloning and characterization of two members of the large-conductance calcium-activated potassium channel beta subunit family. *FEBS Lett.* 474(1):99–106.

72. Meera P, Wallner M, and Toro L. 2000. A neuronal beta subunit (KCNMB4) makes the large conductance, voltage- and Ca2+-activated K+ channel resistant to charybdotoxin and iberiotoxin. *Proc. Natl. Acad. Sci. U.S.A.* 97(10):5562–5567.

73. Weiger TM, Holmqvist MH, Levitan IB, Clark FT, Sprague S, Huang WJ, Ge P, et al. 2000. A novel nervous system beta subunit that downregulates human large conductance calcium-dependent potassium channels. *J. Neurosci.* 20(10):3563–3570.

74. McManus OB, Helms LM, Pallanck L, Ganetzky B, Swanson R, and Leonard RJ. 1995. Functional role of the beta subunit of high conductance calcium-activated potassium channels. *Neuron* 14(3):645–650.

75. Nimigean CM and Magleby KL. 2000. Functional coupling of the beta(1) subunit to the large conductance Ca(2+)-activated K(+) channel in the absence of Ca(2+). Increased Ca(2+) sensitivity from a Ca(2+)-independent mechanism. *J. Gen. Physiol.* 115(6):719–736.

76. Cox DH and Aldrich RW. 2000. Role of the beta1 subunit in large-conductance Ca(2+)-activated K(+) channel gating energetics. Mechanisms of enhanced Ca(2+) sensitivity. *J. Gen. Physiol.* 116(3):411–432.

77. Xia XM, Ding JP, Zeng XH, Duan KL, and Lingle CJ. 2000. Rectification and rapid activation at low Ca2+ of Ca2+-activated, voltage-dependent BK currents: consequences of rapid inactivation by a novel beta subunit. *J. Neurosci.* 20(13):4890–4903.

78. Brenner R, Peréz G, Bonev A, and Eckman D. 2000. Vasoregulation by the 1 subunit of the calcium-activated potassium channel. *Nature*:.

79. Grimm PR, Irsik DL, Settles DC, Holtzclaw JD, and Sansom SC. 2009. Hypertension of Kcnmb1-/- is linked to deficient K secretion and aldosteronism. *Proc. Natl. Acad. Sci. U.S.A.* 106(28):11800–11805.

80. Petkov GV, Bonev AD, Heppner TJ, Brenner R, Aldrich RW, and Nelson MT. 2001. beta1-Subunit of the Ca2+-activated K+ channel regulates contractile activity of mouse urinary bladder smooth muscle. *J. Physiol. (Lond.)* 537(2):443–452.

81. Semenov I, Wang B, Herlihy JT, and Brenner R. 2006. BK channel beta1-subunit regulation of calcium handling and constriction in tracheal smooth muscle. *Am. J. Physiol. Lung Cell Mol. Physiol.* 291(4):L802–10.

82. Brenner R, Chen QH, Vilaythong A, Toney GM, Noebels JL, and Aldrich RW. 2005. BK channel beta4 subunit reduces dentate gyrus excitability and protects against temporal lobe seizures. *Nat. Neurosci.* 8(12):1752–1759.

83. Yan J and Aldrich RW. 2010. LRRC26 auxiliary protein allows BK channel activation at resting voltage without calcium. *Nature* 466(7305):513–516.

84. Dryer SE. 1994. Na(+)-activated K+ channels: a new family of large-conductance ion channels. *Trends Neurosci.* 17(4):155–160.

85. Lawrence C and Rodrigo GC. 1999. A Na+-activated K+ current (IK,Na) is present in guinea-pig but not rat ventricular myocytes. *Pflugers Arch.* 437(6):831–838.

86. Sanchez-Vives MV, Nowak LG, and McCormick DA. 2000. Cellular mechanisms of long-lasting adaptation in visual cortical neurons in vitro. *J. Neurosci.* 20(11):4286–4299.

87. Franceschetti S, Lavazza T, Curia G, Aracri P, Panzica F, Sancini G, Avanzini G, and Magistretti J. 2003. Na+-activated K+ current contributes to postexcitatory hyperpolarization in neocortical intrinsically bursting neurons. *Journal of Neurophysiology* 89(4):2101–2111.

88. Nanou E, Kyriakatos A, Bhattacharjee A, Kaczmarek LK, Paratcha G, and Manira El A. 2008. Na+-mediated coupling between AMPA receptors and KNa channels shapes synaptic transmission. *Proc. Natl. Acad. Sci. U.S.A.* 105(52):20941–20946.

89. Joiner WJ, Tang MD, Wang LY, Dworetzky SI, Boissard CG, Gan L, Gribkoff VK, and Kaczmarek LK. 1998. Formation of intermediate-conductance calcium-activated potassium channels by interaction of Slack and Slo subunits. *Nat. Neurosci.* 1(6):462–469.

90. Yuan A, Santi CM, Wei A, Wang ZW, Pollak K, Nonet M, Kaczmarek L, Crowder CM, and Salkoff L. 2003. The sodium-activated potassium channel is encoded by a member of the Slo gene family. *Neuron* 37(5):765–773.

91. Bhattacharjee A, Joiner WJ, Wu M, Yang Y, Sigworth FJ, and Kaczmarek LK. 2003. Slick (Slo2.1), a rapidly-gating sodium-activated potassium channel inhibited by ATP. *J. Neurosci.* 23(37):11681–11691.

92. Bhattacharjee A, Hehn von CAA, Mei X, and Kaczmarek LK. 2005. Localization of the Na+-activated K+ channel Slick in the rat central nervous system. *J. Comp. Neurol.* 484(1):80–92.

93. Bhattacharjee A, Gan L, and Kaczmarek LK. 2002. Localization of the Slack potassium channel in the rat central nervous system. *J. Comp. Neurol.* 454(3):241–254.

94. Schreiber M, Wei A, Yuan A, Gaut J, Saito M, and Salkoff L. 1998. Slo3, a novel pH-sensitive K+ channel from mammalian spermatocytes. *J. Biol. Chem.* 273(6):3509–3516.

95. Zhang X, Zeng X, and Lingle CJ. 2006. Slo3 K+ channels: voltage and pH dependence of macroscopic currents. *J. Gen. Physiol.* 128(3):317–336.

96. Hamamah S and Gatti JL. 1998. Role of the ionic environment and internal pH on sperm activity. *Hum. Reprod.* 13 Suppl 4:20–30.

97. Lishko PV, Botchkina IL, Fedorenko A, and Kirichok Y. 2010. Acid extrusion from human spermatozoa is mediated by flagellar voltage-gated proton channel. *Cell* 140(3):327–337.

98. Lishko PV and Kirichok Y. 2010. The role of Hv1 and CatSper channels in sperm activation. *J. Physiol. (Lond.)* 588(Pt 23):4667–4672.

99. Kirichok Y, Navarro B, and Clapham DE. 2006. Whole-cell patch-clamp measurements of spermatozoa reveal an alkaline-activated Ca2+ channel. *Nature* 439(7077):737–740.

100. Lishko PV, Botchkina IL, and Kirichok Y. 2011. Progesterone activates the principal Ca2+ channel of human sperm. *Nature* 471(7338):387–391.

101. Navarro B, Kirichok Y, and Clapham DE. 2007. KSper, a pH-sensitive K+ current that controls sperm membrane potential. *Proc. Natl. Acad. Sci. U.S.A.* 104(18):7688–7692.

102. Martínez-López P, Santi CM, Treviño CL, Ocampo-Gutiérrez AY, Acevedo JJ, Alisio A, Salkoff LB, and Darszon A. 2009. Mouse sperm K+ currents stimulated by pH and cAMP possibly coded by Slo3 channels. *Biochem. Biophys. Res. Commun.* 381(2):204–209.

103. Santi CM, Martínez-López P, la Vega-Beltrán de JL, Butler A, Alisio A, Darszon A, and Salkoff L. 2010. The SLO3 sperm-specific potassium channel plays a vital role in male fertility. *FEBS Lett.* 584(5):1041–1046.

104. Zeng X-H, Yang C, Kim ST, Lingle CJ, and Xia X-M. 2011. Deletion of the Slo3 gene abolishes alkalization-activated K+ current in mouse spermatozoa. *Proc. Natl. Acad. Sci. U.S.A.* 108(14):5879–5884.

105. Yang C-T, Zeng X-H, Xia X-M, and Lingle CJ. 2009. Interactions between beta subunits of the KCNMB family and Slo3: beta4 selectively modulates Slo3 expression and function. *PLoS ONE* 4(7):e6135.

106. Yang C, Zeng X-H, Zhou Y, Xia X-M, and Lingle CJ. 2011. LRRC52 (leucine-rich-repeat-containing protein 52), a testis-specific auxiliary subunit of the alkalization-activated Slo3 channel. *Proc. Natl. Acad. Sci. U.S.A.*:.

107. Garcia ML and Kaczorowski GJ. 2005. Potassium channels as targets for therapeutic intervention. *Sci. STKE* 2005(302):pe46.

108. Kaczorowski GJ, McManus OB, Priest BT, and Garcia ML. 2008. Ion channels as drug targets: the next GPCRs. *J. Gen. Physiol.* 131(5):399–405.

109. Kaczorowski GJ, Knaus HG, Leonard RJ, McManus OB, and Garcia ML. 1996. High-conductance calcium-activated potassium channels; structure, pharmacology, and function. *J. Bioenerg. Biomembr.* 28(3):255–267.

110. Ponte CG, McManus OB, Schmalhofer WA, Shen D-M, Dai G, Stevenson A, Sur S, et al. 2012. Selective, Direct Activation of High-conductance, Calcium-activated Potassium Channels Causes Smooth Muscle Reaxation. *Mol. Pharmacol.*:.

111. Seibold MA, Wang B, Eng C, Kumar G, Beckman KB, Sen S, Choudhry S, et al. 2008. An african-specific functional polymorphism in KCNMB1 shows sex-specific association with asthma severity. *Hum. Mol. Genet.* 17(17):2681–2690.

112. Gollasch M, Tank J, Luft FC, Jordan J, Maass P, Krasko C, Sharma AM, Busjahn A, and Bähring S. 2002. The BK channel beta1 subunit gene is associated with human baroreflex and blood pressure regulation. *J. Hypertens.* 20(5):927–933.

113. Jones TR, Charette L, Garcia ML, and Kaczorowski GJ. 1993. Interaction of iberiotoxin with beta-adrenoceptor agonists and sodium nitroprusside on guinea pig trachea. *J. Appl. Physiol.* 74(4):1879–1884.

114. Miura M, Belvisi MG, Stretton CD, Yacoub MH, and Barnes PJ. 1992. Role of potassium channels in bronchodilator responses in human airways. *Am. Rev. Respir. Dis.* 146(1):132–136.

115. Werner ME, Meredith AL, Aldrich RW, and Nelson MT. 2008. Hypercontractility and impaired sildenafil relaxations in the BKCa channel deletion model of erectile dysfunction. *Am. J. Physiol. Regul. Integr. Comp. Physiol.* 295(1):R181–8.

116. Basrai D, Kraft R, Bollensdorff C, Liebmann L, Benndorf K, and Patt S. 2002. BK channel blockers inhibit potassium-induced proliferation of human astrocytoma cells. *Neuroreport* 13(4):403–407.

117. Bloch M, Ousingsawat J, Simon R, Schraml P, Gasser TC, Mihatsch MJ, Kunzelmann K, and Bubendorf L. 2007. KCNMA1 gene amplification promotes tumor cell proliferation in human prostate cancer. *Oncogene* 26(17):2525–2534.

118. Latorre R and Brauchi S. 2006. Large conductance Ca2+-activated K+ (BK) channel: activation by Ca2+ and voltage. *Biol. Res.* 39(3):385–401.

119. Doyle DA, Morais Cabral J, Pfuetzner RA, Kuo A, Gulbis JM, Cohen SL, Chait BT, and MacKinnon R. 1998. The structure of the potassium channel: molecular basis of K+ conduction and selectivity. *Science* 280(5360):69–77.

120. Zhou Y, Morais-Cabral JH, Kaufman A, and MacKinnon R. 2001. Chemistry of ion coordination and hydration revealed by a K+ channel-Fab complex at 2.0 A resolution. *Nature* 414(6859):43–48.

121. Morais-Cabral JH, Zhou Y, and MacKinnon R. 2001. Energetic optimization of ion conduction rate by the K+ selectivity filter. *Nature* 414(6859):37–42.

122. Jiang Y, Lee A, Chen J, Cadene M, Chait BT, and MacKinnon R. 2002. Crystal structure and mechanism of a calcium-gated potassium channel. *Nature* 417(6888):515–522.

123. Jiang Y, Lee A, Chen J, Cadene M, Chait BT, and MacKinnon R. 2002. The open pore conformation of potassium channels. *Nature* 417(6888):523–526.

124. Jiang Y, Lee A, Chen J, Ruta V, Cadene M, Chait BT, and MacKinnon R. 2003. X-ray structure of a voltage-dependent K+ channel. *Nature* 423(6935):33–41.

125. Long SB, Campbell EB, and MacKinnon R. 2005. Crystal structure of a mammalian voltage-dependent Shaker family K+ channel. *Science* 309(5736):897–903.

126. Clayton GM, Altieri S, Heginbotham L, Unger VM, and Morais-Cabral JH. 2008. Structure of the transmembrane regions of a bacterial cyclic nucleotide-regulated channel. *Proc. Natl. Acad. Sci. U.S.A.* 105(5):1511–1515.

127. Alam A and Jiang Y. 2009. High-resolution structure of the open NaK channel. *Nat. Struct. Mol. Biol.* 16(1):30–34.

128. Hansen SB, Tao X, and MacKinnon R. 2011. Structural basis of PIP(2) activation of the classical inward rectifier K(+) channel Kir2.2. *Nature*:.

129. Whorton MR and MacKinnon R. 2011. Crystal Structure of the Mammalian GIRK2 K(+) Channel and Gating Regulation by G Proteins, PIP(2), and Sodium. *Cell* 147(1):199–208.

130. Payandeh J, Scheuer T, Zheng N, and Catterall WA. 2011. The crystal structure of a voltage-gated sodium channel. *Nature* 475(7356):353–358.

131. Bavro VN, De Zorzi R, Schmidt MR, Muniz JRC, Zubcevic L, Sansom MSP, Vénien-Bryan C, and Tucker SJ. 2012. Structure of a KirBac potassium channel with an open bundle crossing indicates a mechanism of channel gating. *Nat. Struct. Mol. Biol.* 19(2):158–163.

132. Magidovich E and Yifrach O. 2004. Conserved gating hinge in ligand- and voltage-dependent K+ channels. *Biochemistry* 43(42):13242–13247.

133. Li W and Aldrich RW. 2006. State-dependent block of BK channels by synthesized shaker ball peptides. *J. Gen. Physiol.* 128(4):423–441.

134. Zhou Y, Xia X-M, and Lingle CJ. 2011. Cysteine scanning and modification reveal major differences between BK channels and Kv channels in the inner pore region. *Proc. Natl. Acad. Sci. U.S.A.* 108(29):12161–12166.

135. Wilkens CM and Aldrich RW. 2006. State-independent block of BK channels by an intracellular quaternary ammonium. *J. Gen. Physiol.* 128(3):347–364.

136. Tang Q-Y, Zeng X-H, and Lingle CJ. 2009. Closed-channel block of BK potassium channels by bbTBA requires partial activation. *J. Gen. Physiol.* 134(5):409–436.

137. Jiang Y, Ruta V, Chen J, Lee A, and MacKinnon R. 2003. The principle of gating charge movement in a voltage-dependent K+ channel. *Nature* 423(6935):42–48.

138. Long SB, Campbell EB, and MacKinnon R. 2005. Voltage sensor of Kv1.2: structural basis of electromechanical coupling. *Science* 309(5736):903–908.

139. Ruta V, Chen J, and MacKinnon R. 2005. Calibrated measurement of gating-charge arginine displacement in the KvAP voltage-dependent K+ channel. *Cell* 123(3):463–475.

140. Tombola F, Pathak MM, and Isacoff EY. 2006. How does voltage open an ion channel? *Annu. Rev. Cell Dev. Biol.* 22:23–52.

141. Long SB, Tao X, Campbell EB, and MacKinnon R. 2007. Atomic structure of a voltage-dependent K+ channel in a lipid membrane-like environment. *Nature* 450(7168):376–382.

142. Tao X, Lee A, Limapichat W, Dougherty DA, and MacKinnon R. 2010. A gating charge transfer center in voltage sensors. *Science* 328(5974):67–73.

143. Armstrong CM and Bezanilla F. 1973. Currents related to movement of the gating particles of the sodium channels. *Nature* 242(5398):459–461.

144. Ma Z, Lou XJ, and Horrigan FT. 2006. Role of charged residues in the S1-S4 voltage sensor of BK channels. *J. Gen. Physiol.* 127(3):309–328.

145. Stefani E, Ottolia M, Noceti F, Olcese R, Wallner M, Latorre R, and Toro L. 1997. Voltage-controlled gating in a large conductance Ca2+-sensitive K+channel (hslo). *Proc. Natl. Acad. Sci. U.S.A.* 94(10):5427–5431.

146. Aggarwal SK and MacKinnon R. 1996. Contribution of the S4 segment to gating charge in the Shaker K+ channel. *Neuron* 16(6):1169–1177.

147. Seoh SA, Sigg D, Papazian DM, and Bezanilla F. 1996. Voltage-sensing residues in the S2 and S4 segments of the Shaker K+ channel. *Neuron* 16(6):1159–1167.

148. Koval OM, Fan Y, and Rothberg BS. 2007. A role for the S0 transmembrane segment in voltage-dependent gating of BK channels. *J. Gen. Physiol.* 129(3):209–220.

149. Liu G, Zakharov SI, Yang L, Deng S-X, Landry DW, Karlin A, and Marx SO. 2008. Position and role of the BK channel alpha subunit S0 helix inferred from disulfide crosslinking. *J. Gen. Physiol.* 131(6):537–548.

150. Yuan A, Dourado M, Butler A, Walton N, Wei A, and Salkoff L. 2000. SLO-2, a K+ channel with an unusual Cl- dependence. *Nat. Neurosci.* 3(8):771–779.

151. Pico AR. 2003. RCK Domain Model of Calcium Activation in BK Channels. Ph. D. thesis; the Rockefeller University, New York.

152. Derst C and Karschin A. 1998. Review: Evolutionary link between prokaryotic and eukaryotic K+ channels. *J. Exp. Biol.* 201(Pt 20):2791–2799.

153. Durell SR, Hao Y, Nakamura T, Bakker EP, and Guy HR. 1999. Evolutionary relationship between K(+) channels and symporters. *Biophys. J.* 77(2):775–788.

154. Kuo MM-C, Haynes WJ, Loukin SH, Kung C, and Saimi Y. 2005. Prokaryotic K(+) channels: from crystal structures to diversity. *FEMS Microbiol. Rev.* 29(5):961–985.

155. Ye S, Li Y, Chen L, and Jiang Y. 2006. Crystal structures of a ligand-free MthK gating ring: insights into the ligand gating mechanism of K+ channels. *Cell* 126(6):1161–1173.

156. Lingle CJ. 2007. Gating rings formed by RCK domains: keys to gate opening. *J. Gen. Physiol.* 129(2):101–107.

157. Niu X, Qian X, and Magleby KL. 2004. Linker-gating ring complex as passive spring and Ca(2+)-dependent machine for a voltage- and Ca(2+)-activated potassium channel. *Neuron* 42(5):745–756.

158. Wei A, Solaro C, Lingle C, and Salkoff L. 1994. Calcium sensitivity of BK-type KCa channels determined by a separable domain. *Neuron* 13(3):671–681.

159. Schreiber M and Salkoff L. 1997. A novel calcium-sensing domain in the BK channel. *Biophys. J.* 73(3):1355–1363.

160. Bao L, Kaldany C, Holmstrand EC, and Cox DH. 2004. Mapping the BKCa channel's 'Ca2+ bowl': side-chains essential for Ca2+ sensing. *J. Gen. Physiol.* 123(5):475–489.

161. Braun AP and Sy L. 2001. Contribution of potential EF hand motifs to the calcium-dependent gating of a mouse brain large conductance, calcium-sensitive K(+) channel. *J. Physiol. (Lond.)* 533(Pt 3):681–695.

162. Bian S, Favre I, and Moczydlowski E. 2001. Ca2+-binding activity of a COOH-terminal fragment of the Drosophila BK channel involved in Ca2+-dependent activation. *Proc. Natl. Acad. Sci. U.S.A.* 98(8):4776–4781.

163. Schreiber M, Yuan A, and Salkoff L. 1999. Transplantable sites confer calcium sensitivity to BK channels. *Nat. Neurosci.* 2(5):416–421.

164. Bao L, Rapin AM, Holmstrand EC, and Cox DH. 2002. Elimination of the BK(Ca) channel's high-affinity Ca(2+) sensitivity. *J. Gen. Physiol.* 120(2):173–189.

165. Xia X-M, Zeng X, and Lingle CJ. 2002. Multiple regulatory sites in large-conductance calcium-activated potassium channels. *Nature* 418(6900):880–884.

166. Zhang G, Huang S-Y, Yang J, Shi J, Yang X, Moller A, Zou X, and Cui J. 2010. Ion sensing in the RCK1 domain of BK channels. *Proc. Natl. Acad. Sci. U.S.A.* 107(43):18700–18705.

167. Cox DH. 2007. *BKCa-Channel Structure and Function*. S-H Chung, OS Andersen, V Krishnamurthyed. 171–218. New York, NY: Springer New York.

168. Blundell TL, Sibanda BL, Montalvão RW, Brewerton S, Chelliah V, Worth CL, Harmer NJ, Davies O, and Burke D. 2006. Structural biology and bioinformatics in drug design: opportunities and challenges for target identification and lead discovery. *Philos. Trans. R. Soc. Lond., B, Biol. Sci.* 361(1467):413–423.

169. Wlodawer A and Vondrasek J. 1998. Inhibitors of HIV-1 protease: a major success of structure-assisted drug design. *Annu Rev Biophys Biomol Struct* 27:249–284.

170. Wlodawer A. 2002. Rational approach to AIDS drug design through structural biology. *Annu. Rev. Med.* 53:595–614.

171. Junge FF, Schneider BB, Bernhard FF, 6. 2008. Large-scale production of functional membrane proteins. *Cell. Mol. Life Sci.* 65(11):1729–1755.

172. Mus-Veteau I. 2010. Heterologous expression of membrane proteins for structural analysis. *Methods Mol. Biol.* 601(601):1–16.

173. Wiener MC. 2004. A pedestrian guide to membrane protein crystallization. *Methods* 34(3):364–372.

174. Cereghino JL and Cregg JM. 2000. Heterologous protein expression in the methylotrophic yeast Pichia pastoris. *FEMS Microbiol. Rev.* 24(1):45–66.

175. Kawate T and Gouaux E. 2006. Fluorescence-detection size-exclusion chromatography for precrystallization screening of integral membrane proteins. *Structure* 14(4):673–681.

176. Miller C, ed. 1986. *Ion channel reconstitution*. C Millered. Plenum Press, New York.

177. Morera FJ, Vargas G, González C, Rosenmann E, and Latorre R. 2007. Ion-Channel Reconstitution. 400(Chapter 38):571–585. Methods Mol. Biol.

178. Miller C. 1995. The charybdotoxin family of K+ channel-blocking peptides. *Neuron* 15(1):5–10.

179. MacKinnon R, Cohen SL, Kuo A, Lee A, and Chait BT. 1998. Structural conservation in prokaryotic and eukaryotic potassium channels. *Science* 280(5360):106–109.

180. Garcia ML, Galvez A, Garcia-Calvo M, King VF, Vázquez J, and Kaczorowski GJ. 1991. Use of toxins to study potassium channels. *J. Bioenerg. Biomembr.* 23(4):615–646.

181. Galvez A, Gimenez-Gallego G, Reuben JP, Roy-Contancin L, Feigenbaum P, Kaczorowski GJ, and Garcia ML. 1990. Purification and characterization of a unique, potent, peptidyl probe for the high conductance calcium-activated potassium channel from venom of the scorpion Buthus tamulus. *J. Biol. Chem.* 265(19):11083–11090.

182. Garcia-Calvo M, Vázquez J, Smith M, Kaczorowski GJ, and Garcia ML. 1991. Characterization of the solubilized charybdotoxin receptor from bovine aortic smooth muscle. *Biochemistry* 30(46):11157–11164.

183. Koschak A, Koch RO, Liu J, Kaczorowski GJ, Reinhart PH, Garcia ML, and Knaus HG. 1997. [125I]Iberiotoxin-D19Y/Y36F, the first selective, high specific activity radioligand for high-conductance calcium-activated potassium channels. *Biochemistry* 36(7):1943–1952.

184. Nishikawa M, Nojima S, Akiyama T, Sankawa U, and Inoue K. 1984. Interaction of digitonin and its analogs with membrane cholesterol. *J. Biochem.* 96(4):1231–1239.

185. Parini A and Graham RM. 1989. Glycerol, sodium phosphate, and sodium chloride permit the solubilization and partial purification of rat hepatic alpha 1-receptors by 3-(3-cholamidylpropyl)-dimethylammonio-1-propanesulfonate. *Anal. Biochem.* 176(2):375–381.

186. Arnold T and Linke D. 2008. The use of detergents to purify membrane proteins. *Curr Protoc Protein Sci* Chapter 4:Unit 4.8.1–4.8.30.

187. MacKinnon R and Miller C. 1988. Mechanism of charybdotoxin block of the high-conductance, Ca2+-activated K+ channel. *J. Gen. Physiol.* 91(3):335–349.

188. Shimony E, Sun T, Kolmakova-Partensky L, and Miller C. 1994. Engineering a uniquely reactive thiol into a cysteine-rich peptide. *Protein Eng.* 7(4):503–507.

189. Knaus HG, Schwarzer C, Koch RO, Eberhart A, Kaczorowski GJ, Glossmann H, Wunder F, Pongs O, Garcia ML, and Sperk G. 1996. Distribution of high-conductance Ca(2+)-activated K+ channels in rat brain: targeting to axons and nerve terminals. *J. Neurosci.* 16(3):955–963.

190. Giangiacomo KM, Becker J, Garsky C, Schmalhofer W, Garcia ML, and Mullmann TJ. 2008. Novel alpha-KTx sites in the BK channel and comparative sequence analysis reveal distinguishing features of the BK and KV channel outer pore. *Cell Biochem. Biophys.* 52(1):47–58.

191. Daum G, Lees ND, Bard M, and Dickson R. 1998. Biochemistry, cell biology and molecular biology of lipids of Saccharomyces cerevisiae. *Yeast* 14(16):1471–1510.

192. Lagane B, Gaibelet G, Meilhoc E, Masson JM, Cézanne L, and Lopez A. 2000. Role of sterols in modulating the human mu-opioid receptor function in Saccharomyces cerevisiae. *J. Biol. Chem.* 275(43):33197–33200.

193. Yuan P, Leonetti MD, Pico AR, Hsiung Y, and MacKinnon R. 2010. Structure of the human BK channel Ca2+-activation apparatus at 3.0 A resolution. *Science* 329(5988):182–186.

194. Yuan P, Leonetti MD, Hsiung Y, and MacKinnon R. 2011. Open structure of the Ca(2+) gating ring in the high-conductance Ca(2+)-activated K(+) channel. *Nature*:.

195. Yusifov T, Savalli N, Gandhi CS, Ottolia M, and Olcese R. 2008. The RCK2 domain of the human BKCa channel is a calcium sensor. *Proc. Natl. Acad. Sci. U.S.A.* 105(1):376–381.

196. Kim H-J, Lim H-H, Rho S-H, Eom SH, and Park C-S. 2006. Hydrophobic interface between two regulators of K+ conductance domains critical for calcium-dependent activation of large conductance Ca2+-activated K+ channels. *J. Biol. Chem.* 281(50):38573–38581.

197. Wu Y, Yang Y, Ye S, and Jiang Y. 2010. Structure of the gating ring from the human large-conductance Ca(2+)-gated K(+) channel. *Nature* 466(7304):393–397.

198. Zhang X, Zeng X, Xia X-M, and Lingle CJ. 2006. pH-regulated Slo3 K+ channels: properties of unitary currents. *J. Gen. Physiol.* 128(3):301–315.

199. Stühmer W. 1992. Electrophysiological recording from Xenopus oocytes. *Meth. Enzymol.* 207:319–339.

200. Strong M, Sawaya MR, Wang S, Phillips M, Cascio D, and Eisenberg D. 2006. Toward the structural genomics of complexes: crystal structure of a PE/PPE protein complex from Mycobacterium tuberculosis. *Proc. Natl. Acad. Sci. U.S.A.* 103(21):8060–8065.

201. Torgerson DG, Kulathinal RJ, and Singh RS. 2002. Mammalian sperm proteins are rapidly evolving: evidence of positive selection in functionally diverse genes. *Mol. Biol. Evol.* 19(11):1973–1980.

202. Swanson WJ and Vacquier VD. 2002. The rapid evolution of reproductive proteins. *Nat. Rev. Genet.* 3(2):137–144.

203. Srivastava J, Barber DL, and Jacobson MP. 2007. Intracellular pH sensors: design principles and functional significance. *Physiology (Bethesda)* 22:30–39.

204. Rao S and Rossmann M. 1973. Comparison of Super-Secondary Structures in Proteins. *J. Mol. Biol.* 76(2):241–&.

205. Lee JO, Rieu P, Arnaout MA, and Liddington R. 1995. Crystal structure of the A domain from the alpha subunit of integrin CR3 (CD11b/CD18). *Cell* 80(4):631–638.

206. Branden C and Tooze J. 1991. *Introduction to protein structure*. Garland Publ., New York.

207. Roosild TP, Miller S, Booth IR, and Choe S. 2002. A mechanism of regulating transmembrane potassium flux through a ligand-mediated conformational switch. *Cell* 109(6):781–791.

208. Albright RA, Ibar J-LV, Kim CU, Gruner SM, and Morais-Cabral JH. 2006. The RCK domain of the KtrAB K+ transporter: multiple conformations of an octameric ring. *Cell* 126(6):1147–1159.

209. Santi CM, Butler A, Kuhn J, Wei A, and Salkoff L. 2009. Bovine and mouse SLO3 K+ channels: evolutionary divergence points to an RCK1 region of critical function. *J. Biol. Chem.* 284(32):21589–21598.

210. Shi J, Krishnamoorthy G, Yang Y, Hu L, Chaturvedi N, Harilal D, Qin J, and Cui J. 2002. Mechanism of magnesium activation of calcium-activated potassium channels. *Nature* 418(6900):876–880.

211. Yang H, Shi J, Zhang G, Yang J, Delaloye K, and Cui J. 2008. Activation of Slo1 BK channels by Mg2+ coordinated between the voltage sensor and RCK1 domains. *Nat. Struct. Mol. Biol.* 15(11):1152–1159.

212. Park CS, Hausdorff SF, and Miller C. 1991. Design, synthesis, and functional expression of a gene for charybdotoxin, a peptide blocker of K+ channels. *Proc. Natl. Acad. Sci. U.S.A.* 88(6):2046–2050.

213. Otwinowski Z and Minor W. 1997. Processing of X-ray diffraction data collected in oscillation mode. *Method Enzymol* 276:307–326.

214. Terwilliger TC and Berendzen J. 1999. Automated MAD and MIR structure solution. *Acta Crystallogr. D Biol. Crystallogr.* 55(Pt 4):849–861.

215. Emsley P and Cowtan K. 2004. Coot: model-building tools for molecular graphics. *Acta Crystallogr. D Biol. Crystallogr.* 60(Pt 12 Pt 1):2126–2132.

216. Ramachandran GN, Ramakrishnan C, and Sasisekharan V. 1963. Stereochemistry of polypeptide chain configurations. *J. Mol. Biol.* 7:95–99.

217. Potterton E, Briggs P, Turkenburg M, and Dodson E. 2003. A graphical user interface to the CCP4 program suite. *Acta Crystallogr. D Biol. Crystallogr.* 59(Pt 7):1131–1137.

218. Brunger AT. 2007. Version 1.2 of the Crystallography and NMR system. *Nat Protoc* 2(11):2728–2733.

219. Murshudov GN, Vagin AA, and Dodson EJ. 1997. Refinement of macromolecular structures by the maximum-likelihood method. *Acta Crystallogr. D Biol. Crystallogr.* 53(Pt 3):240–255.

220. Echols N, Milburn D, and Gerstein M. 2003. MolMovDB: analysis and visualization of conformational change and structural flexibility. *Nucleic Acids Res.* 31(1):478–482.

221. Ruta V, Jiang Y, Lee A, Chen J, and MacKinnon R. 2003. Functional analysis of an archaebacterial voltage-dependent K+ channel. *Nature* 422(6928):180–185.

222. Heginbotham L, Kolmakova-Partensky L, and Miller C. 1998. Functional reconstitution of a prokaryotic K+ channel. *J. Gen. Physiol.* 111(6):741–749.

223. Liman ER, Tytgat J, and Hess P. 1992. Subunit stoichiometry of a mammalian K+ channel determined by construction of multimeric cDNAs. *Neuron* 9(5):861–871.

224. Barrett JN, Magleby KL and Palotta BS. 1982. Properties of single calcium-activated potassium channels in cultured rat muscle. *J. Physiol*. 331:211-230